Real-time MRI of Moving Spins Using Undersampled Radial FLASH

Dissertation zur Erlangung des

naturwissenschaftlichen Doktorgrades

der Bayerischen Julius-Maximilians-Universität Würzburg

vorgelegt von

Arun Antony Joseph

aus Chennai, Indien

Würzburg 2013

Eingereicht am:
bei der Fakultät für Physik und Astronomie

1. Gutachter: Prof. Dr. rer. nat. P.M. Jakob
2. Gutachter: Prof. Dr. rer. nat. J. Frahm
3. Gutachter:
der Dissertation

1. Prüfer: Prof. Dr. rer. nat. P.M. Jakob
2. Prüfer: Prof. Dr. rer. nat. J. Frahm
3. Prüfer: Prof. Dr. rer. nat. A. Denner
im Promotionskolloquium

Tag des Promotionskolloquiums:
Doktorurkunde ausgehändigt am:

Abstract

Nuclear spins in motion is an intrinsic component of any dynamic process when studied using magnetic resonance imaging (MRI). Moving spins define many functional characteristics of the human body such as diffusion, perfusion and blood flow. Quantitative MRI of moving spins can provide valuable information about the human physiology or of a technical system. In particular, phase-contrast MRI, which is based on two images with and without a flow-encoding gradient, has emerged as an important diagnostic tool in medicine to quantify human blood flow. Unfortunately, however, its clinical usage is hampered by long acquisition times which only provide mean data averaged across multiple cardiac cycles and therefore preclude monitoring the immediate physiological responses to stress or exercise. These limitations are expected to be overcome by real-time imaging which constitutes a primary aim of this thesis.

Short image acquisition times, as the core for real-time phase-contrast MRI, can be mainly realized through undersampling of the acquired data. Therefore the development focused on related technical aspects such as pulse sequence design, k-space encoding schemes and image reconstruction. A radial encoding scheme was experimentally found to be robust to motion and less sensitive to undersampling than Cartesian encoding. Radial encoding was combined with a FLASH acquisition technique for building an efficient real-time phase-contrast MRI sequence. The sequence was further optimized through overlapping of gradients to achieve the shortest possible echo time. Regularized nonlinear inverse reconstruction (NLINV), a technique which jointly estimates the image content and its corresponding coil sensitivities, was used for image reconstruction. NLINV was adapted specifically for phase-contrast MRI to produce both magnitude images and phase-contrast maps. Real-time phase-contrast MRI therefore combined two highly undersampled (up to a factor of 30) radial gradient-echo acquisitions with and without a flow-encoding gradient with modified NLINV reconstructions. The developed method achieved real-time phase-contrast MRI at both high spatial (1.3 mm) and temporal resolution (40 ms).

Applications to healthy human subjects as well as preliminary studies of patients demonstrated real-time phase-contrast MRI to offer improved patient compliance (e.g., free breathing) and immediate access to physiological variations of flow parameters (e.g., response to enhanced in-

trathoracic pressure). In most cases, quantitative blood flow was measured in the ascending aorta as an important blood vessel of the cardiovascular circulation system commonly studied in the clinic. The performance of real-time phase-contrast MRI was validated in comparison to standard Cine phase-contrast MRI using studies of flow phantoms as well as under in vivo conditions. The evaluations confirmed good agreement for comparable results.

As a further extension to real-time phase-contrast MRI, this thesis implemented and explored a dual-echo phase-contrast MRI method which employs two sequential gradient echoes with and without flow encoding. The introduction of a flow-encoding gradient in between the two echoes aids in the further reduction of acquisition time. Although this technique was efficient under in vitro conditions, in vivo studies showed the influence of additional motion-induced phase contributions. Due to these additional temporal phase information, the approach showed little promise for quantitative flow MRI.

As a further method three-dimensional real-time phase-contrast MRI was developed in this thesis to visualize and quantify multi-directional flow at about twice the measuring time of the standard real-time MRI method, i.e. at about 100 ms temporal resolution. This was achieved through velocity mapping along all three physical gradient directions. Although the method is still too slow to adequately cover cardiovascular blood flow, the preliminary results were found to be promising for future applications in tissues and organ systems outside the heart. Finally, future developments are expected to benefit from the adaptation of model-based reconstruction techniques to real-time phase-contrast MRI.

Zusammenfassung

Die Bewegung der Kernspins ist eine wesentliche Eigenschaft von dynamischen Vorgängen, die mit Hilfe der Magnetresonanztomographie (MRT) untersucht werden. Bewegte oder fließende Spins charakterisieren viele Funktionen des menschlichen Körpers, wie z.B. die Gewebeperfusion und den Blutfluss in den Gefäßen. Die quantitative MRT von bewegten Spins kann daher wertvolle Informationen über die menschliche Physiologie oder auch über ein technisches System geben. Insbesondere die Phasenkontrast-MRT, die auf der Aufnahme von zwei Bildern mit und ohne flusskodierenden Gradienten basiert, hat sich als ein wichtiges diagnostisches Werkzeug in der Medizin entwickelt, um den Blutfluss funktionell zu quantifizieren. Die klinische Nutzung ist jedoch durch die langen Messzeiten eingeschränkt, da die Daten über mehrere Herzzyklen gemittelt werden müssen und damit die Untersuchung unmittelbarer physiologischer Reaktionen auf Stress und/oder Muskelbelastung ausgeschlossen ist. Ein primäres Ziel dieser Arbeit war es, diese Einschränkungen durch die Entwicklung einer MRT-Flussmessung in Echtzeit zu überwinden.

Entscheidende Grundlage jeder Echtzeit-MRT sind kurze Aufnahmezeiten, die vor allem durch eine Reduktion der aufgenommenen Daten (Unterabtastung) realisiert werden. Daher konzentrierte sich die hier vorgestellte Entwicklung auf die damit verbundenen technischen Aspekte wie die MRT-Sequenz zur Datenaufnahme, das räumliche Kodierungsschema, und die Bildrekonstruktion. Experimentell erwies sich ein radiales Kodierungsschema als robust gegenüber Bewegungen und relativ unempfindlich gegenüber milder Unterabtastung. Dieses Kodierungs schema wurde mit der FLASH Aufnahmetechnik für eine effiziente Phasenkontrast-Sequenz in Echtzeit kombiniert. Zusätzlich wurde die Sequenz durch Überlappung von Gradienten hinsichtlich einer kurzen Echozeit optimiert. Für die Bildrekonstruktion wurde die regularisierte nichtlineare inverse Rekonstruktion (NLINV) verwendet, bei der die Bildinformation und die entsprechenden Spulensensitivitäten gleichzeitig geschätzt werden. NLINV wurde speziell für die Phasenkontrast-MRT angepasst, um sowohl Betragsbilder als auch robuste Phasenkontrast-Karten mit hoher raumzeitlicher Genauigkeit zu berechnen. Das erarbeitete Verfahren der Phasenkontrast-MRT in Echtzeit kombiniert daher zwei stark unterabgetastete (bis zu einem Faktor von 30) und unterschiedlich flusskodierte, radiale Gradientenecho-Aufnahmen mit einer

modifizierten NLINV Rekonstruktion. Mit dieser Methode wurde sowohl eine gute räumliche Auflösung (1.3 mm), als auch eine hohe zeitliche Auflösung (40 ms) erreicht.

Bei Anwendungen an gesunden Probanden sowie vorläufigen Untersuchungen von Patienten konnte nachgewiesen werden, dass die Phasenkontrast-MRT in Echtzeit einen verbesserten Komfort für die Patienten (z.B. freie Atmung) und unmittelbaren Zugang zu physiologischen Veränderungen der Flussparameter bietet (z.B. Reaktion auf erhöhten Druck im Brustraum). In den meisten Fällen wurden quantitative Blutflussmessungen in der aufsteigenden Aorta, einem klinisch wichtigen Gefäß des Herz-Kreislauf-Systems, vorgenommen. Die Messungen mit der Phasenkontrast-MRT in Echtzeit wurden mit der EKG-getriggerten Cine Phasenkontrast-MRT (klinischer Standard) an einem Flussphantom und unter in vivo Bedingungen verglichen. Die Ergebnisse zeigten unter vergleichbaren Bedingungen gute Übereinstimmung.

Im Rahmen dieser Arbeit wurde zusätzlich eine Doppelecho-Variante der Phasenkontrast-MRT in Echtzeit implementiert. Das Einfügen eines flusskodierenden Gradienten zwischen den beiden Echos führte zu einer weiteren Reduzierung der Messzeit. Obwohl sich diese Technik unter in vitro Bedingungen als tauglich erwies, zeigten sich bei in vivo Studien störende Einflüsse durch bewegungsinduzierte Phasenbeiträge, die wenig Erfolg für quantitative Flussmessungen versprechen.

Als weitere Methode wurde in dieser Arbeit eine dreifach kodierte Sequenz zur Phasenkontrast-MRT entwickelt, um multidirektionalen Fluss zu untersuchen. Die Geschwindigkeitskodierung entlang aller drei physikalischen Gradientenrichtungen führte zu einer verlängerten Messzeit (zeitliche Auflösung ~100 ms) gegenüber der Echtzeit-Flussmessung in nur einer Richtung. Obwohl das Verfahren noch zu langsam ist, um den kardiovaskulären Blutfluss adäquat zu beschreiben, waren vorläufige Ergebnisse in Körperregionen außerhalb des Herzens für zukünftige klinische Anwendungen sehr vielversprechend. Es ist zu erwarten, dass entsprechende Weiterentwicklungen von modellbasierten Rekonstruktionsverfahren profitieren werden.

Contents

Chapter 1

Introduction

Magnetic resonance imaging (MRI) is a technique prominently used in the field of medical imaging. It came into existence in 1973 in a seminal publication by Paul Lauterbur [1] after 30 years of research on nuclear magnetic resonance spectroscopy. Since then, major technical advances have aided in making MRI an indispensible tool in the field of diagnostic imaging. Key advantages of MRI in comparison to other medical imaging techniques such as X-ray computed tomography (CT) and positron emission tomography (PET) are its non-invasiveness, the excellent soft-tissue contrast without the need of a contrast agent and the access to high spatial resolution. Moreover, the technical variability of MRI allows for encoding diverse qualitative and quantitative informations that range from microstructural to functional imaging for widespread applications. For example, parameters comprise spin density, T1, T2, chemical shift, magnetization transfer, chemical exchange, flow, diffusion and perfusion that aid in the diagnosis of diseases or in understanding specific physiological processes or technical systems. This thesis specifically addresses the field of flow imaging.

Flow imaging refers to MRI of moving spins. During the past decade, the number of methods and techniques related to flow MRI has strongly increased. The various approaches can be generalized as qualitative and quantitative techniques based on the information produced. Although qualitative methods provide perceivable visual information, comprehensive analysis of diseases and physiological processes are better provided by quantitative techniques. Phase-contrast flow MRI, which in its simplest form combines two images with and without a flow-encoding gradient, is one of the prominent methods that provide both qualitative and quantitative information about moving spins. However, existing implementations suffer from drawbacks that limit its usage in clinical applications. Key problems are the need for long acquisition times, the occurrence of motion artifacts and only moderate patient compliance. In order to improve patient comfort and reduce motion artifacts, methods such as Cine imaging with retrospective gating have been developed and used extensively for cardiovascular imaging. These methods

interpolate the data acquired over multiple cardiac cycles into a single cardiac cycle. Obviously, such approaches do not provide access to physiological variations and can not be applied to patients with irregular heart cycles as observed during arrhythmia. These challenges are expected to be overcome by a robust and reliable real-time flow MRI method which provides quantitative flow information for individual heartbeats at sufficient spatial and temporal resolution. This task defines the primary aim of this thesis.

To achieve real-time phase-contrast MRI, the methodological developments focused on both the image acquisition and reconstruction process. Accelerated acquisitions are usually obtained through data undersampling which results in a corresponding reduction of the overall acquisition time. A certain degree of insensitivity to motion emerges as another design criterion for real-time MRI of moving objects. In this thesis, a radial sampling scheme was found to be beneficial for real-time recordings in comparison to a standard Cartesian sampling scheme. It was therefore used as the basis for the development and optimization of a phase-contrast MRI sequence. With respect to image reconstruction the present work adapted the recent development of a parallel imaging technique based on regularized nonlinear inversion (NLINV). In contrast to anatomical real-time MRI, phase-contrast MRI needs to reconstruct both magnitude images and phase-contrast maps. In fact, real-time imaging using NLINV has been previously realized only for studies of joints, speaking and swallowing processes and cardiac functions. In this thesis, NLINV was modified to phase-contrast MRI to perform quantitative real-time flow studies at high spatio-temporal resolution. After validation in comparison to conventional Cine flow MRI and apart from preliminary patient studies, real-time phase-contrast MRI was mainly applied to study blood flow in the human aorta including physiological responses to changes in intrathoracic pressure. Additional methodological extensions dealt with dual-echo phase-contrast MRI to further decrease the acquisition times, and to multi-directional phase-contrast MRI to explore three-dimensional flow patterns at high temporal resolution.

Chapter 2

Magnetic Resonance Imaging

Magnetic resonance imaging is based on the physics of nuclear magnetic resonance (NMR) and its effect on condensed matter discovered by Bloch and Purcell [2, 3] in 1946. The basic physics of MR, that include the physical aspects of nuclear spins, signal generation and image formation, act as the foundation for the development of new MR imaging techniques. This chapter focuses on the introduction of the principles of MR imaging which will further aid in understanding the concepts and development of real-time phase-contrast imaging discussed in this thesis.

2.1   NMR Phenomenon

The basic physics of NMR is based on the curious property of spins of subatomic particles. Spin is a quantum mechanical description of the angular momentum present in the subatomic particles. This property is exhibited only by the nuclei with odd atomic numbers such as ^{1}H, ^{13}C, ^{31}P, or ^{23}Na where uneven number of neutrons and protons are present. Hydrogen proton (^{1}H), due to its abundant presence in the human body through water and fat molecules, is mostly used in MRI. The magnetic moment induced by these particles is related to the angular momentum represented by

$$\mu = \gamma \mathbf{J} \tag{2.1}$$

where γ is gyromagnetic ratio. The nuclear spin acts like a magnetic dipole and orient in different directions. The net magnetization is zero as the magnetic dipoles in different directions cancel each other. In the presence of external magnetic field, the nuclear spins experience *Zeeman splitting* and are aligned in two energy states. The energy states are proportional to the strength of magnetic field $\mathbf{B_0}$ and can be represented for hydrogen proton as

$$E_\downarrow = \gamma \frac{\hbar}{2} B_0 \tag{2.2}$$

$$E_\uparrow = -\gamma \frac{\hbar}{2} B_0 \tag{2.3}$$

where $\hbar$ is Planck's constant divided by 2π. The energy states are named anti-parallel($\downarrow$) and parallel ($\uparrow$) with respect to the alignment of spins to the external magnetic field. The difference in energy of the two energy states is given by

$$\triangle E = \hbar \gamma B_0 \tag{2.4}$$

The difference in spin population of the two energy levels is given by the Boltzmann relationship as

$$\frac{N_\uparrow}{N_\downarrow} = e^{\frac{\triangle E}{k_b T}} \tag{2.5}$$

where k_b and T are Boltzmann constant and temperature respectively. The spins in the energy state are unequally distributed with the larger amount of spins in the lower energy state (parallel$\uparrow$) causing a bulk magnetization M_0 parallel to the static B_0.

$$M_0 = \rho \frac{\gamma^2 \hbar^2}{4 k_b T} B_0 \tag{2.6}$$

ρ is the proton density within a macroscopic volume.

2.1.1   Excitation

Although spin is fundamentally a quantum mechanical concept, for better understanding of the principles of MRI, "classical" perspective can be employed. The direction of the magnetization vector in the static magnetic field is generally defined as the z direction. The transverse component of the proton magnetic moments precess along the xy plane with a definite frequency called Larmor frequency [4,5]. Larmor frequency is directly proportional to the static magnetic field B_0 given by

$$\omega_0 = \gamma B_0 \tag{2.7}$$

The angular frequency ω_0 in a static magnetic field of $B_0 = 2.89$ T used in this present work correspond to $7.74\dot{1}0^8$ rad/s or $f_0 = \omega_0 / 2\pi = 123.3$ MHz. The bulk magnetization vector $(\vec{M})$ experiences a torque due to varying magnetic field B_1 according to the classical equation of motion as

$$\frac{d\vec{M}}{dt} = \gamma \vec{M} \times B_1 \tag{2.8}$$

The B_1 field is achieved by the application of radiofrequency (RF) pulse. The NMR effect of radio frequency pulses was observed and demonstrated by Hahn in 1950 [6]. The RF pulse tilts the magnetization vector at an angle called *RF Flip angle* α which is proportional to the integral over the applied B_1.

$$\alpha = \gamma \int_0^{T_{RF}} B_1 dt \tag{2.9}$$

T_{RF} is the duration of the RF pulse excitation. After the application of RF pulse, a M_{xy} component of the magnetization precess around the z-axis. This time varying magnetic field induces an oscillation signal in a pertinent receiver coil. Figure 2.1 represents the magnetization vector during different stages of pulsed NMR experiment.
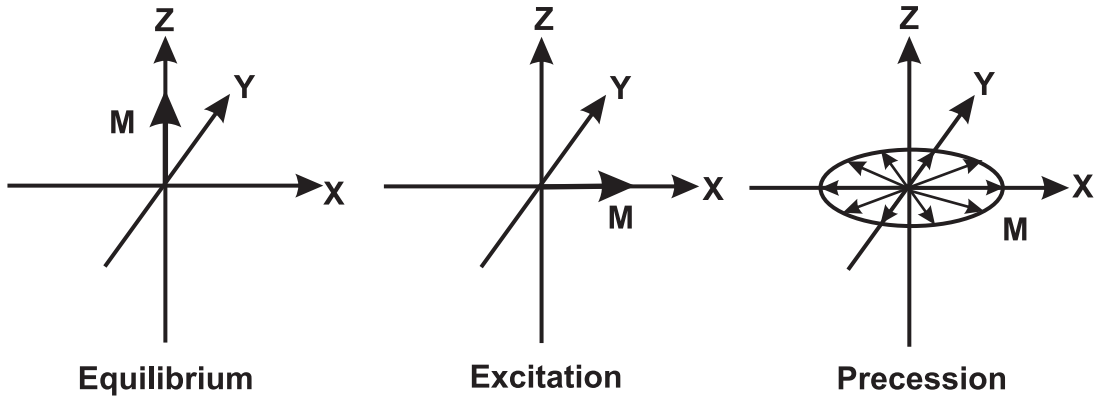
Figure 2.1: Representation of the pulsed NMR experiment during equilibrium, excitation and precession states. M represents the magnetization vector.

2.1.2 Relaxation

After the RF excitation the signal detected declines rapidly due to spins proceeding towards the thermal equilibrium state. In the process, the bulk magnetization encounters two relaxation mechanisms namely longitudinal and transverse relaxation [2]. Longitudinal relaxation, also called as spin-lattice relaxation, is the exponential recovery of the longitudinal magnetization M_z after RF pulse excitation. This is characterized by the energy exchange of protons with their environment. Longitudinal relaxation time, often represented with a time constant T_1, is a tissue specific parameter varying between 400 to 1500 ms.

$$M_z(t) = M_z(0) \cdot (1 - e^{\frac{-t}{T_1}}) \tag{2.10}$$

5

Transverse relaxation deals with the exponential decay of the transverse magnetization M_{xy} defined by signal loss due to spin interactions within a macroscopic volume. Therefore transverse magnetization is also known as spin-spin relaxation which leads to the dephasing of spins represented through the following equation along with the transverse relaxation time T_2.

$$M_{xy}(t) = M_{xy}(0) \cdot e^{\frac{-t}{T_2}} \tag{2.11}$$

Transverse relaxation time T_2 is always shorter than the longitudinal relaxation time T_1 and vary for different tissues within the human body between 50 to 150 ms. These effects were represented by Bloch [2] in 1946 through the following equation

$$\frac{d\vec{M}}{dt} = \vec{M} \times \gamma\vec{B} + \begin{pmatrix} -M_x/T_2 \\ -M_y/T_2 \\ (M_0/M_z)\,T_1 \end{pmatrix} \tag{2.12}$$

In practice the dephasing of spins is increased by the static field inhomogenities and magnetic field gradients [7]. This effect leads to a change in relaxation time which is shorter than T_2 and is represented as effective spin-spin relaxation T_2^*.

$$\frac{1}{T_2^*} = \frac{1}{T_2} + \frac{1}{T_{2inhom}} = \frac{1}{T_2} + \gamma\triangle B_0 \tag{2.13}$$

2.2 Signal Localization

Spatial information can be obtained by the use of additional gradient coils along with main magnetic field B_0 as introduced by Lauterbur [1]. These gradient coils create magnetic gradient fields in x,y and z directions. The gradient fields in different spatial directions can be created by switching gradient coils either separately or in combination with other coils. The idea is to differentiate spins from different locations as the larmor frequencies depends on the local field strength. The overall spatially-dependent magnetic field can be represented as

$$\mathbf{B}_z(x, y, z) = \mathbf{B}_0 + \mathbf{G}_x \cdot x + \mathbf{G}_y \cdot y + \mathbf{G}_z \cdot z \tag{2.14}$$

2.2.1 Slice Selection

Through the application of linear gradient G_z along with the RF pulse containing a bandwidth of frequencies $\triangle\omega$, the excitation of spins are spatially limited to the location represented by the following equation.

$$z = \left(\frac{\omega}{\gamma} - B_0 \right) / G_z \qquad \forall \omega \in \triangle \omega \qquad (2.15)$$

By this approach, the excitation is reduced from 3D macroscopic volume to a 2D imaging plane. In order to achieve a rectangular slice profile, the pulse shape has to approximate a sinc-function. In practice, truncated version of the sinc function is used with additional filtering to achieve finite length. Truncation or restricting the length of the sinc function reciprocally creates a broad slice profile. The choice of the filter for truncation should concur the trade-off between broadened flip angle distribution in slice and imperfect slice profile.

2.2.2   Frequency Encoding

The spins are spatially localized in the x direction through frequency encoding. This method encodes the spatial locations in the frequency of the received signal. Neglecting the relaxation effects for simplicity, the NMR signal obtained after the excitation of spins through the slice selection technique can be expressed as

$$s(t) = M \cdot e^{-i\gamma B_0 t} \qquad (2.16)$$

The Larmor frequency is spatially altered through the application of gradient G_x in the x direction during the sampling interval. This results in a linear relation between the Larmor frequency and the spin location in the x-direction yielding a complex signal represented as

$$s(t) = \int M(x) \cdot e^{-i\gamma G_x \cdot xt} dx \qquad (2.17)$$

where t is the duration of the frequency encoding gradient.

2.2.3   Phase Encoding

The frequency encoding gradient as explained in the previous section would be only sufficient to encode in one dimension i.e. x axis. Additional gradient is required to encode information in y axis. This is achieved through the application of phase encoding gradient in the y-direction. The phase encoding gradient, which is usually applied for a short span of time between excitation and data acquisition, induces a spatially dependent shift in the phase of spins along the y direction.

$$\varphi(y) = \gamma \cdot y \int_0^T G_y(t) dt \qquad (2.18)$$

where T is the total duration of the phase encoding gradient. In order to obtain a complete 2D image, the phase encoding gradient has to be repeated with the desired number of sampling

points in the y-direction.

2.3   k-space Sampling

Phase encoding and frequency encoding techniques in combination to obtain two dimensional images is generally referred as k-space formalism. The method to acquire and fill the k-space through the application of different gradients is described as k-space trajectory. The k-space trajectory is represented as

$$\mathbf{k}(t) = \frac{\gamma}{2\pi} \int_0^t \mathbf{G}(t)dt \tag{2.19}$$

The signal obtained from the transverse magnetization in the xy-plane can be represented by the following equation.

$$s(k_x, k_y) = \iint M(x, y) \cdot e^{-i2\pi(k_x x + k_y y)})dxdy \tag{2.20}$$

Although the signal obtained is represented above through the continuous Fourier transform, in practice it is discretized by sampling at a certain sampling rate. The sampling distance $\triangle k$ between two discrete points in k-space can be expressed by the image size i.e. field of view (FOV)

$$\triangle k = \frac{1}{FOV} \tag{2.21}$$

Ideally higher sampling distance through prolonged sampling duration is preferred as it increases signal to noise ratio (SNR). The sampling interval, also called the *dwell time*, of the receiver determines the bandwidth (BW) which is given by.

$$BW = \frac{1}{\triangle t} \tag{2.22}$$

where $\triangle$t indicates the acquisition time. The number of sample points (n) or *base resolution* is directly related to the number of image pixels. FOV and the base resolution determine the spatial resolution of the reconstructed image which is represented as

$$\triangle x = \frac{FOV}{n} \tag{2.23}$$

In order to avoid aliasing, the sampling distance has to satisfy Nyquist criterion given by

$$\triangle k = \frac{2k_{max}}{n} \leqslant \frac{1}{FOV} \tag{2.24}$$

where, k_{max} is the maximum frequency component.

The filling of k-space discussed above is based on the Cartesian encoding scheme where lines in k-space were acquired through frequency and phase encoding gradients. Cartesian sampling scheme is primarily used due to its simplicity, robustness with respect to various imperfections such as off-resonance and eddy current effects. The major drawback of the Cartesian scheme is its sensitivity to motion. Moreover, reduction of encoding lines for shortening of acquisition time results in the aliasing of signal in the phase encoding direction or decrease in spatial resolution. Due to the advancements in the MR hardware over the past years, several other complex k-space trajectories have come into existence such as echo-planar, radial and spiral trajectories.

Radial

The radial encoding scheme is a projection acquisition where each spoke passes through the center of the k-space. Radial scheme was initially proposed by Lauterbur [1] but was not favored as it was not technically robust. Over the years the interest for radial scheme has been revived due to the extensive reconstruction advantages [8] and advancements in hardware. In order to achieve radial trajectories, the amplitudes of the gradients are varied in different physical gradient axis and played out simultaneously.

$$G_x = G \cdot cos(\phi) \tag{2.25}$$

$$G_y = G \cdot sin(\phi) \tag{2.26}$$

where ϕ represents the angle of the spoke. As gradients in both directions are employed for each radial spoke in k-space, they are considered as read gradients rather than frequency and phase encoding gradients as in Cartesian scheme. Radial and spiral trajectories are one of the most frequently used non-Cartesian encoding schemes. The radial encoding scheme is greatly favored for real-time studies due to various advantages such as a certain tolerance to undersampling and less sensitivity to motion. The advantages of radial encoding scheme will be greatly discussed in the chapter 4.

Spiral

Spiral encoding [9, 10] involves the simultaneous application of oscillating gradients G_x, G_y with varying amplitudes. This leads to the acquisition of the k-space in a spiral trajectory starting commonly from the center of the k-space (Figure 2.2). The spiral encoding scheme

has the advantage of acquiring samples from the center of k-space immediately after the RF excitation. This enables acquisition of maximum signal due to minimal dephasing of spins after the excitation. Undersampling is performed with decreasing the number of shots, often called as interleaves, in a spiral scan. Reduced number of interleaves have been used for the purpose of dynamic imaging. However, the major drawback of spiral encoding scheme is its high sensitivity to off-resonance effects when compared to Cartesian and radial schemes [11]. Although spiral scheme do not produce ghosting artifacts as in Cartesian scheme, it is considered to be sensitive to motion when compared with radial scheme [12]. Moreover, spiral scheme is considered to be more sensitive to hardware imperfections than other acquisitions methods [11].

Echo-planar Imaging

Echo-planar imaging (EPI) used for fast imaging [13,14] involves the covering of the k-space by a series of gradient echoes after a single RF excitation. Although EPI has been favored previously for fast imaging, it suffers from many drawbacks such as geometric distortions caused by off-resonance [15,16] and Nyquist ghosts due to alternating gradients [17]. Further similar to spiral, EPI also suffers from reduced spatial resolution due to long acquisition time and $T_2^\star$ decay.
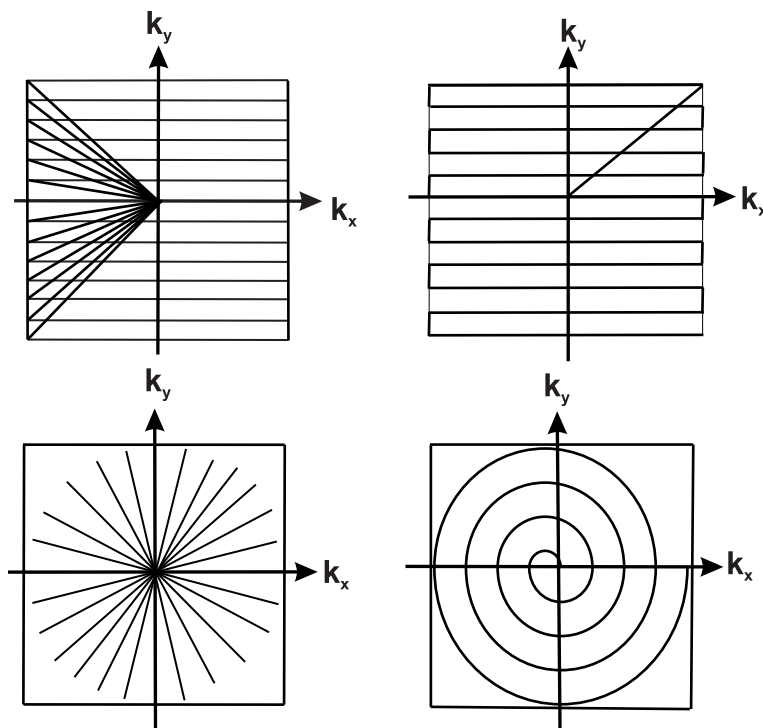

Figure 2.2: Schematic representation of different encoding schemes used in MRI. In clockwise direction Cartesian, echo-planar imaging, spiral, and radial.

2.4   Image Reconstruction

The formation of the k-space is followed by reconstruction of the data by inverse Fourier transformation. The natural equidistant distribution of sample points in k-space is an advantage of Cartesian encoding scheme. For the other k-space trajectory schemes the raw data obtained has to be regridded before the reconstruction operation which is usually performed by interpolation. Fast Fourier transform (FFT) operation is then performed on a uniformly distributed grid of sample points to obtain the reconstructed image. FFT operation for a two dimensional image is performed separately for each row and column of the raw data matrix. The reconstructed data matrix is complex, which can be further processed to display magnitude and phase images.

2.4.1   Gridding and Inverse FFT

Gridding or regridding technique was introduced to medical imaging in 1985 by O'Sullivan [18] and was later adapted in MRI for the reconstruction of data acquired through non-Cartesian encoding schemes. This technique basically deals with the interpolation of sample points onto a rectilinear grid prior to normal FFT based reconstruction. For radial encoding the data consists of varying sampling density and has to be density compensated before the interpolation is performed. The density compensation function is used as a weighting function and is performed for each sample point in the k-space. This is followed by the interpolation operation in the frequency space and resampled onto the Cartesian grid. The resampling onto the Cartesian grid is achieved by the convolution of measured samples with the interpolation kernel. Kaiser-Bessel window kernel was found to be an optimal interpolation function for radial acquisitions providing good quality images at reasonable window size and is given by

$$
K_{kb}(x) = \begin{cases} \frac{1}{L} I_0(\beta\sqrt{1 - (2x/L)^2} & \mid x \mid \leq \frac{L}{2}, \\ 0 & \mid x \mid > \frac{L}{2}. \end{cases} \tag{2.27}
$$

where L is the width of the kernel, $I_0(x)$ denotes the zero-order modified Bessel function and β is the shape factor. Since the gridding operation is performed discrete, aliasing or multiple copies of image object is produced in the image after the Fourier transformation. Aliasing is avoided by oversampling of images in both dimensions which leads to the increase of distance between the sampling points or in other words the aliasing is pushed towards the outer regions of the image. Image crop operation is performed on the Fourier transformed image to display the original region of interest without aliasing.

2.5 Pulse Sequence

A pulse sequence can be defined as a pictorial representation of the sequence of events for signal acquisition and usually represents the events (RF pulse, gradients, analog to digital converter (ADC)) between two consecutive RF excitation pulse. The terms echo time (TE) and repetition time (TR) are used to refer the different time periods in pulse sequences. TE, which indicate the time between signal generation and acquisition, extends from the center RF pulse to the center of the echo. TR refers to the time between center of two consecutive RF pulses for signal generation. Although there are many pulse sequences employed in the field of MR imaging, only few basic sequences are discussed.

2.5.1 Spin-echo Sequence

The spin-echo sequence was introduced by Hahn in 1950 [6, 19]. The basic pulse sequence, as seen in Figure 2.3, consists of the application of two RF pulses with different flip angles of 90° and 180°. As discussed previously, the magnetization vector M is flipped by 90° pulse to the transverse plane xy and dephases with time. By the application of additional 180° pulse, the spins are inverted and rephase in time. These spins are exactly in phase thereby creating a spin-echo which is acquired. The use of 180° RF pulse compensates for the local field inhomogeneities distortions which lead to $T_2^\star$ relaxation time. Therefore the spin-echo signal amplitude is entirely based on T_2 relaxation time. The gradients represented in Figure 2.3 are used for spatial localization of the spins.
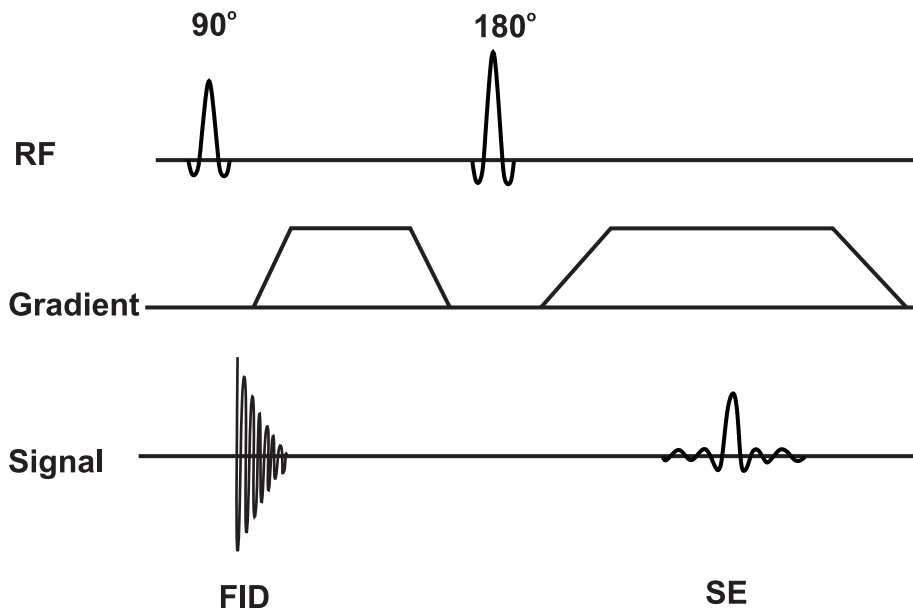

Figure 2.3: Schematic representation of the spin-echo pulse sequence. FID and SE represent the free induction decay and spin-echo signal, respectively.

2.5.2 Gradient-echo Sequence

The gradient-echo sequence (Figure 2.4) consists of two gradients of opposite polarity namely prephasing and readout gradient. The spins are initially dephased by the prephasing gradient and are then rephased by the readout gradient to generate an echo. The peak of the gradient-echo occurs at the center of the readout gradient [17]. Local field inhomogeneities and T_2 induce incomplete or partial rephasing of the spins. The signal amplitude therefore depends on TE and $T_2^\star$ by a factor $e^{-TE/T_2^\star}$. Gradient-echoes are also known in other names such as gradient-recalled echoes, gradient-refocused echoes or field echoes. The acquisition time is highly shortened with gradient-echo as compared to spin-echo technique due to the non-application of 180° RF pulse. Gradient-echo acquisitions can be performed fast by using flip angles α smaller than 90°. Such techniques are known as fast low angle shot (FLASH) imaging [20, 21].
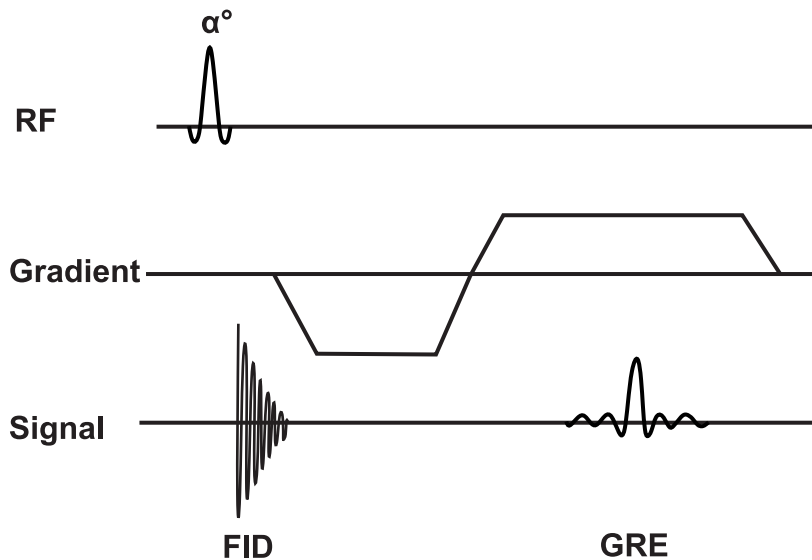

Figure 2.4: Schematic representation of the gradient-echo pulse sequence. FID and GRE represent the free induction decay and gradient-echo signal, respectively.

Chapter 3

Introduction to Flow MRI

The proton nuclear spins, which produce the NMR signal, are present abundantly in the body. The nuclear spins can be differentiated into stationary and moving spins. As the moving spins in the human body are mostly related to blood flow and cerebro-spinal fluid flow, the imaging of moving spins is called flow MRI. The present chapter starts with a history of flow MRI and then provides an overview of the methods employed for flow imaging. They are summarized in this chapter into two subgroups based on the information obtained from the images, namely qualitative and quantitative flow MRI.

3.1 History of Flow MRI

The development of MRI for flow imaging was based on the observations of NMR signal fluctuations from flowing fluid by Suryan [22]. It was reported that at slow and rapid flow the signal observed from the flowing fluid through the coil was strong and weak, respectively, due to the replacement of strongly magnetized spins with less completely magnetized moving spins. These observed effects from flowing medium were termed as washout effects. Hahn [6] observed the effect of motion in a magnetic gradient field on the amplitude of spin-echo formation. Further studies were performed by Carr and Purcell [23] to understand the dependence of spin-echo amplitude and the phase shifts acquired by the moving spins leading to the development of a flow sensitive pulse sequence. The two major properties of moving spins in the presence of magnetic field such as washout of saturated spins and phase shifts were applied in biological systems by Singer [24–26], Grover [27] and Battocletti [28]. In addition, Hahn [29] proposed the application of pulsed magnetic gradient field to induce phase shifts proportional to the velocity of the flowing medium. Stejskal [30, 31] applied gradient pulses on moving spins and described its effect on the phase of moving spins. The approach proposed by Stejskal [30] was further adopted and applied to velocity phase mapping by Moran [32] and Bryant [33]. Studies were performed to analyze the MR effects on blood flow [34] and the application of phase shifts on

flow measurements [35, 36]. Based on these foundations many techniques were developed for the purpose of imaging flow which would be introduced in the subsequent sections.

3.2   Angiographic Methods

Interest to observe blood vessels and thereby diagnose diseases led to the field of angiography. Angiography in the past was mainly performed with x-rays and contrast agents. Although x-ray angiography is advantageous to image small and moving blood vessels such as coronary arteries, due to continuous radiation exposure for a long duration, a consistent effort has been taken during the past decades to move toward non-radiative techniques. This interest has led to development of angiographic techniques in MRI. These methods effectively use the properties of flow to provide qualitative information of the blood vessels along with some quantitative information in some instances.

3.2.1   Black and Bright Blood Imaging

Black and Bright blood imaging are methods to image the blood vessels and vessel wall. These methods are named according to the pixel intensity for blood in the images. Black blood imaging captures the attenuation of the signal from the blood spins which can be achieved by employing different techniques. One of the common methods used for black blood imaging is spin-echo technique. Here, the refocusing pulse attenuates the signal of the rapid flowing blood while the signal from neighboring stationary tissue is preserved. The moving spins which experience both the excitation and the refocusing pulse produce a signal which is captured by the readout gradient. Other methods such as usage of spatial saturation pulses and inversion recovery magnetization methods can also be used for black blood imaging. Black blood methods are not prone to intravoxel dephasing as it further reduces the signal from blood. Further, they provide better specificity to stenosis and can be used for vessel wall studies due to its better depiction.

Bright blood imaging, which represents the blood in bright pixel intensities, is mainly achieved through gradient-echo imaging which produces hyperintense blood signal along with short TR. Apart from the high acquisition speed, the bright blood imaging through gradient echoes can be exploited for imaging inflow effects by angiographic techniques. Although images obtained from the black and bright imaging methods are helpful in delineating vessel walls from the inflowing blood, they lack in providing sufficient quantitative flow information. Figure 3.1 represents the black and bright blood images obtained from a transverse section of the head.
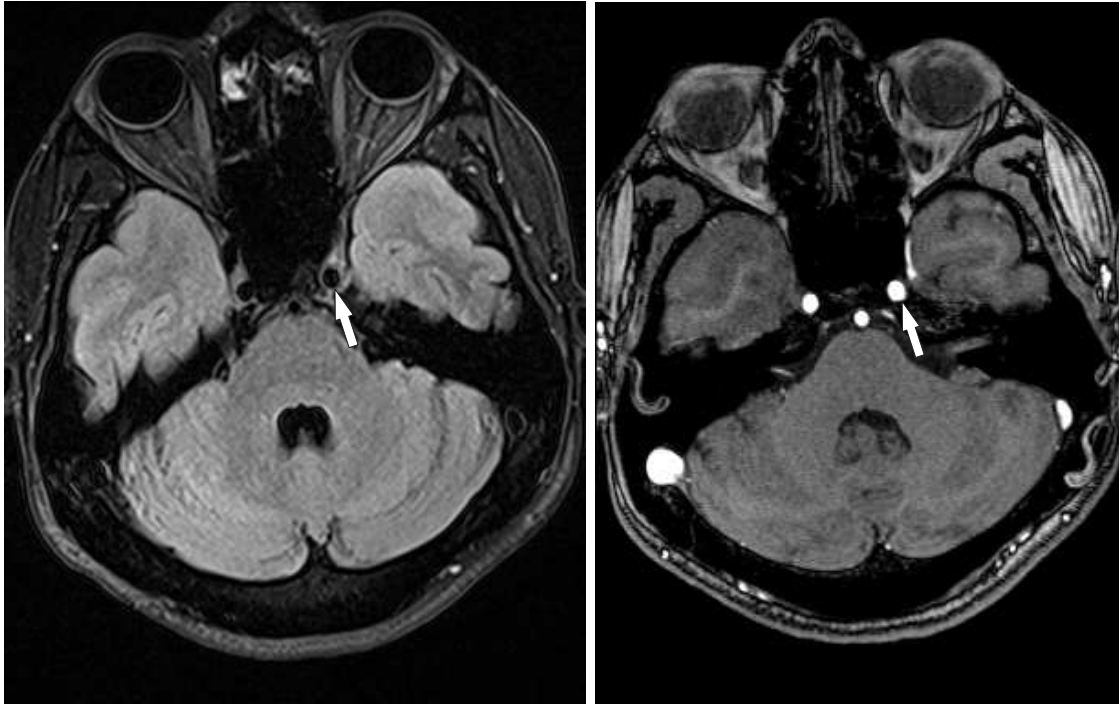
16

Figure 3.1: Transverse section of the human head around eye region. Carotid arteries (arrow) in a black blood image (left) and bright blood image (right).

3.2.2 Time-of-Flight Methods

Time-of-flight measurements are performed using the inflow effect of the blood to the imaging slice. The spins from the stationary tissue and the inflowing blood is exposed to RF excitation pulse and the difference in RF exposure between the stationary and moving spins lead to the inflow effect. Stationary spins get saturated with repeated RF excitation of a section which leads to low steady value for longitudinal magnetization and results in low signal in the images obtained. Inflowing blood entering the section consists of fresh longitudinal magnetization (Mz = 1) producing signal of high intensity in the region of flow (Figure 3.2). The signal intensity obtained for every pixel is dependent on the refreshing rate of the blood which is a function of velocity, slice thickness and TR. Further, this method is also dependent on the excitation flip angle and T_1 of blood to provide high signal intensities [37, 38]. The images are reconstructed with maximum intensity projection (MIP) technique which is sensitive to high signal from the inflowing spins. In MIP, high-intensity signals from the blood vessels in different sections are added to provide an angiogram. Over the years, there has been further development of modified pulse sequences for TOF angiography [39–42] attempting to provide high contrast images of blood vessels. TOF methods have drawbacks such as long acquisition time, inability to image small vessels, venous contamination and representation of false stenoses [43].
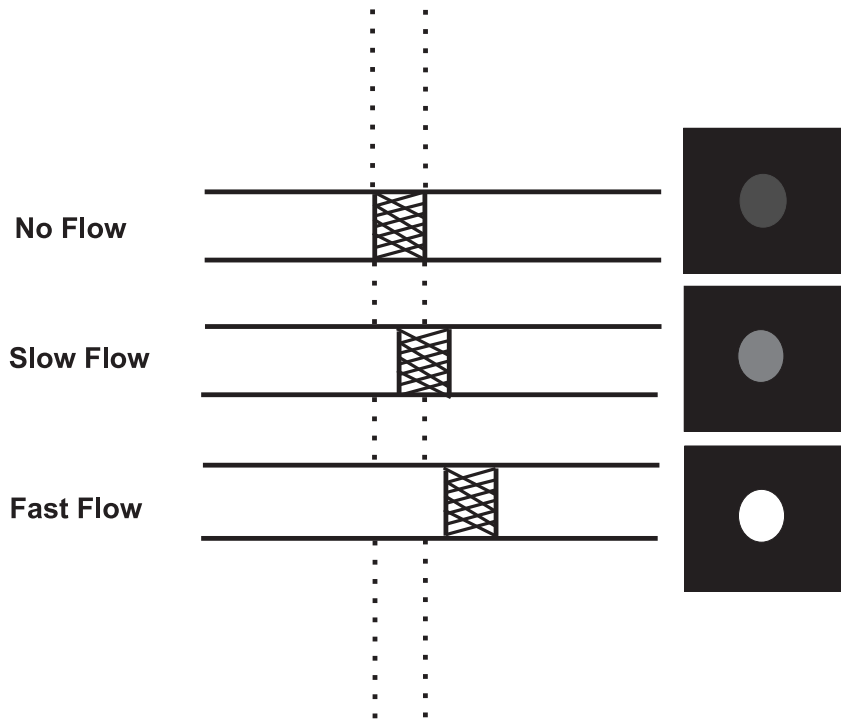
17

Figure 3.2: Pictorial representation of the inflow effect during repetition interval which has an influence on the time-of-flight (TOF) measurements. The contrasts obtained from the imaging plane are dependent on the flow conditions.

3.2.3 Selective Tagging

Selective tagging is an angiographic method which uses a saturation pulse to selectively tag the longitudinal magnetization of inflowing blood. The tagging of spins induces differences in the longitudinal magnetization between flowing or stationary spins that result in better contrast to differentiate blood vessels from surrounding regions [38, 44]. Tagging of spins is followed by the readout of the blood entering the imaging slice with a conventional sequence and reconstruction through maximum intensity projection. Figure 3.3 shows the effect of tagging pulses on the blood vessels of the brain. Both arterial and venous blood vessels are observed when tagging pulses are not used. The stationary regions have minimal signal due to repeated application of RF pulses and low longitudinal magnetization. To obtain only the representation of arterial blood vessels, the tagging saturation pulse are placed on the upper regions of the brain where the venous outflow is present, and for imaging the venous blood vessels, the saturation pulses are applied to arterial inflow in the region of the neck. Tagging method is used for vessels such as renal arteries, hepatic arteries and the portal system.
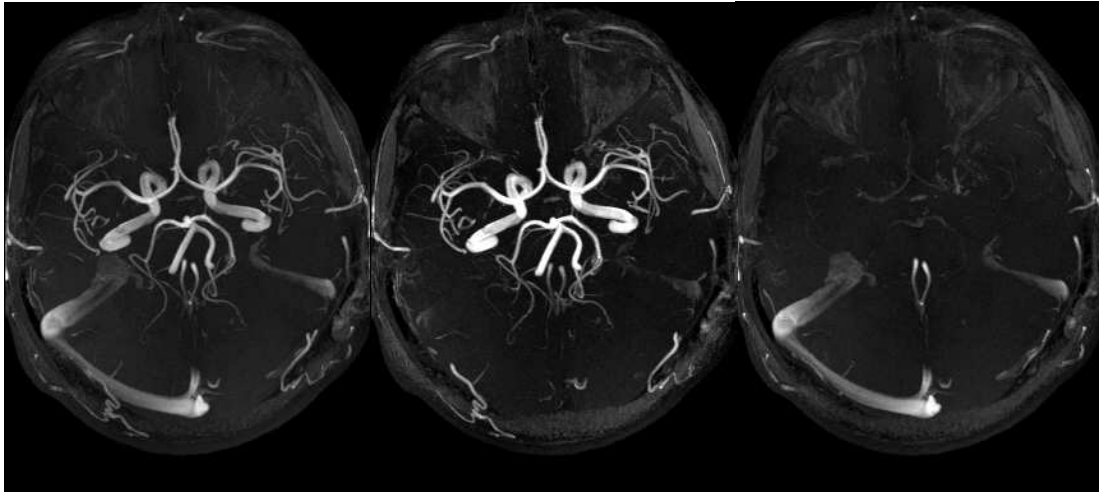
Figure 3.3: Maximum intensity projection (MIP) images representing tagging of blood in the specific regions of the human brain. Images obtained without tagging (left) consist of arterial and venous flow, (center) after venous tagging and (right) after arterial tagging.

3.3 Quantitative Flow Methods

The angiographic methods as explained in the previous section, produce qualitative images of blood vessels without much additional quantitative information. Over the years the development of techniques in MRI has made it possible to acquire quantitative and functional information of many physiological processes. Quantitative flow information is of great importance as it provides flow parameters which can be used for the diagnosis of diseases. In this section, phase-contrast imaging and Fourier flow imaging, used to obtain quantitative MRI flow information, are discussed along with the merits and demerits.

3.3.1 Phase-contrast Imaging

Phase-contrast imaging (PC MRI) is a technique which images the magnetized moving spins [32–34,45] thereby obtaining quantitative flow information. This is achieved by the introduction of a bipolar flow encoding gradient, after the RF excitation pulse and slice selection gradient, to encode the velocity of the moving spins. The velocity of the moving spins is translated into phase of the image by the flow encoding gradients and is directly proportional to the velocity of the moving spins. The flow gradients can be placed in any physical gradient axis to achieve flow sensitivity in the respective direction. In fact, flow gradients can even be applied simultaneously in multiple axes to obtain flow sensitivity in an arbitrary direction. Phase data obtained from the different MRI techniques is influenced by factors like B_0 inhomogeneities and eddy currents. In order to reduce these effects in PC MRI, two images are acquired as shown in Figure 3.4. The first image is acquired with the flow gradient and the second image either

without or toggled flow gradient.

The complex values of the two images are subtracted on pixel basis. The subtraction process has an advantage as it removes the background signal from stationary tissue and other unwanted phase errors. Two different methods can be employed to subtract the complex values from PC MRI such as complex difference [46] and phase difference method [33, 47]. Complex difference method, as the name suggests, performs the subtraction of the two complex data either in k-space or in image domain. The complex difference method can provide qualitative images to view the presence of the moving spins or flow present in the imaging plane and is robust to partial volume effects. However, it cannot be used to either visualize the direction of moving spins or quantify flow parameters for a region of interest. The phase difference operation is performed pixel-by-pixel on the two complex datasets and subsequently the phase is extracted through argus tangens of the resultant complex data [48]. Intensity of each pixel of the phase difference image represents the velocity and direction of the moving spins. Due to additional values or information obtained, phase difference method is used for quantitative analysis. The phase difference image is also called in other names such as phase-contrast map, velocity map or phase velocity map. The complex data obtained after the phase difference operation provide an opportunity to get magnitude images along with phase-contrast maps. The magnitude image can be used for qualitative evaluation of the anatomical information and segmentation of a region of interest by post processing software.
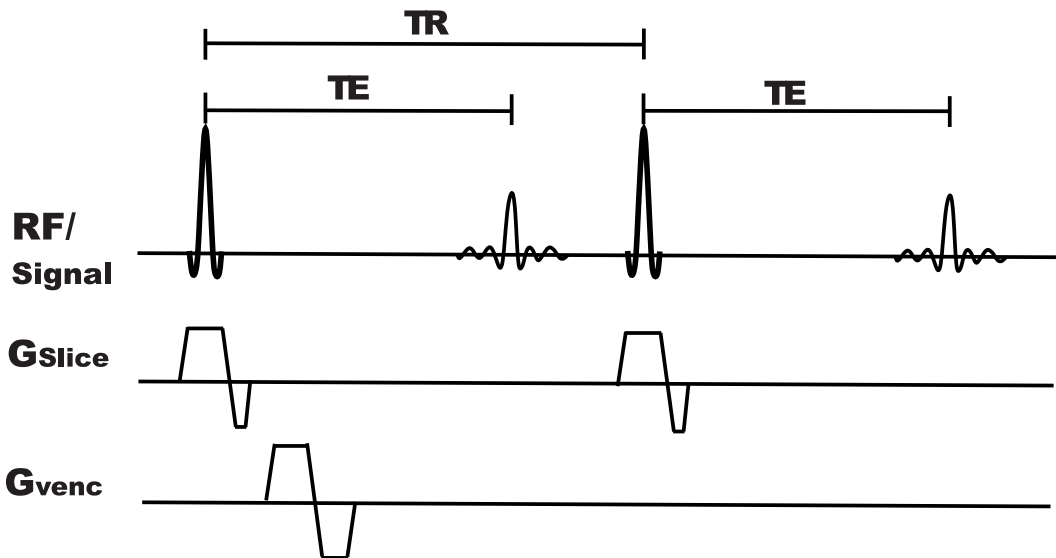

Figure 3.4: Schematic representation of the phase-contrast MRI acquisition process for producing a phase-contrast map. Phase-contrast MRI relies on two image acquisitions with and without velocity-encoding gradient (G_{venc}). G_{slice} represents the slice-selective gradient.

PC MRI has primarily been used to image and quantify blood flow, especially with respect to the cardiovascular blood system. However, it can be used for variety of functional studies such as cerebro-spinal fluid or even motion where constant and periodic movements of spins are involved. Further, these studies can even be extended to three-dimensional velocity mapping to study flow in multiple directions.

3.3.2   Fourier Flow Imaging

Fourier flow imaging is based on the principle of using bipolar gradients to encode velocity as in phase-contrast imaging [32, 49]. Here, the amplitude of the bipolar gradients are increased or incremented in steps similar to phase-encoding gradients in Cartesian encoding scheme. Each bipolar gradient step encodes a certain velocity range in the resultant images. The methods using the bipolar gradients are generally termed as 3D acquisition techniques as the acquired data represent two spatially encoded directions and one velocity encoded direction. In Fourier flow imaging, as shown in the Figure 3.5, an additional Fourier transform is performed on the acquired set of flow-encoded images along the flow-encoding direction. Each reconstructed Fourier flow image represents the moving spins within a certain velocity range.
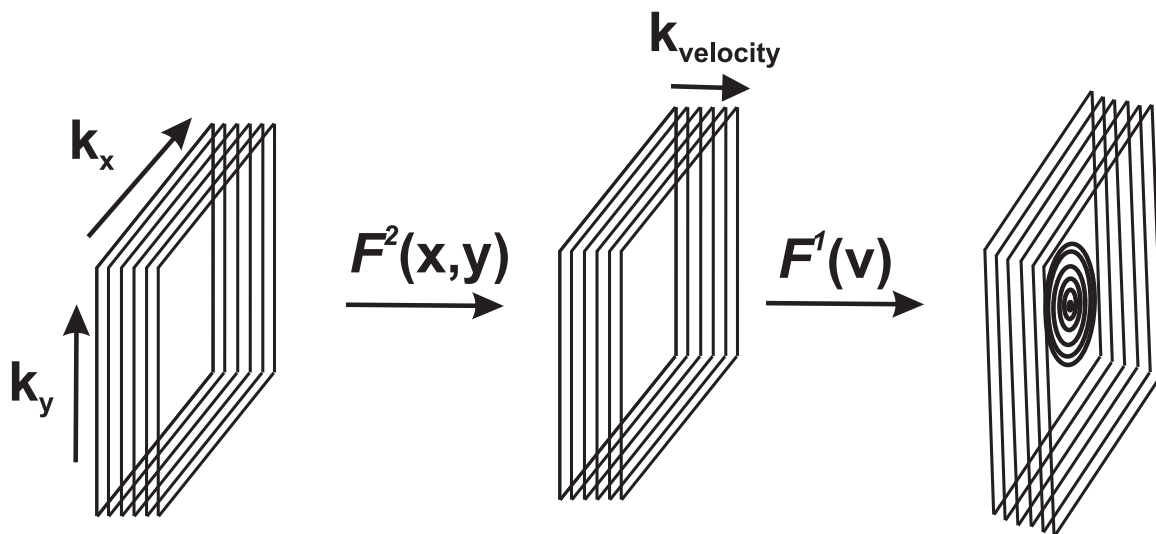

Figure 3.5: Schematic representation of the Fourier flow reconstruction process.   Two-dimensional Fourier transformation for image reconstruction is followed by additional Fourier transformation in the velocity dimension to obtain images for specific velocities.

Fourier flow imaging provides good representation of the range of velocities of moving spins along with qualitative information of the blood vessels and is less prone to partial volume effects. Although Fourier flow imaging has been used to evaluate peak velocity in some studies [50, 51] it is generally not preferred for in vivo imaging due to its long acquisition time. Moreover, in order to obtain precise quantification of velocity in a pixel, the flow sensitivity has to be

increased through additional bipolar gradient steps.

3.4 Summary

An overview of the flow-based MRI methods was introduced in this chapter. These techniques are used for diagnostic imaging depending on the qualitative or quantitative information provided. Ideally, a technique which yields both qualitative and quantitative information would be preferable. Angiographic techniques are good at providing qualitative information of the blood vessels but lack in providing quantitative information of moving spins. In contrast, phase-contrast and Fourier flow imaging, though developed mainly for quantitative imaging, also provide qualitative information. Fourier flow imaging has a drawback of long acquisition time which has limited scope of improvement in methodology due to the use of multiple steps of bipolar gradients. Phase-contrast imaging is also hindered by long acquisition time due to two phase images acquired. But this drawback can be overcome by employing advanced acquisition and image reconstruction methods and thereby achieving real-time imaging.

Chapter 4

Real-time Radial FLASH MRI

Real-time MR imaging of moving spins focuses on the observation of dynamic processes such as in the human cardiovascular system. This is realized through the efficient acquisition of qualitative images at a short span of time. To achieve real-time imaging, specific strategies for image acquisition and reconstruction processes have to be employed. The general acquisition and reconstruction techniques employed for fast MR imaging are discussed in this chapter. Greater focus is placed on the introduction of radial FLASH and regularized nonlinear inversion reconstruction (NLINV) techniques, which will be used in the subsequent chapters as the basis for achieving real-time phase-contrast imaging.

4.1 FLASH Sequence

The FLASH pulse sequence is a gradient-echo technique where low flip angle RF pulses with short repetition time [20,21] are used to produce T_1-weighted images [52]. Low flip angle helps in rapid recovery of magnetization thereby reducing the time spent before the next excitation. In the steady state, the FLASH technique with short TR produces more signal in comparison to conventional gradient-echo imaging. In comparison to spin-echo, FLASH is more sensitive to field inhomogeneities and susceptibility differences. On the other hand it provides several advantages such as reduction in acquisition time due to short TR, lower specific absorption rate (SAR) and extra contrast due to imaging at in-phase and opposed-phase conditions [53]. Further, the properties of gradient-echo imaging such as inflow effect producing bright intensities from moving fluids is retained for FLASH. Over the years, many pulse sequences have been developed based on FLASH focusing on consecutive excitation pulses and the resulting steady state situation often known as steady state free precession (SSFP) [54].

Although steady state can be achieved within the FLASH technique, the dephasing of transverse magnetization is incomplete after every acquisition. This problem is overcome by the

application of RF spoiling and gradient spoiling. RF spoiling [55] changes the phase of the RF pulse for each transmit-receive cycle. Gradient spoiling [56] uses spoiler gradients with different strength for each line acquired in the k-space to remove the residual magnetization that remain after the application of RF spoiling. In this thesis, the radial scheme was combined with fast low angle shot (FLASH) pulse sequence for the implementation of phase-contrast imaging. For radial encoded FLASH acquisitions as displayed in Figure 4.1, no additional spoiler gradient is required as gradient spoiling is self achieved through the applications of varying read gradients(G_x, G_y) for each TR interval. The radial FLASH sequence used as a foundation for this thesis is based on the extensive studies on radial acquisitions by Block [57]. Zhang [58] extended this radial FLASH sequence for real-time MRI.
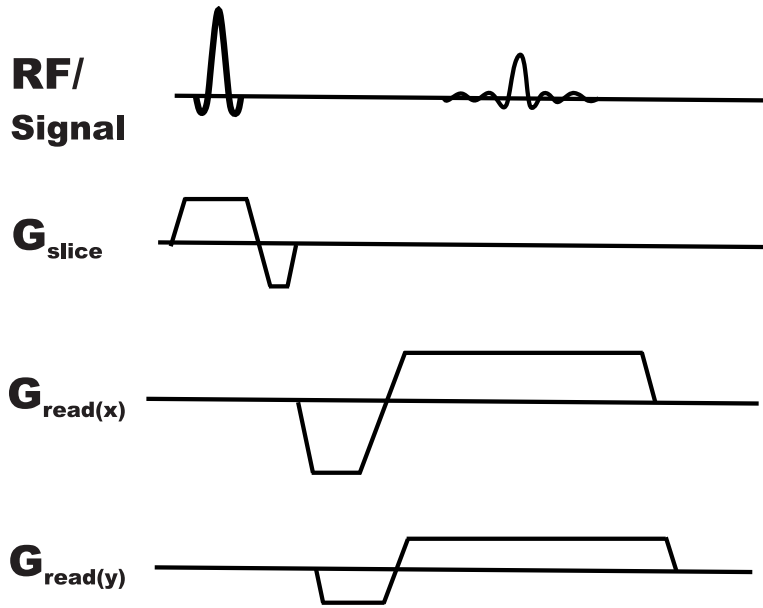

Figure 4.1: Pulse sequence diagram of radial FLASH gradient-echo sequence.

4.2 Radial Sampling

Radial sampling scheme as introduced in the chapter 2 consists of several advantages which can be utilized for real-time dynamic imaging [59]. Unlike Cartesian scheme, the number of radial spokes used are not dependent on FOV and base resolution. The number of spokes that needed to be acquired to maintain Nyquist criterion of sampling is defined by the equation

$$N_{spokes} \geq \frac{\pi}{2} \cdot BR \tag{4.1}$$

where BR is the base resolution. Undersampled radial acquisitions result in streaking artifacts especially on the outer regions of the image [60]. Moreover, the point spread function (PSF)

of the radial scheme is independent of the spoke count and is broadened under undersampling [57]. Further, radial sampling involves the equal distribution of different spatial frequencies in every spoke and oversampling of the center of k-space thereby providing robustness at high undersampling and motion [12, 61]. Unlike the Cartesian scheme, the readout oversampling is performed in both dimensions for the radial sampling which helps in avoiding the aliasing artifacts that arise from distant sampling points. This property provides an opportunity to image regions centrally located without any corruption from aliasing effects.

4.3   Radial Reordering Scheme

Radial views or spokes are acquired in a certain view order to fill the k-space. The simplest method to fill the k-space is the acquisition of radial spokes in a sequential order with a certain interval in the azimuthal direction. The view order plays a major role in dynamic imaging as the motion of the object within the field of view may lead to signal inconsistencies. The distribution of radial spokes in k-space and different types of view order had been studied extensively by Zhang [58]. Interleaved reordering uniformly distributes the spokes between consecutive k-space acquisitions for effective usage of spatio-temporal information. However, sequential reordering scheme (Figure 4.2) along with 5 radial turns was experimentally found to be optimal for dynamic imaging. In addition, the reordering scheme assists the reconstruction algorithm in removing the streaking artifacts effectively from the images.
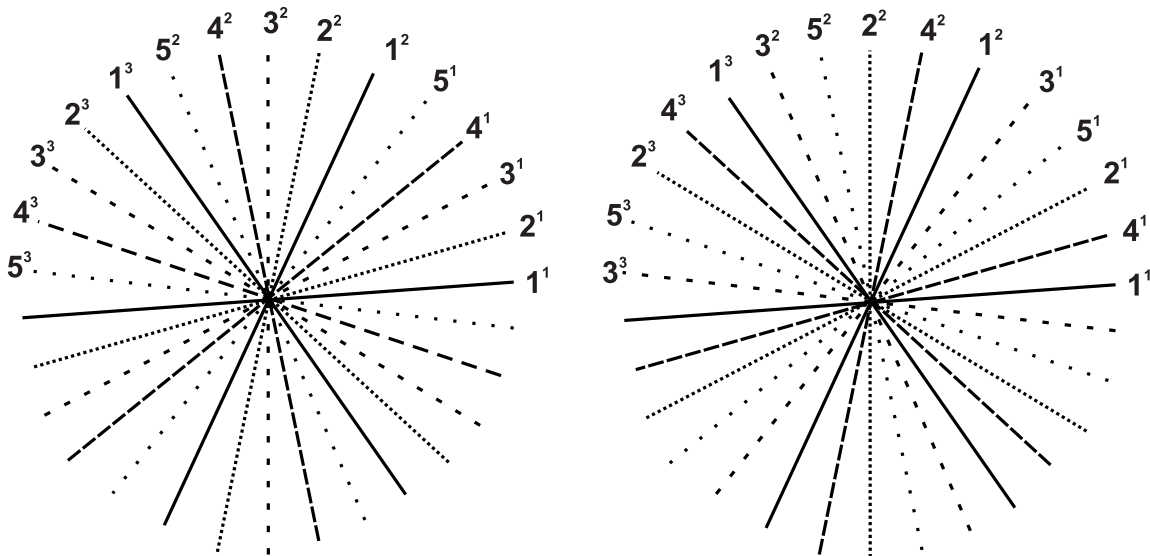

Figure 4.2: Schematic representation of the (left) sequential and (right) interleaved reordering schemes for the acquisition of 5 radial turns each with 3 radial spokes.

4.4   Image Reconstruction

Reconstruction of the non-uniformly sampled radial k-space data can be performed through gridding and FFT. For achieving real-time imaging, the reconstruction process has to focus on obtaining desirable images with undersampled k-space data. This section introduces the sliding window FFT and parallel imaging techniques that are employed for reconstructing the real-time radial data.

4.4.1   Sliding-window Technique

Real-time imaging can be achieved by increasing the frame rate through sharing of radial spokes between the multiple frames, often referred to as sliding-window or view sharing. It is used by acquisition techniques such as keyhole imaging [62], partial k-space updating and segmented k-space cardiac acquisition [63–65] to reduce the overall acquisition time. For radial MRI, the sliding-window reconstruction separates acquisitions into periodic repetition of group of views that can be referred as *radial turns*. A certain number of the acquired radial spokes are shared between adjacent frames within the radial turn resulting in pseudo-increase of temporal resolution. The reconstruction of individual images are performed after regridding procedure using FFT. The image reconstruction and update rate is increased by a factor of the number of frames per turn. Since the number of spokes per frame remains constant, there is no loss of spatial resolution in the reconstructed images and therefore sliding-window reconstructions are usually used for real-time acquisitions to detect changes within the object such as motion [58,66].

4.4.2   Parallel Imaging

Parallel imaging is a general technique developed in MRI to combine and accelerate the information acquired through multiple receive coils. The development of parallel imaging started with the introduction of phased-array coils for the signal acquisition which aid in achieving higher SNR with small surface coils [67]. The small coils aid in efficient acquisition of signals from nuclear spins in a localized region thereby increasing the SNR. It is generally considered that the SNR increases proportionally to the number of phased-array receive coils used. Data acquired from each coil can be reconstructed independently by Fourier transformation. The MRI signal obtained from different coils can be represented through the following equation

$$s_j(t) = \int \rho(x)c_j(x)e^{-2\pi i k(t)x}dx \qquad\qquad j = 1,\dots,N. \qquad\qquad (4.2)$$

where $\rho(x)$ and c_j are proton density and coil sensitivity, respectively. $k(t)$ represents the k-space trajectory. Equation (4.2) can be considered as a forward problem of image reconstruction and represented as

$$y = \mathbf{F}x \qquad (4.3)$$

where y is the data, x is the unknown image. Therefore, the reconstruction of x is a linear inverse problem. $\mathbf{F}$ is the forward operator consisting of three components denoted by

$$\mathbf{F} = \mathbf{P}_k \mathcal{F} \mathbf{C} \qquad (4.4)$$

where $\mathbf{P}_k$ is the projection onto the trajectory. $\mathcal{F}$ and $\mathbf{C}$ represents the Fourier transform and the coil sensitivities, respectively.

Parallel imaging is mainly designed to use the spatial information of coil sensitivities provided by different coils to replace or substitute the missing lines in k-space. This ability to work with undersampled data reduced the acquisition times and are widely used in the clinical environment by factors of 2-3. For Cartesian scheme, the lines of k-space are reduced in the phase-encoding direction and for 3D imaging the lines are reduced in both phase encoding directions.

The methods of parallel imaging can be generally divided into groups depending on the domain (image or Fourier) where the reconstruction is employed. These reconstruction techniques rely on the numerically predetermined coil sensitivities from multiple coils to reconstruct the image. This approach converts the reconstruction process, as shown in Equation (4.3), into a simple linear inverse problem which simplifies the image reconstruction. Parallel imaging methods in the image space, introduced initially as SENSE [68], exploit the decoupling of the linear system of equations in the image space into large number of small linear equations to obtain regular sampling patterns. On the other hand, k-space methods are based on the sparse approximation of the inverse in the Fourier domain [69]. SMASH [70] and GRAPPA [71] are the important parallel imaging techniques which operate in the Fourier domain. SMASH technique expresses missing samples approximately as a linear combination of nearby k-space samples from all coils. GRAPPA is an extension to SMASH technique where the missing samples can be approximated as a linear combination of nearby k-space points. Calibration scans are additionally acquired for these techniques to create coil sensitivity profiles. These reference scans are mainly obtained from a low resolution image consisting of reference lines at the center of the k-space. Auto-calibration methods have been employed to find the weights directly from some fully sampled lines in the central k-space as against external reference lines [72, 73]. Parallel imaging techniques in general need accurate coil sensitivity profiles to derive the missing information of the undersampled data. The coil sensitivities are usually obtained from reference scans under the assumption that the acquired profiles are constant over time. However, in most of the in vivo

studies, the subject or the region of interest could have voluntary or involuntary movement leading to inconsistent coil sensitivity profiles and therefore additional reference scans have to be performed subsequently.

Many new methods in parallel imaging have been developed recently such as k-t Blast, compressed sensing, regularized nonlinear inverse reconstruction (NLINV) which employ different strategies to reconstruct the images. These techniques employ iterative methods during the reconstruction process to find a solution from a linear or nonlinear system. k-t Blast [74] technique utilizes correlations in k-space and time to obtain a time-average composite image from all acquired data which is used as a training dataset to reduce artifacts and improve the reconstruction process. Compressed sensing [75] relies on regularization techniques and sparse representations to effectively remove the noise distributions and increase image content. This technique is supported intrinsically by wavelet transformation and nonlinear inverse reconstruction process. NLINV is a reconstructed method for autocalibrating parallel MRI which estimates the image content and coil sensitivity simultaneously. This is advantageous for real-time applications as motion is challenging for other techniques, which rely on pre-scan calibration data. NLINV has been successfully applied recently for real-time imaging of many anatomical structures [66, 76–78]. Since it is an established technique in real-time imaging, it is adapted in this thesis for real-time phase-contrast imaging.

Regularized Nonlinear Inverse Reconstruction (NLINV)

Regularized nonlinear inverse reconstruction is an iterative reconstruction technique which was recently introduced in the field of MRI by Uecker et al. [69,79]. NLINV simultaneously estimates the image content ρ and coil sensitivities c_j by formulating the reconstruction process into a non-linear inverse problem

$$F(\rho, c_j) = y \tag{4.5}$$

where y is the measured data. The NLINV reconstruction is based on iteratively regularized Gauss-Newton-Method [80] and incorporates additional penalties to constrain the solution. The reconstruction process involves the minimization of cost function

$$\parallel F(\rho, c_j) - y \parallel^2 \; + \; \alpha \parallel \rho - \rho^0 \parallel^2 \; + \; \alpha \parallel W(c_j - c_j^0) \parallel^2 \tag{4.6}$$

where α represents the regularization parameter involved. Regularization parameter α in the Equation (4.6) is reduced during each iteration or Newton step according to $\alpha_n = \alpha_0 q^n$ with q ϵ (0,1) [69]. W is a weighted discrete Fourier transform that constrains the coil sensitivities to

provide smooth coil sensitivity profiles. The weighting operator W is of the form $(1+W_c \mid k \mid^2)^{16}$ (with $-0.5 < k_x k_y < 0.5$) where W_c represents a constant [76, 81]. The initial guess for ρ^0 and c_j^0 as in Equation (4.6) is chosen to be 1 and 0, respectively.

For the reconstruction of serial image acquisitions, the reconstruction process is extended to temporal regularization where the previous frame is chosen as the initial estimate for proton density and coil sensitivities. The previous frame is used for temporal regularization after multiplication with a dampening factor. Dampening factor adjusts the degree of temporal regularization. The final step involves the application of a pixel-wise temporal median filter over the image series during post processing. The median filter is applied to n frames depending on the window size and is centered around the present frame. Temporal regularization and median filter are important components for achieving qualitative real-time images without streaking artifacts. The reordered acquisition is another core component of NLINV reconstruction process. Temporal regularization relies on the different information in each frame obtained through reordered acquisition. Median filter effectively removes the remaining streaking artifacts that flicker between the frames after the reordered acquisition and NLINV reconstruction [76, 82].

Although NLINV reconstruction process is time consuming, recent advances in mathematics and technology such as principal component analysis (PCA) [83, 84] and graphical processing units (GPU) have drastically reduced the reconstruction time. GPUs consists of large number of parallel processors to process simultaneously large blocks of MRI data resulting in faster reconstruction of images [81, 85–88]. PCA compresses the data collected from multiple receiver coils to 10 virtual channel data for the NLINV reconstruction process [69, 81]. Application of PCA before the reconstruction process does not affect the reconstructed images as the maximum energy is preserved by the chosen virtual channels. These additions help in achieving nearly real-time online display of the reconstructed images.

4.5   Summary

Real-time imaging consists of a combination of different techniques covering efficiently various aspects of pulse sequence, encoding schemes and reconstruction methods. Radial encoding scheme has several advantages such as robustness to undersampling and less sensitivity to motion which are beneficial for real-time studies. Radial encoding scheme was combined with FLASH technique which is a fast, efficient pulse sequence and can be used as a foundation for the development of real-time phase-contrast imaging. This chapter also provided an overview of the reordering schemes and sliding-window FFT reconstruction with respect to radial encoding scheme. Parallel imaging, common to today's MRI acquisitions, was also discussed. NLINV

reconstruction, which is used in this thesis, utilizes advanced reconstruction methods and acquisition schemes effectively to produce qualitative images from highly undersampled data. It has to be noted that the sliding-window technique is not used by NLINV reconstruction. However, the radial turns from the acquisition have been effectively used in combination with the reordering scheme to reduce residual streaking artifacts by median filtering. The techniques introduced in this chapter will be used subsequently for the development and evaluation of real-time phase-contrast imaging.

Chapter 5

Development of Real-time PC MRI

Real-time imaging using radial FLASH and NLINV as described in chapter 4 has become a potential method to monitor moving anatomical structures in the human body. The motion produced by these structures can be voluntary (task-driven) and involuntary (such as the cardio-vascular movement) in nature. Recent studies have shown real-time imaging provides valuable qualitative information which is advantageous in clinical environment [66,77,78]. Similarly, real-time PC MRI could provide more quantitative information which may not be obtained from standard PC MRI sequences. The development and in vivo validation of real-time PC MRI using radial FLASH and NLINV reconstruction will be discussed extensively in this chapter.

5.1 Sequence Implementation and Optimization

The development of real-time PC MRI method primarily involves the implementation of real-time PC MRI pulse sequence and its adaptation to NLINV reconstruction technique. Further the optimization of the real-time PC MRI has to be performed to obtain high spatial and temporal resolutions. This section focuses on different areas of development such as evaluation of the sequence parameters, comparison of encoding schemes, sequence optimization, evaluation of the real-time PC MRI pulse sequence and the analysis of the NLINV reconstruction parameters.

5.1.1 Experimental Setup

MRI System

In vitro and in vivo studies were performed on a commercially available scanner (MAGNETOM TimTrio System, Siemens AG, Erlangen, Germany). The scanner consists of a bore of length 142 cm and diameter 60 cm with achievable Field of View (FOV) of 50 cm in each direction.

The bore essentially contains the superconducting magnet of field strength $B_0 = 2.89$ T and body coil for RF excitation. The gradient system can achieve a maximum gradient strength of 38 mT m^{-1} per axis and is switched on a 10 μs raster with a maximum slew rate of 170 T m^{-1}s^{-1}. Body coils within the bore and separate coils, which are part of RF system, are used for excitation and receiving resonance signals for data acquisition respectively. However, separate single or multi-channel RF receive coils are also available in different configurations depending on the application. In vitro studies were performed with single channel CP and 32 channel head coil, whereas for in vivo studies 32 channel RF receive cardiac coil consisting of 16 anterior and 16 posterior array elements were used as shown in Figure 5.1.

Figure 5.1: MRI System (top) and receiver coils (bottom) used in this thesis. 32-channel head coil (bottom-left) and 32-channel body coil (bottom-right) with its 16 anterior and posterior elements.

Phantom

Phantoms used for real-time PC MRI can be divided into two categories as stationary and flow phantoms according to the intended purpose (Figure 5.2). Stationary phantom is used to evaluate the influence of basic sequence parameters whereas flow phantom was used for studies on moving spins. The flow phantom consisted of two stiff tubes with inner diameters 20 mm and 10 mm placed inside a plexiglass. The region between the tubes and plexiglass box are filled with stationary water. The velocity of water or the moving spins flowing through the tubes are proportional to the diameter of the tube. The flow phantom was designed to study the effects of constant and pulsatile flow on the phase-contrast maps. The diameters of the tubes were in accordance with the blood vessels such as aorta or pulmonary artery in the cardiovascular circulation system.

The inflow and outflow through the flow phantom is achieved by an electrical pump (Lux Plus KTW270, Herzog, Göttingen, Germany) which is connected to a computer controlled power supply (Voltcraft 12010, Hirschau, Germany) for adjusting the flow rate (l min^{-1}). The flow rate is independently measured by an external flow meter (FCH-C-PA, BioTech, Vilshofen, Germany) of accuracy $\pm$ 0.05 l min^{-1} outside the magnetic field of the scanner. Double distilled water was used as flowing medium. Before entering the phantom, water is passed through 15 m closed looped tube placed inside the magnet for fully magnetizing the moving spins. The length of the closed loop tube was chosen in accordance with the T_1 relaxation time of water.

The softwares used for the quantitative analysis of phase-contrast maps were 1) Argus flow analysis tool (Siemens Healthcare, Erlangen, Germany), 2) QFlow 5.4 Prototype Flow analysis (Medis, Leiden, Netherlands), 3) Semi-automatic quantitative flow analysis tools written using MATLAB (Mathworks, USA). For the major portion of this thesis (both in vitro and in vivo studies) Argus Flow analysis tool and QFlow 5.4 Prototype were used.

5.1.2 Pulse Sequence Design

The basic FLASH pulse sequence used for real-time imaging has been explained in chapters 2 and 4. PC MRI as explained in chapter 3 introduces bipolar gradients to image the flow. The basic FLASH PC MRI pulse sequence with Cartesian encoding scheme is shown in Figure 5.3.

Figure 5.4 provides an overview of interaction of the stationary and moving spins to a bipolar velocity-encoding gradient (flow gradient) and the resultant phase accumulated. The phase of the stationary spins returns to the initial phase position at the end of second gradient lobe, i.e.

Figure 5.2: Stationary phantom (left) and flow phantom (right) used for in vitro studies.
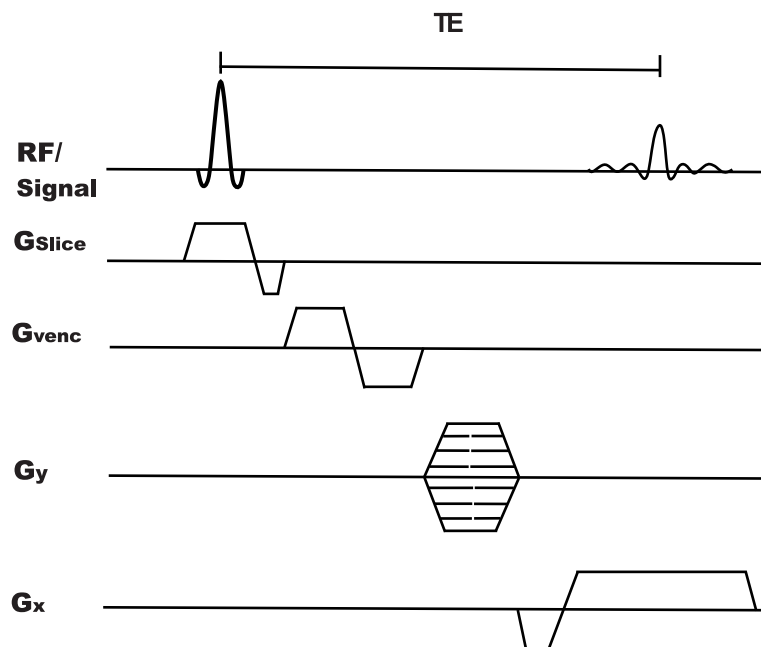

Figure 5.3: Schematic representation of the phase-contrast imaging pulse sequence along with Cartesian encoding scheme. The bipolar velocity-encoded gradient present in the slice direction (G_z) are not overlapped with gradients in other directions.

the net phase accumulated over the duration of flow gradients is zero. On the contrary, the moving spins acquire a net accumulation of phase after the application of flow gradients which is directly proportional to the velocity of the concerned spins.
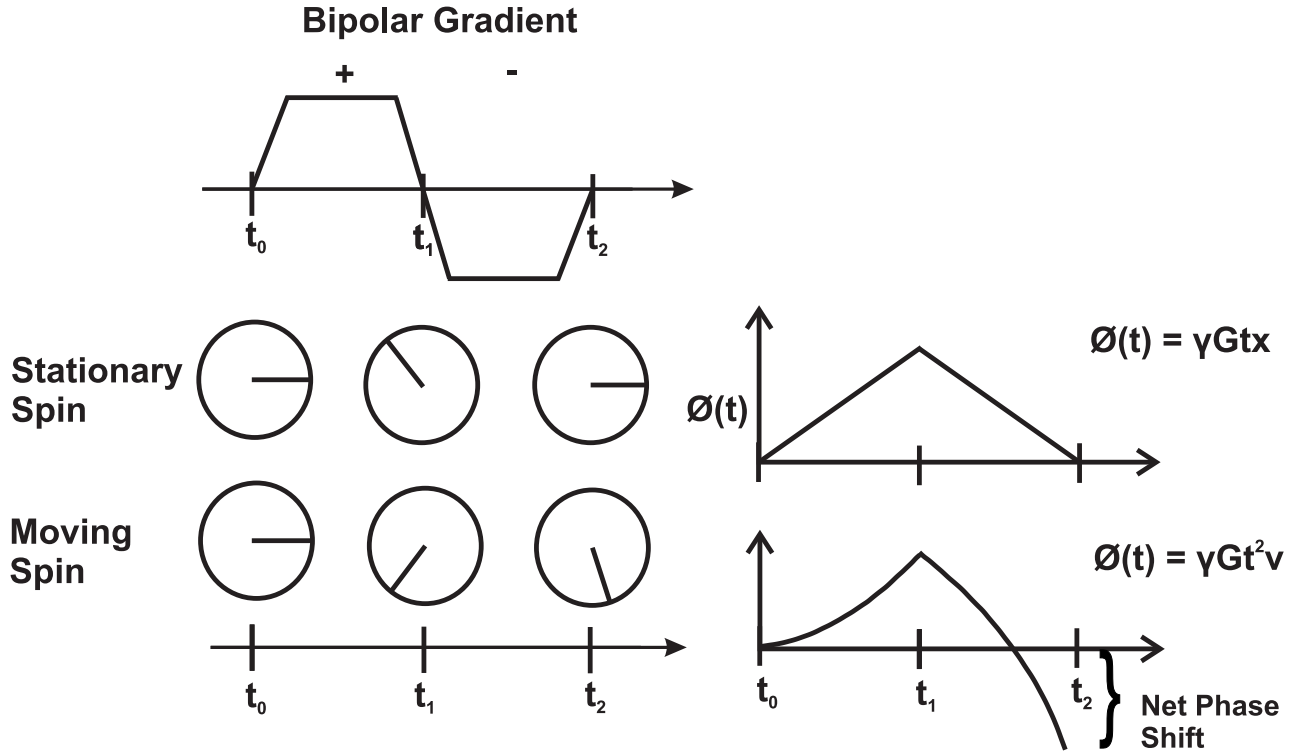

Figure 5.4: Schematic representation of the phase accumulation over time by stationary and moving spins during the bipolar gradients. The net phase accumulated by the moving spin is proportional to the velocity of the spin.

The spin position as a function of time is given by

$$x(t) = x(0) + x_1 \cdot t + \frac{1}{2!}x_2 \cdot t^2 + \cdots + \frac{1}{n!}x_n \cdot t^n \tag{5.1}$$

$$x_1 = \text{velocity}, \; x_2 = \text{acceleration}$$

And the phase accumulation with respect to gradient moment expansion is given by

$$\phi(T) = \gamma \int_0^T G(t) \cdot x(t)dt \tag{5.2}$$

$$= \gamma[x_0 \int_0^T G(t)dt + x_1 \int_0^T t \cdot G(t) \cdot dt + \cdots] \tag{5.3}$$

$$= \gamma[x_0 m_0(T) + x_1 m_1(T) + \cdots] \tag{5.4}$$

35

where m represents the gradient moment. For constant flow velocity the phase is directly proportional to the velocity and is given by

$$\phi = \gamma G t^2 v \tag{5.5}$$

$$\gamma = \text{gyromagnetic ratio}, 2.678 \cdot 10^8 (rad/T \cdot s)$$
$$G = \text{gradient amplitude}$$
$$v = \text{velocity}$$
$$t = \text{duration of flow-encoding gradient}$$

The phase represented by the Phase-contrast imaging (PC) is dependent on the choice of velocity field of view which is given in cm s^{-1} and can be selected by the amplitude and duration of the velocity-encoding gradient. The velocity field of view (VENC) plays a major role in the exact representation of velocities and avoiding the occurrence of phase wrapping artifacts when the accumulated phase exceeds the range $\pm\pi$.

Flow-Encoding Gradients

The amplitude and duration of flow gradients can be calculated from the Equations (5.4,5.5). This formula is derived from the assumption that bipolar flow gradients, in rectangular form, are used in the PC MRI. However, due to the hardware limitations for achieving the rectangular gradients, trapezoidal gradients are preferred in pulse sequences. Therefore the gradient formula for amplitude and duration are recalculated with respect to the moments obtained in trapezoidal gradient waveforms. The trapezoidal gradient waveform consists of three basic units such as ascending ramp time (0 to G gradient strength), descending ramp time (G to 1) and the rectangular section (with G gradient amplitude). This is schematically represented in Figure 5.5 where r, d represents ramp time and flat top time, respectively.

The first-order moment as a continuation of Equation (5.4) for the first trapezoidal gradient from the position 0 to 1 and 1 to 2 is given by

$$\phi_1 \;=\; \gamma G v (\frac{1}{2}d^2 + \frac{3}{2}rd + r^2) \tag{5.6}$$
$$\phi_2 \;=\; -\gamma G v (\frac{3}{2}d^2 + \frac{9}{2}rd + 3r^2) \tag{5.7}$$

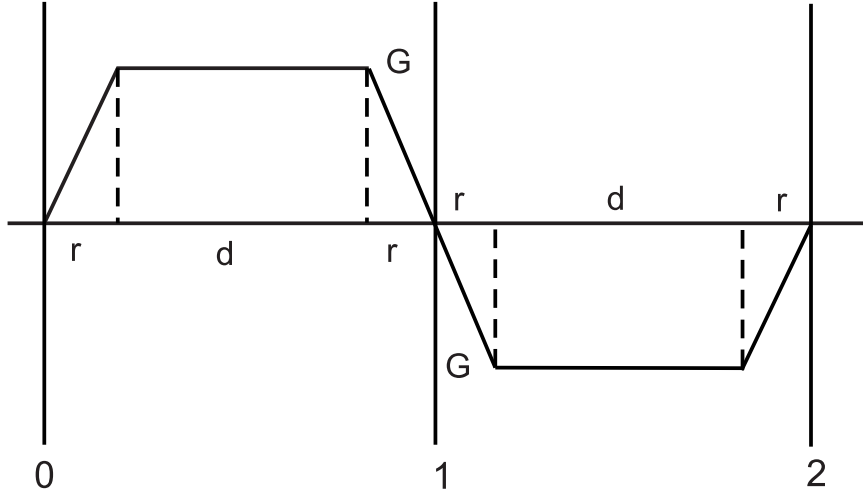The total first order gradient moment for the bipolar flow gradient is calculated as

Figure 5.5: Schematic representation of the trapezoidal bipolar velocity-encoding gradient at different time points such as 0, 1 and 2. Ramp time and flat top time are represented by r, d respectively.

$$\phi = \phi_1 + \phi_2 \qquad (5.8)$$
$$= -2\gamma Gv(d^2 + 3rd + 2r^2) \qquad (5.9)$$

For a single experiment the maximum phase ϕ is equal to π and therefore the flat top time for a single trapezoidal gradient is calculated by

$$\pi = -2\gamma Gv(d^2 + 3rd + 2r^2) \qquad (5.10)$$
$$\frac{\pi}{-2\gamma Gv} = (d^2 + 3rd + 2r^2) \qquad (5.11)$$
$$d = -\frac{3}{2} + \sqrt{\frac{r^2}{4} + \frac{\pi}{(\gamma Gv)}} \qquad (5.12)$$

The ramp time r can further be calculated from the flat top time obtained, previously. The formulas derived above are with respect to independent flow gradients. However, in the case of flow gradients being overlapped with other gradients, these derivations have to be modified accordingly.

Flow-encoding Gradient Modes

Two acquisitions with and without bipolar velocity-encoding gradients are used in phase-

contrast imaging to obtain phase-contrast maps. The acquisition without the bipolar velocity gradient, also called the Zero mode, is generally considered as the reference image for the phase difference operation ($\phi_1 - \phi_2$). However, the reference image can also be obtained by toggling the bipolar velocity gradient referred as Min-Max mode, i.e. the difference of the two gradient shapes results in the desired velocity-encoding gradient. Figure 5.6 shows the schematic representation of the two flow-encoding gradient modes such as Min-Max and Zero-Max played out after the slice selection gradient. The gradient formula calculation is an extension to Equation (5.5) and is given as
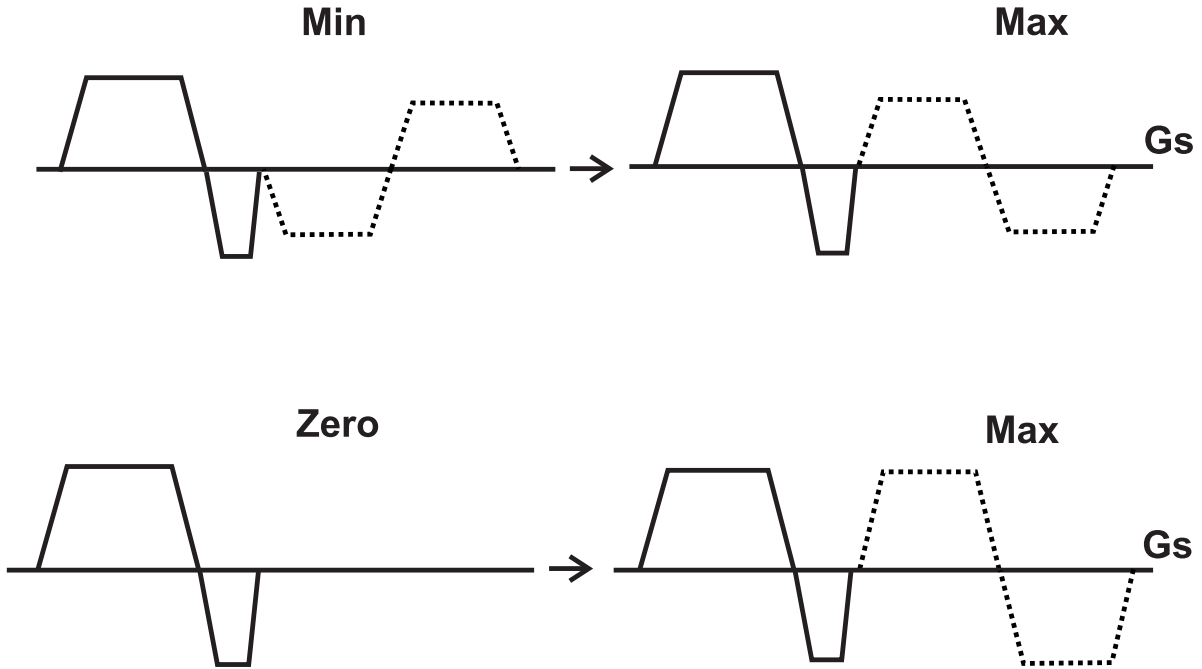
$$\phi = 2\gamma G t^2 v \tag{5.13}$$

Figure 5.6: Schematic representation of the Min-Max and Zero-Max flow-encoding gradient modes used for the acquisition of phase-contrast maps along the slice-selection axis. Independent bipolar velocity-encoded gradient (dashed) is introduced in the slice-selection axis after the slice selection and slice rephasing gradient.

5.1.3 Combining of Multi-channel Data for PC MRI

Multi-channel coils are used in parallel imaging to produce faster acquisitions with higher SNR [89]. The number of coil elements used in parallel imaging differs such as 8, 12, 32 with respect to the application concerned. Specific methods are employed to combine the information from these coil elements and obtain an image. The conventional method for combining multi-channel data is called "Sum of Squares" [67, 90]. The major drawback of this method is

the loss of phase information during the reconstruction process. During the past years, many methods have been developed to combine multi-channel data [91, 92].

Two complex images I_1 and I_2 obtained with and without flow-encoding gradients in PC MRI can be represented in their respective magnitude (A) and phase (ϕ) components as shown in Equation (5.15).

$$I_1 = A_1 \cdot e^{i\phi_1} \tag{5.14}$$

$$I_2 = A_2 \cdot e^{i\phi_2} \tag{5.15}$$

The phase-contrast map $\Delta\phi$ for a single channel receiver coil is calculated as

$$\Delta\phi = \arg(I_1 \cdot I_2^*) \tag{5.16}$$

$$= \arg(A_1 \cdot A_2 \cdot e^{i(\phi_1-\phi_2)}) \tag{5.17}$$

$$= \phi_1 - \phi_2 \tag{5.18}$$

The Equation (5.18) can be extended for multi-channel data where phase difference operation is performed after combining all individual channels.

$$\phi_1 = \arg(\sum_1^n A_{1n} \cdot e^{i\triangle\phi_{1n}}) \tag{5.19}$$

$$\phi_2 = \arg(\sum_1^n A_{2n} \cdot e^{i\triangle\phi_{2n}}) \tag{5.20}$$

$$\Delta\phi = \phi_1 - \phi_2 \tag{5.21}$$

For multi-channel data of PC MRI, Bernstein [48] proposed a unique method to obtain a single phase-contrast map for quantitative analysis. This method consisted of two parts such as 1) performing the phase different operation for individual channels as shown in Equation (5.18) and 2) combination of phase-contrast maps of n channels as shown in Equation (5.22)

$$\triangle\phi = \arg(\sum_1^n A_{1n} \cdot A_{2n} \cdot e^{i\triangle\phi_n}) \tag{5.22}$$

The two methods for obtaining the phase-contrast map as shown in Equation (5.21) and Equation (5.22) were implemented and analyzed for phase-contrast imaging. Figure 5.7 represents

the phase-contrast maps obtained from both methods. It is clearly observed that Bernstein [48] method provides good qualitative phase-contrast map without any artifacts in the regions of flow. Therefore Bernstein method is used in this thesis for combining multi-channel PC MRI data. Additional weighting through the sensitivity profile of individual coils was included before the phase difference operation to smooth phase-contrast maps.
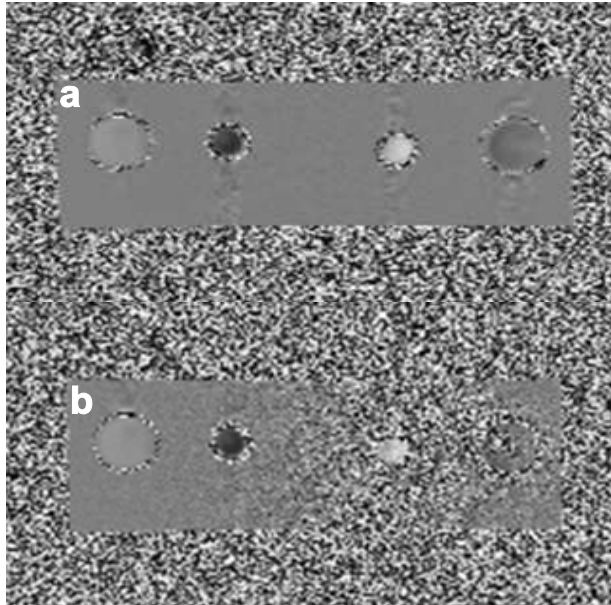

Figure 5.7: Phase-contrast maps obtained from Cartesian encoding scheme for different methods of multi-channel data combination; a) Bernstein Method b) phase difference operation after combining multi-channel data.

5.1.4 Comparison between Cartesian vs Radial Encoding Schemes

The advantages and disadvantages of Cartesian and radial encoding schemes have been briefly discussed in the chapter 2. In PC MRI Cartesian encoding scheme has been used widely in comparison to radial scheme. Therefore qualitative comparison of Cartesian and radial phase-contrast maps is performed for choosing the appropriate encoding scheme for real-time PC MRI. The quality of phase-contrast maps obtained from Cartesian and radial encoding schemes were compared for different acquisition times along with a constant VENC of 150 cm s^{-1}. Shortest repetition time TR and echo time TE were used for the experiments. Radial encoded images were reconstructed for a constant matrix size of 256×256 using the gridding technique. The phase-contrast maps images from both encoding schemes as shown in Figure 5.8 demonstrate their respective artifacts. Cartesian encoding scheme produce motion artifacts along the phase encoding direction whereas streaking artifacts are prominent in radial encoding scheme. It is observed that both encoding schemes provide equivalent qualitative information for images

acquired at longer acquisition time. But at short acquisition times, radially encoded phase-contrast maps show motion robust qualitative information. Further, the radial phase-contrast maps are less sensitive to undersampling in comparison to Cartesian images. Since radial encoding scheme provides robustness and less sensitivity to undersampled data, which are two important properties for achieving real-time imaging, the radial encoding scheme was used for this thesis.
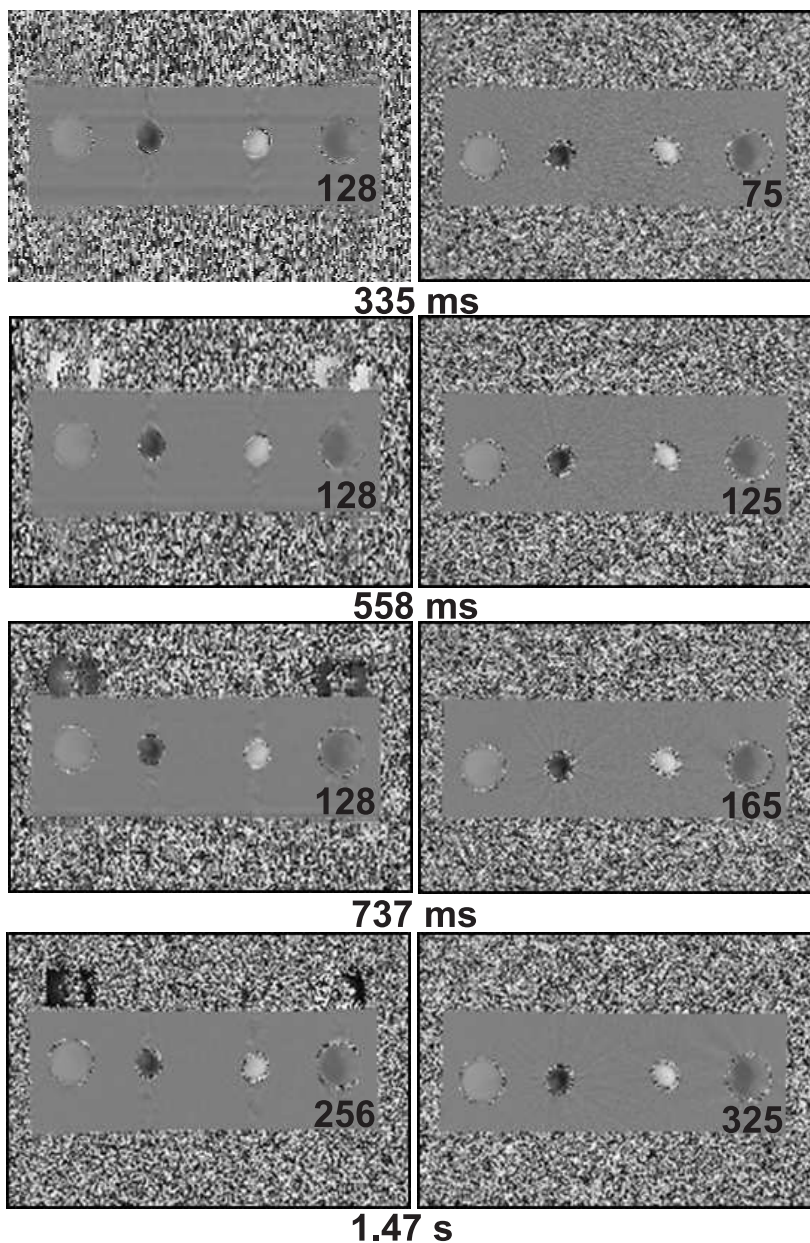

Figure 5.8: Phase-contrast maps obtained from Cartesian (left) and radial (right) encoding schemes at different total acquisition times. The phase-contrast maps were obtained from Cartesian encoding scheme with base resolution 256 and respective field of view as represented. Phase-contrast maps from radial scheme were acquired with different number of spokes as represented in the images.

5.1.5 Comparison between Gridding/FFT and NLINV Reconstruction

Real-time imaging of anatomical structures using radial encoding scheme and NLINV reconstruction technique has been demonstrated previously [76, 81]. In this thesis, the NLINV reconstruction technique was adapted to phase-contrast imaging. Since phase-contrast imaging involves quantitative analysis, no median filter was used to maintain the best possible temporal resolution. The phase-contrast maps obtained from sliding-window FFT and NLINV reconstruction methods were compared qualitatively. The results obtained with shortest TR/TE and spatial resolution of $1.8 \times 1.8 \times 6$ mm^3 from both reconstruction methods for different number of spokes have been displayed in Figure 5.9. It is observed that NLINV provides reasonable phase-contrast maps even at an extremely reduced number of spokes of only 5 spokes.
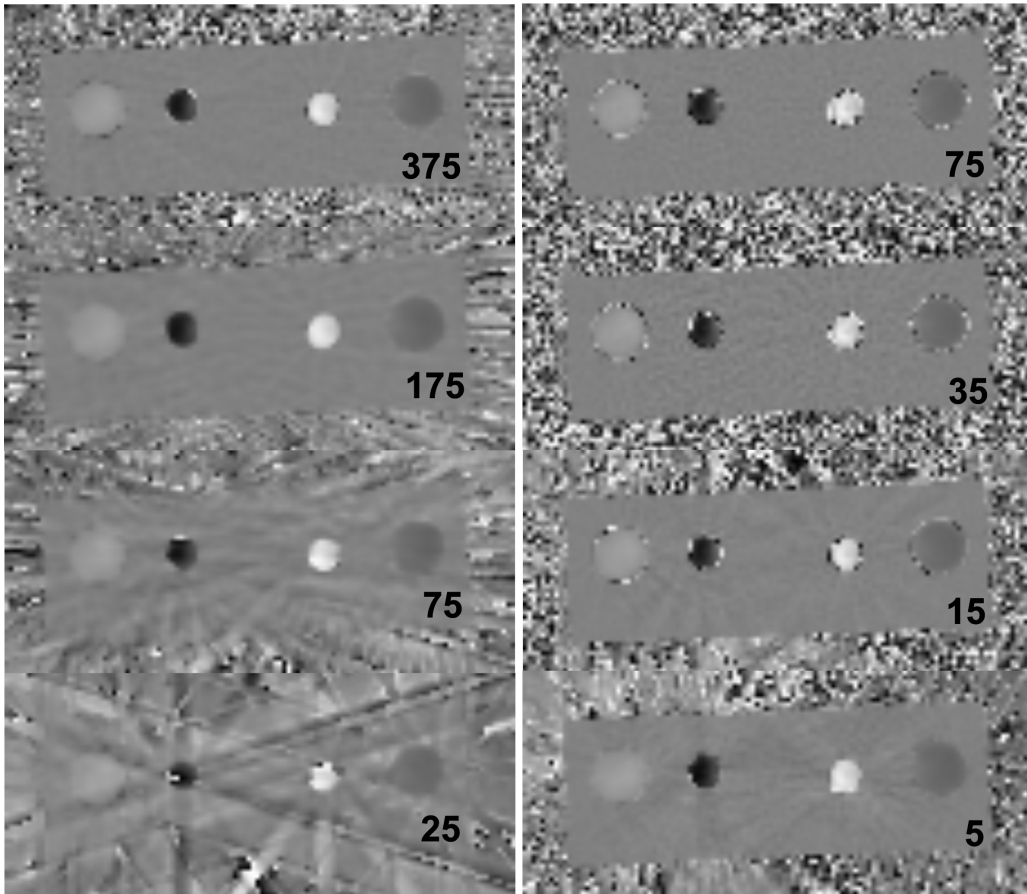

Figure 5.9: Phase-contrast maps obtained for varying number of radial spokes using sliding-window FFT (left) and NLINV (right) reconstruction techniques.

Quantitative analysis was performed on the flow phantom with constant flow rates for evaluation with Argus of 10 simulated heart cycles from sliding-window FFT and NLINV reconstructions

as shown in Figure 5.10. The flow rates obtained from sliding-window FFT and NLINV reconstruction were consistent with the actual flow rate from the flow meter. Minimal deviations for lower flow rates (2 - 3 l min^{-1}) were observed for NLINV reconstructed phase-contrast maps. The minimal deviations of the slow flow measurements may be due to flow enhancement of border voxels also containing static spins. These deviations do not have major influence for cardiovascular analysis of large vessels where flow rates of 5 to 8 l min^{-1} are observed. The consistency of flow rates from NLINV reconstruction with actual flow rate meter values even with highly undersampled radial acquisition demonstrates its applicability for real-time flow imaging.
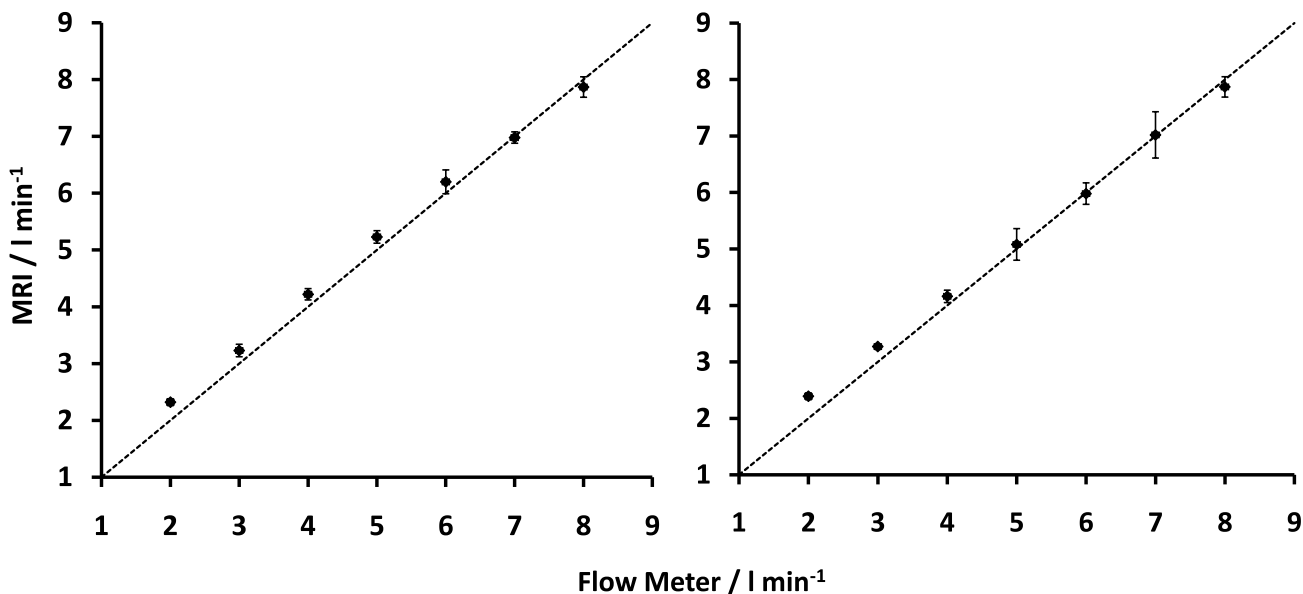

Figure 5.10: Calibration of flow rates obtained from PC MRI using sliding-window FFT (left) and NLINV (right) reconstruction techniques. Analysis performed on phase-contrast maps from 10 continuous heart cycle acquired with simulated ECG trigger stamps.

Comparison between sliding-window FFT and NLINV were also performed on the flow phantom under pulsatile flow condition, as shown in Figure 5.11 which is commonly observed in the human body. Pulsatile flow was generated by a repetitive protocol of high and low velocity flows distributed over 2 s. The scan parameters were TR/TE/α = 3.44/2.68 ms/10°, spatial resolution of $1.8 \times 1.8 \times 6$ mm^3. The number of spokes per phase-contrast map for sliding-window FFT and NLINV reconstructions were 2×35 and 2×7, respectively. Peak velocities obtained across four pulsatile cycles with a temporal resolution of 150 ms are displayed in Figure 5.11. Averaging or broadening of velocity curves was observed for sliding-window FFT while NLINV reconstructed phase-contrast maps due to its higher temporal resolution were capable of estimating the high peak velocities. Further, the flow rates determined manually by bucket and clock method (4.47 l min^{-1}) were in excellent agreement with the experimentally determined values (4.38±0.07 l min^{-1}). The ability to produce both qualitative and quantitative

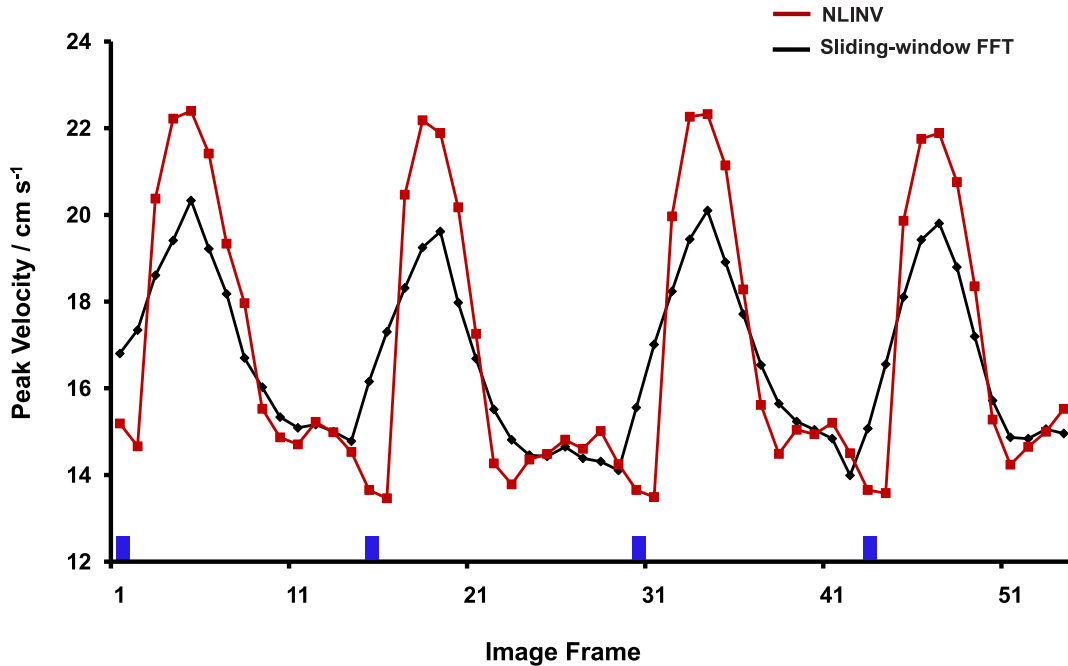information from highly undersampled data makes NLINV reconstruction technique ideal for real-time PC MRI.

Figure 5.11: The effect of pulsatile flow on the peak velocity estimation from the phase-contrast maps obtained from sliding-window FFT and NLINV reconstruction methods. The phase-contrast maps were obtained with a temporal resolution of 150 ms and 750 ms for NLINV and sliding-window FFT reconstructions, respectively.

5.1.6 Evaluation of Sequence Parameters

A large variety of sequence parameters is important for image acquisition. The effect of these parameters under flow conditions has to be analyzed and the sequence optimized accordingly. This section describes and evaluates the important sequence parameters with respect to PC MRI. The results discussed in this section were obtained using Cartesian encoding scheme.

Flip Angle

Flip angle as a sequence parameter influences the angle at which the transverse magnetization vector is tilted after the application of RF pulse. The choice of flip angle has influence on slice profile and SNR of images. The SNR obtained from magnitude images with different flip angles was compared as shown in Table 5.1. The SNR obtained is consistent for flip angles above 15° but reduced to half for flip angle 5°.

Flip Angle	Stationary Spins SNR	Moving Spins SNR
5°	44	45
15°	102	122
25°	118	176
35°	116	205
45°	108	217

Table 5.1: SNR of stationary and moving spins obtained from the magnitude images of PC MRI at varying flip angles.

Further slice profile measurements were performed on a multi-purpose stationary phantom containing two wedges with a known slope ±11.3°. The slice profile obtained at two different flip angles are shown in Figure 5.12. The images were obtained with isotropic in-plane resolution of 1 mm, slice thickness of 4 mm, TR/TE = 8.41/4.99 ms , RF pulse duration 1000 μs and bandwidth time product 2. At flip angle 10° the slice profile is an acceptable Gaussian curve, whereas at higher flip angle it is strongly degraded. At higher flip angles, due to imperfect slice profiles, the possibility of excitation of two nearby slices is high which leads to partial volume effect and wrong representation of velocities. Moreover, it has to be noted that shorter TR can also deform the slice profile due to flip angle and T_1 dependent saturation [93]. Nevertheless, for optimal performance the flip angle between 8 - 10 ° is chosen for flow quantification measurements as it provide homogeneous distribution of phase signal.

Bandwidth / Data Acquisition Time

Receiver bandwidth is an important sequence parameter which influences the acquisition time and the SNR of an acquired image. High bandwidth shortens the acquisition time resulting in increased sampling rate. Influence of bandwidth on the phase-contrast maps has to be studied in order to find the optimal choice which balances the criteria of reduction of TE along with reasonable sensitivity. The reduction of TE help in reducing total acquisition time and minimizing off-resonance effects including phase contributions from acceleration, jerk, or turbulence. Higher bandwidths also reduce artifacts produced by off-resonant spins [94] and chemical shift-induced phase errors [95]. Phase-contrast maps obtained from different bandwidths are shown Figure 5.13. The maximum velocity of flow medium through the phantom was fixed to be around 3 cm s^{-1}. The flip angle and the slice thickness were 15° and 4 mm, respectively. The TE and TR were kept minimal according to the given bandwidth values. It is observed from the results that higher bandwidth values do not have specific influence on the phase-contrast maps.
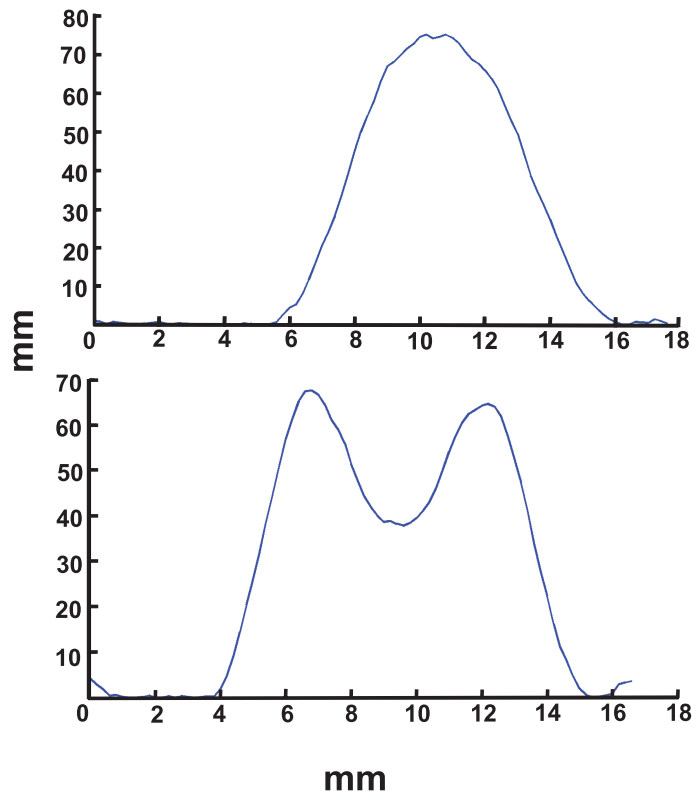
Figure 5.12: Slice profiles for flip angles 10° (top) and 40° (bottom) obtained using stationary phantom.
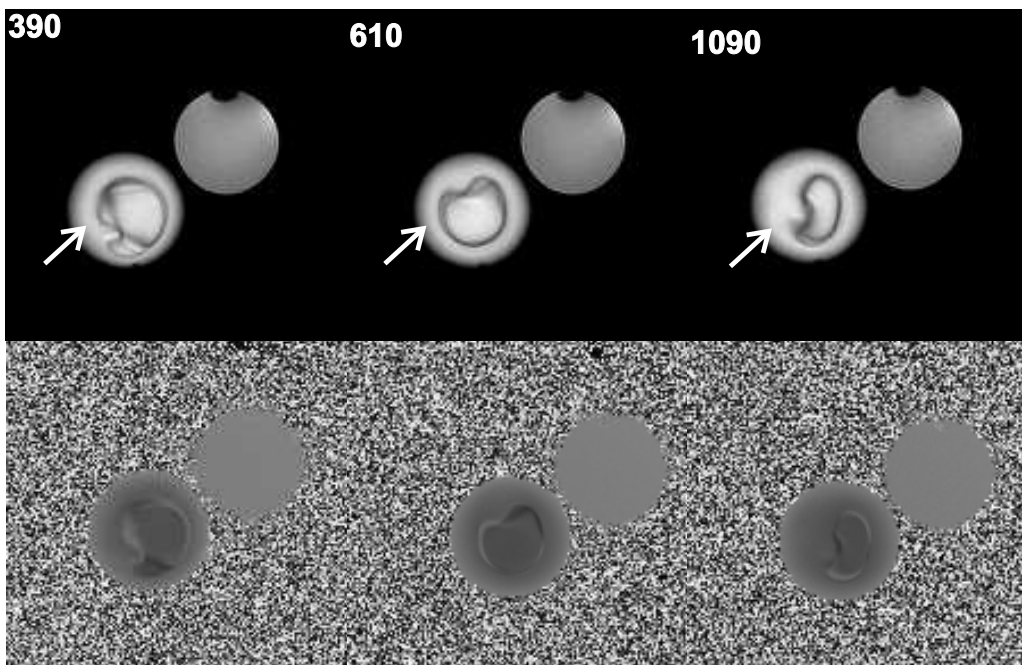

Figure 5.13: Magnitude images and phase-contrast maps of a stationary and flow phantom obtained from PC MRI using varying receiver bandwidths (Hz Pixel^{-1}). The arrows indicate the flow regions.

Velocity Field of View

The velocity field of view (VENC) determines the range of velocities ($\pm$ cm s^{-1}) to be represented by the flow gradients because the phase values in the phase-contrast map are defined between $\pm\pi$. Velocity values beyond the given range create phase wrapping artifacts which lead to misrepresentation of the actual velocities. Higher VENC helps in imaging flow with high velocities without phase wrapping artifacts. However, the sensitivity to low flow reduces substantially with higher VENC values [96, 97]. Figure 5.14 demonstrates the influence of VENC values 10 cm s^{-1} and 30 cm s^{-1} in the laminar phantom with maximum flow velocity adjusted to 16 cm s^{-1}. At VENC of 10 cm s^{-1}, the phase wrapping artifacts due to low VENC are observed. These phase wrapping artifacts are avoided with higher VENC of 30 cm s^{-1}. Phase wrapping artifacts produced in phase-contrast maps can be removed through phase unwrapping methods [98]. However, higher VENCs of more than 30% of the actual imaged velocity, is generally used in the clinical scenario due to the unavailability of robust phase wrapping methods.
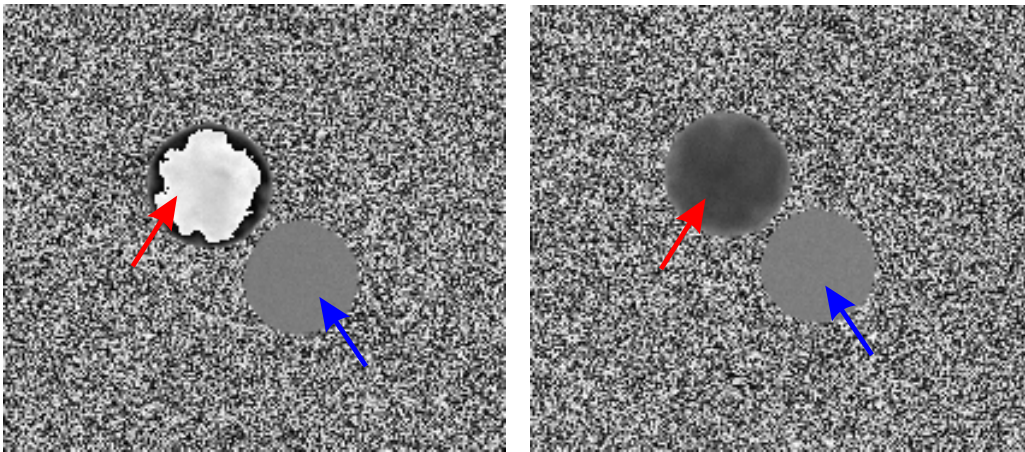

Figure 5.14: The influence of different VENCs on the phase-contrast imaging. Phase-contrast maps of a stationary and flow phantom obtained using single Channel CP head coil with VENC 10 cm s^{-1} (left) and 30 cm s^{-1} (right). The arrows indicate the stationary (blue) and flow (red) regions.

Slice Thickness

The choice of slice thickness in MRI studies depends on the application concerned. For certain anatomical studies, images are generally acquired with slice thicknesses of 8 - 10 mm. In flow studies the choice of slice thickness is of great importance as it can influence the velocity values obtained in every pixel. Influence of intravoxel dephasing and partial volume effects on a given voxel of phase-contrast maps have been discussed extensively in the literature [99, 100]. Intravoxel dephasing is the dispersion of accumulated phase of moving spins due to complex flow. On the other hand, partial volume effect is the loss of signal of different materials located in

the same voxel [34]. Usage of smaller slice thickness is preferable in flow studies as the increase in slice thickness subsequently increases the phase errors in quantitative analysis.

The effect of varying slice thickness were analyzed qualitatively and quantitatively. The flow rate through phantom was kept constant with maximum velocity of flow fixed to be around 3 cm s^{-1} for the experiment. The flip angle was fixed to 5° and TR/TE were kept minimal according to the given slice thickness. Table 5.2 represents the quantitative flow parameters obtained for varying slice thickness. No major deviation in the flow parameters is observed. This may be due to the non-presence of intravoxel dephasing and partial volume effects to flow at constant velocity. However, smaller slice thickness such as 6 mm is preferred in PC MRI under in vivo conditions to obtain accurate flow parameters.

Slice thickness (mm)	Peak Velocity (cm s^{-1})	Average Velocity (cm s^{-1})	Flow Rate (ml s^{-1})	Tube Output (l min^{-1})
5	44	36	69.7	4.19
7	43.1	35.6	68.3	4.10
9	43.6	35.9	69.2	4.11

Table 5.2: Flow parameters obtained for measurements with different slice thickness. The sequence parameters for the experiment: 7 spokes, FOV 256×256, 128×128 matrix, Min-Max flow gradients, Flip angle α 10°, minimum TR/TE. The flow rate of flow pump was set around 4.1 l min^{-1}.

Spatial Resolution

Spatial resolution, similar to slice thickness, is an important sequence parameter dependent on the intended application. High spatial resolution is desirable to increase the qualitative and quantitative information from a region of interest. High spatial resolution reduces partial volumes and intravoxel dephasing effects under flow conditions. But increase in spatial resolution proportionally increases TE and total acquisition time. Choice of spatial resolution for flow studies must balance achievable acquisition time along with reduction of flow-induced artifacts. Flow parameters obtained with three spatial resolutions such as 1.5 mm, 1.8 mm, 2 mm, as shown in Table 5.3, were found to be consistent. For clinical applications under in vivo conditions it is preferable to have spatial resolution below $2 \times 2 \times 6$ mm^3 which provides an optimal balance between spatial resolution and TE.

Number of Spokes / Radial Views

The number of spokes used for an image has a direct influence on the quality of the image. It is observed from previous results that NLINV reconstructions can produce qualitative images

Spatial Resolution (mm)	Peak Velocity (cm s^{-1})	Average Velocity (cm s^{-1})	Flow Rate (ml s^{-1})	Tube Output (l min^{-1})
$1.5 \times 1.5 \times 6$	44.1	36	71.1	4.29
$1.8 \times 1.8 \times 6$	43.9	36	69.3	4.16
$2.0 \times 2.0 \times 6$	42.9	35.5	68.5	4.13

Table 5.3: Flow parameters obtained for measurements with different base resolution. The sequence parameters for the experiment: 7 spokes, FOV 256×256, Min-Max flow gradients, minimum TR/TE. The flow rate of flow pump was set around 4.1 l min^{-1}.

from highly undersampled data. However, the stability of NLINV reconstruction for real-time PC MRI to undersampling has to be quantitatively analyzed before in vivo trials. Since undersampling depends on the number of spokes used, quantitative analysis was performed on phase-contrast maps obtained from different number of spokes. The results of flow parameters as shown in Table 5.4 are consistent with actual flow rate in the tube. The stability of NLINV reconstruction even with highly undersampled data of 7 spokes is observed. It turned out that undersampling beyond 7 spokes might strain NLINV reconstruction process and lead to the generation of artifacts. Therefore, 7 spokes was used for measurements under in vivo conditions.

Number of Spokes	Peak Velocity (cm s^{-1})	Average Velocity (cm s^{-1})	Flow Rate (ml s^{-1})	Tube Output (l min^{-1})
7	43.9	36	69.3	4.19
11	43.7	35.4	68.6	4.12
25	44	35.5	70.1	4.23

Table 5.4: Flow parameters obtained for measurements with different number of spokes. The sequence parameters for the experiment: FOV 256×256, 128×128 matrix, slice thickness 6 mm, VENC 150 cm s^{-1}, Min-Max flow gradients, TR/TE/α = 3.43/2.75 ms/10°. The flow rate of flow pump was set around 4.1 l min^{-1}.

5.1.7 Sequence Optimization

In the previous sections, the bipolar flow gradients were used separately for any other gradients (independent mode) to understand its influence on basic sequence parameters. As the major portion of TE for phase-contrast pulse sequence is used by flow-encoding gradients, any reduction in TE will lead to the decrease in total acquisition time thereby increasing the temporal resolution. Further, shorter TE would decrease the negative effects of turbulent flow which lead to dephasing of different velocities in a single voxel [36, 101, 102]. To achieve reduction of TE, the flow gradients in z direction can be overlapped with slice selection and slice rephasing gradient while maintaining the overall zero gradient magnetic moment. Figure 5.15 displays the

overlapped radial FLASH PC MRI pulse sequence. The method used for minimizing TE using overlapping flow encoding gradients was adopted in this thesis from Bernstein et al. [17,103].
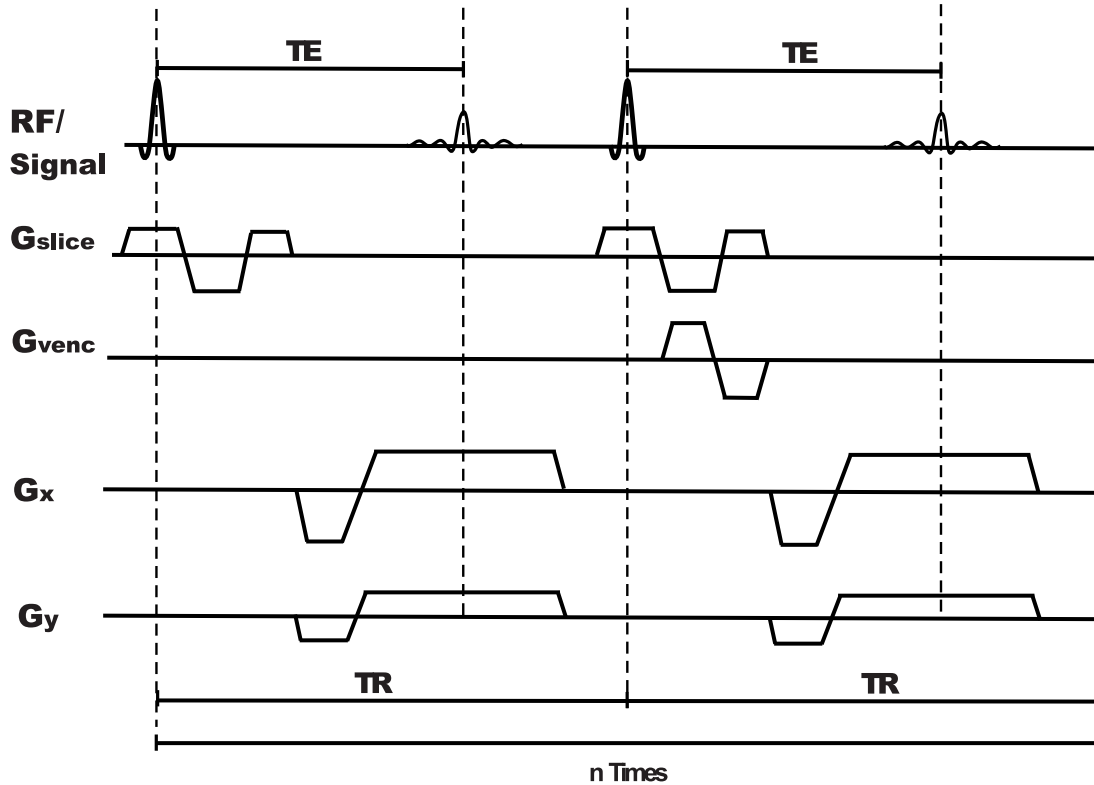

Figure 5.15: Schematic representation of radial FLASH pulse sequence with flow gradients in G_{venc} which is overlapped with the motion-compensated slice selection gradient.

Phase difference maps from images can be obtained by applying bipolar flow gradients in two gradient modes such as Max-Zero and Min-Max. These two flow gradient forms are overlapped with slice rephasing gradients as shown in Figure 5.16. From the Figure 5.16, it is seen that for the Min-Max version the overlapped gradients are being played out on both flow encoding images whereas for the Zero-Max version the overlapped gradient is being played only for the Max condition.

The reference image obtained from Zero or Min condition might be influenced by motion artifacts or uncompensated moving spins which can induce potential phase errors. These errors are avoided by introducing motion-compensated gradients in the G_z direction [104] which are further overlapped with the slice selection and slice rephasing gradient. Motion compensation gradient represented in Figure 5.17 is introduced in the zero condition.
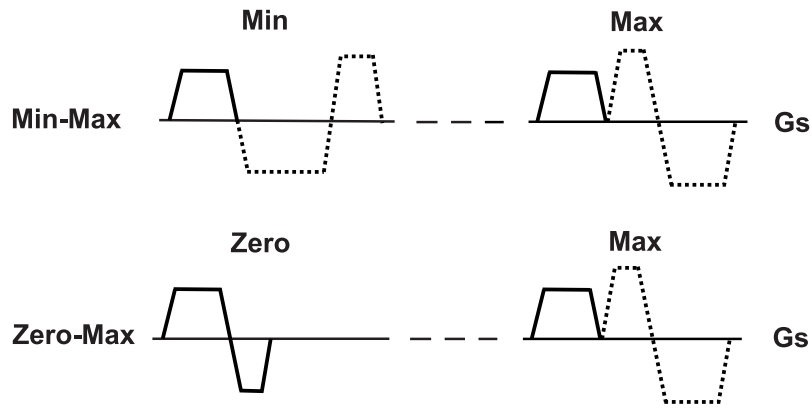
Figure 5.16: Schematic representation of overlapping of Min-Max and Max-Zero flow gradients (dashed) with slice rephasing gradient.
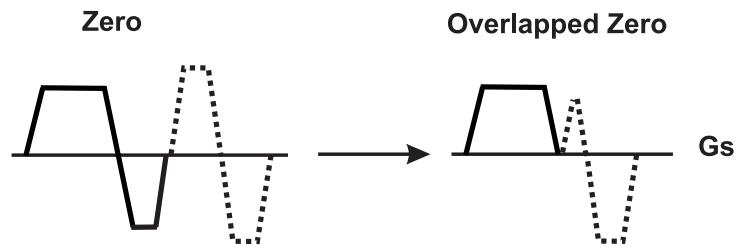

Figure 5.17: Schematic representation of overlapping motion-compensation gradient (dashed) with slice rephasing gradient.

Independent vs Overlapping Flow Gradients

The pulse sequences with independent and overlapped flow gradients are validated for a definite value of flow rate and volume on the flow phantom. The flow gradient modes such as Min-Max and Zero-Max were combined with the slice selection gradient to obtain overlapped gradients. The spatial resolution was set to $1 \times 1 \times 6$ mm^3 and the temporal resolution for each phase difference image was fixed to 2 seconds with number of spokes per image being 255, 235 for Max-Zero and Max-Min mode with overlapping flow gradients, respectively. The minimal TR/TE for Min-Max and Zero-Max mode of overlapping gradient format were 4.25/3.28 ms and 3.92/2.91 ms respectively and for independent gradient format 4.25/3.33 ms and 4.65/3.72 ms respectively. The flow rate was set to constant flow of around 4.5 l min^{-1}. The results obtained from the two tubes of the flow phantom are displayed in Table 5.5 for large and small tubes. They are consistent with the values obtained from the flow meter. These results suggest that overlapping of gradients do not have negative influence on the obtained flow parameters. Also the overlapping Max-Zero gradient mode provides additional reduction of TE when compared to Min-Max.

Sequence	Large Tube (1 min^{-1})	Small Tube (1 min^{-1})
Overlap:Max-Zero	4.5	4.4
Overlap:Max-Min	4.5	4.4
Independent:Max-Zero	4.5	4.6
Independent:Max-Min	4.5	4.4

Table 5.5: Flow rate obtained from large and small tubes using independent and overlap flow gradient sequence

.

Overlapping Readout Gradients

In the previous section, the overlapping of bipolar flow gradients and slice rephasing gradients to reduce TE was discussed. The flow encoding gradient was overlapped with slice selection gradient but was kept independent with respect to other gradients. Further shortening of TE is possible by overlapping the read dephasing gradient with the overlapped flow gradients as shown in Figure 5.18.
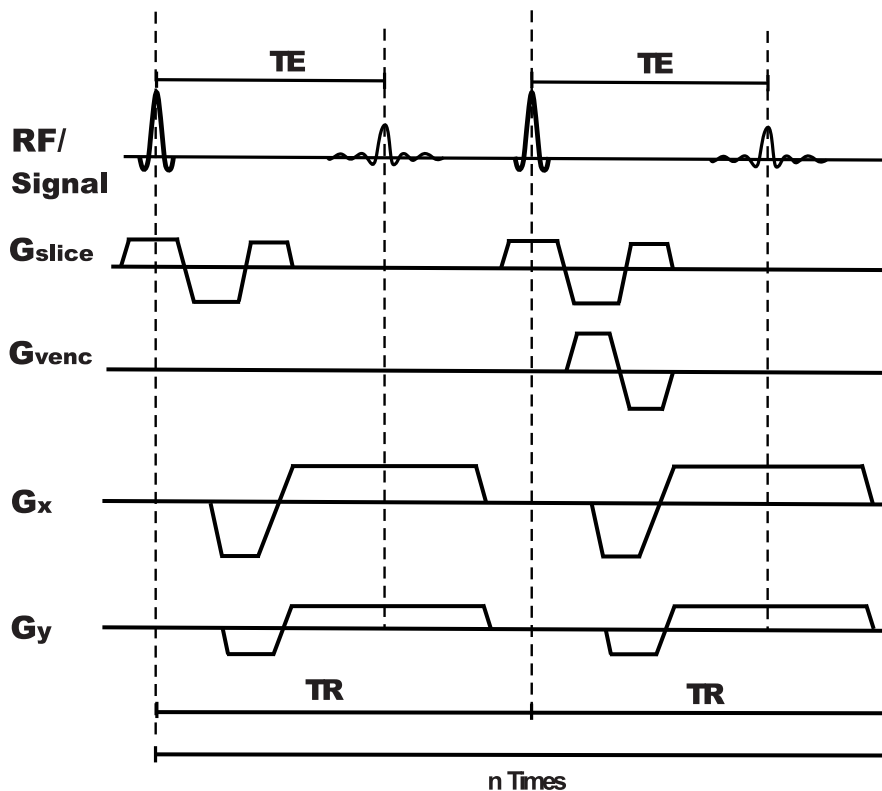

Figure 5.18: Schematic representation of radial PC MRI sequence where flow gradients represented in G$_{venc}$ is overlapped with slice rephasing and read dephasing gradient.

Experiments were performed on the flow phantom to understand the influence of overlapping

Sequence	Peak Velocity (cm s^{-1})	Average Velocity (cm s^{-1})	Flow Rate (ml s^{-1})	Tube Output (l min^{-1})
Read Dephasing Overlap	43.2	35.6	69.6	4.19

Table 5.6: Flow parameters obtained for measurements on phantom with overlapped flow gradients. The sequence parameters for the experiment: 7 spokes, FOV 256×256, 144×144 matrix, TR/TE/α = 3.05/2.29 ms/10°, Min-Max flow gradients. The flow rate of flow pump was set around 4.1 l min^{-1}.

readout gradients on the flow parameters. Table (5.6) shows the flow parameters obtained from the overlapping gradients. The flow parameters obtained were consistent with flow rate obtained from flow meter. Therefore the pulse sequence consisting of overlapped flow and read gradients was further used for in vivo studies as it enables a further reduction of TE.

5.1.8 Evaluation of Sequence Design

The basics of phase-contrast MRI were discussed in the previous sections. Essential factors such as encoding schemes and reconstruction techniques were compared for achieving real-time PC MRI. In addition, the evaluation of the sequence parameters and optimization of sequence was also performed to maintain high spatial and temporal resolution. However, the optimized pulse sequence has to be evaluated for factors which are specific to phase-contrast imaging. This section discusses the evaluation of optimized real-time PC MRI method for flow studies.

Phase Offset Error

Pixels in phase-contrast maps have to be integrated for a region of interest to obtain valuable physiological information. Each pixel in the phase-contrast map directly correlates with the velocity of the moving spins. This suggests that regions of stationary spins should ideally represent zero phase or zero velocity [105]. However, due to system imperfections, eddy current effects are produced [106–108] which induce inaccuracies to the sensitivity of the phase. These inaccuracies can be observed in the phase difference image where the stationary spins have minimal phase offsets. Many methods and techniques have been proposed to avoid or to correct the phase offset error [17, 109–115]. One of the most commonly used techniques to correct the phase error is to image a stationary phantom after the volunteer study and to subtract the phase offset obtained for the same ROI from the volunteer data. Although this method is commonly used, the approach to subtract phase offset based on different measurements consisting of volunteer and phantom is questionable. Phase offset errors have to be kept at minimal levels since the existing techniques do not provide optimal phase offset correction. Phase offset error below 5% is considered as an acceptable value for measurements [116]. The phase offset error produced in phase-contrast maps for the Max-Min and Zero-Max flow gradient modes were

compared. A region of interest representing stationary spins and similar in size to the region of flowing medium is taken for comparison of flow rates.
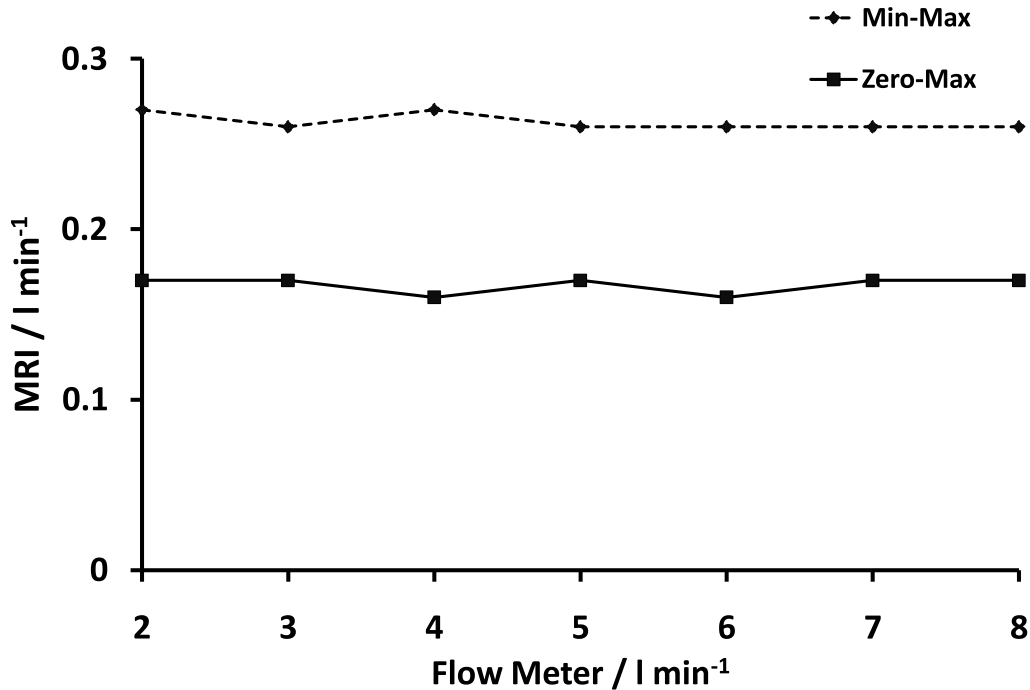

Figure 5.19: Phase offset error comparison between Min-Max and Zero-Max flow gradients for different flow rates. The sequence parameters for the experiment: 7 spokes, spatial resolution $1.3 \times 1.3 \times 6$ mm^3. TR/TE/α = 3.21/2.32 ms/10° and 2.86/1.93 ms/10° for Min-Max and Zero-Max flow gradient modes, respectively.

As observed in the Figure 5.19 the flow rates representing the phase offset obtained were fairly consistent for different flow meter values. The phase offsets observed on the graphs corresponded to about 0.17 l min^{-1} for the Zero-Max and 0.27 l min^{-1} for the Min-Max version. Phase offset errors observed is very low for Zero-Max version compared to normal cardiac output of 5-6 l min^{-1} observed in the heart.

Flow Gradient Mode: Min-Max vs Zero-Max

The presence of two flow gradient modes of Min-Max and Zero-Max has been discussed in detail in the previous sections. Due to the overlapping of velocity-encoding flow gradient and other gradients, shorter TE has been achieved by both flow gradient modes. Moreover, Zero-Max version provides further reduced TE as compared to Min-Max version with lower phase offset values during in vitro studies. Although Zero-Max version would be preferred for real-time PC MRI studies due to its shorter TE, both flow gradient modes were validated prior to in vivo studies. Calibration for different flow rates were performed between Min-Max and Zero-Max

flow gradient methods. Results shown in Figure 5.20 were obtained for 10 simulated ECG heart cycles. It is observed that both versions provide flow rates similar from those obtained from flow meter.
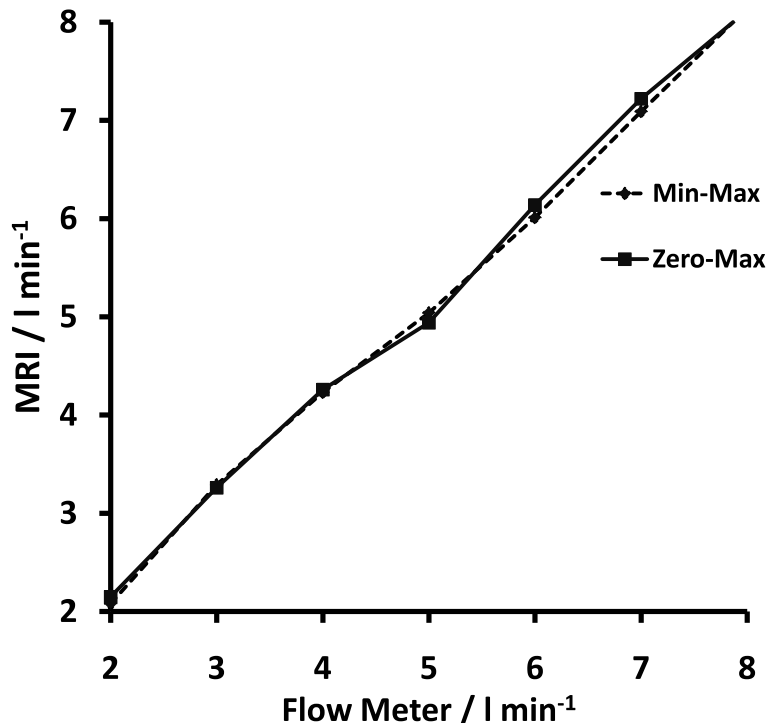

Figure 5.20: Calibration of phantom with different flow rates for Max-Zero and Min-Max flow gradient mode. The sequence parameters for the experiment: 7 spokes, FOV 192×192, 144×144 matrix, VENC 150 cm s^{-1}. TR/TE/α for Min-Max and Zero-Max were 3.21/2.32 ms/10° and 2.86/1.93 ms/10°, respectively.

Influence of Motion-Compensation Gradients

The introduction of motion-compensation gradients in the slice direction and its influence on the flow parameters were discussed in the previous sections. Additional motion-compensation gradients can also be introduced in other physical gradient axis directions. It is assumed that such introduction of flow-compensation gradients might aid in removing additional dephasing of spins in the read directions (G_x, G_y). However, such influence of motion-compensation gradients in the read directions have to be qualitatively and quantitatively analyzed. The readout motion-compensation gradient was overlapped with other gradients to achieve minimum TE. The pulse sequence design with overlapped slice and readout motion-compensation gradients is shown in Figure 5.21.

The quantitative analysis, with and without motion-compensation gradient in the read direction, was performed on the flow phantom and the flow parameters are displayed in Table 5.7.
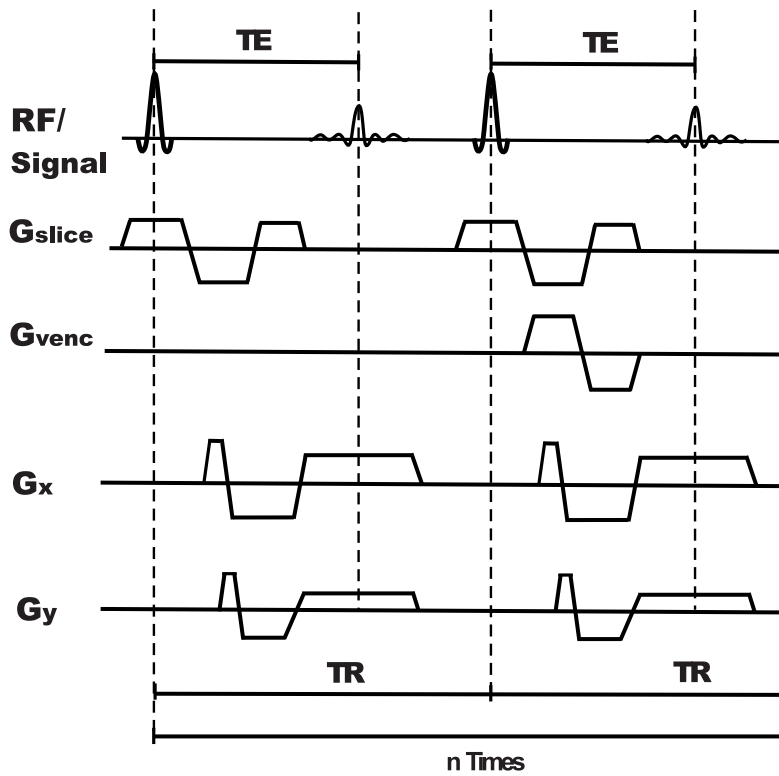
Figure 5.21: Schematic representation of radial FLASH PC MRI sequence with flow gradients in G_{venc} and motion compensation gradients in the read direction.

The flow parameters obtained in the read direction with and without motion-compensation gradient are similar in nature as there is minimal or no influence of moving spins in the read direction.

Experiments were performed under in vivo conditions to evaluate the presence of motion-compensation gradients. Figure 5.22 depicts the magnitude and phase-contrast maps obtained from with and without motion-compensation gradients in the read direction. Table 5.8 represents quantitative analysis performed in the region of ascending aorta obtained through real-

Sequence	Peak Velocity (cm s^{-1})	Average Velocity (cm s^{-1})	Flow Rate (ml s^{-1})	Tube Output (l min^{-1})
Without Flow Compensation	43.2	35.6	69.6	4.19
With Flow Compensation	44.5	36.7	70.6	4.24

Table 5.7: Flow parameters obtained for measurements on phantom with overlapped flow gradients. The sequence parameters for the experiment: 7 spokes, spatial resolution such as $1.8 \times 1.8 \times 6$ mm^3 with TR/TE/α = 3.05/2.29 ms/10° and 3.15/2.39 ms/10° for without and with motion compensation in read direction, respectively. The flow rate of flow pump was set around 4.1 l min^{-1}

56

time PC MRI. It is observed that most of the flow parameters are similar between real-time PC MRI with and without motion-compensation gradients in read direction. However, lower values of peak and average velocities are observed for the acquisition performed with motion-compensation gradients in the read direction due to the associated longer TE. Employing shorter TE is encouraged for flow studies as it reduces potential effects induced by turbulence. Therefore in order to obtain minimum TE, in vivo studies used motion-compensation gradients in slice direction were only used for in vivo studies.
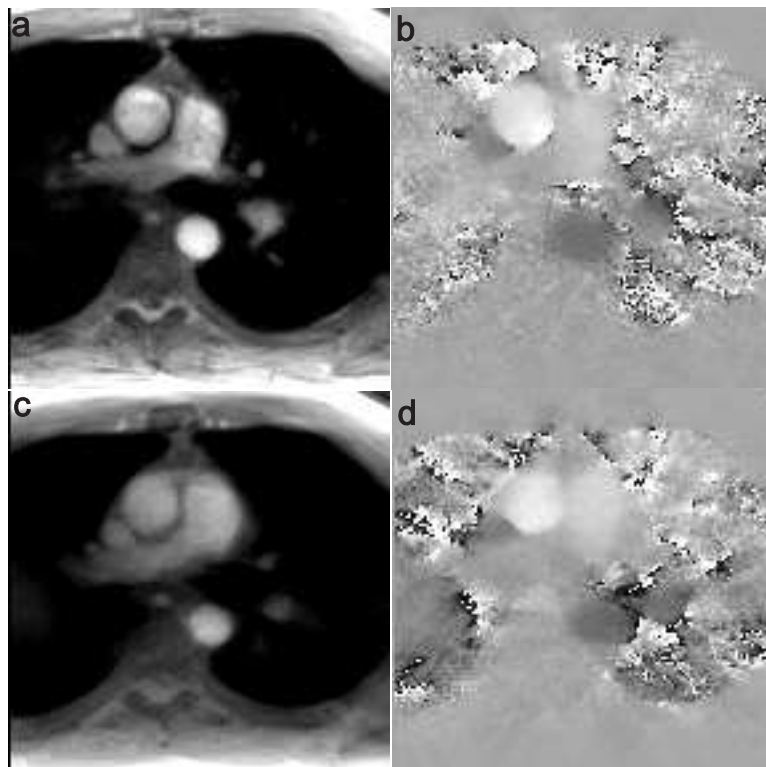

Figure 5.22: Transverse view of the human heart at the region of ascending aorta: Magnitude images (a, c) and phase-contrast maps (b, d) during peak systole phase of the cardiac cycle obtained with motion-compensated slice gradients (a, b) and motion-compensation slice and read gradients (c, d) using real-time PC MRI.

Interleaved vs Sequential Flow Encoding

The phase difference operation for PC MRI is performed on two images with different flow-encoding gradients. Every radial phase image is obtained from a particular order of spokes determined by the reordering scheme. Two variants of acquiring k-space with and without flow-encoding gradients called sequential and interleaved flow encoding were developed in this thesis. In interleaved version, the radial spokes are acquired with and without flow-encoding gradients alternatively, whereas radial spokes are acquired one after another in a sequential order to form complete images before the phase difference operation [117]. The total acquisition

Flow Parameters	Slice	Slice + Read
Heart Rate (Beats min^1)	64.6 ± 10.3	64.8 ± 6.9
Peak Velocity (cm s^1)	140.9 ± 15.9	93.8 ± 8.3
Max. Peak Average Velocity (cm s^1)	81.5 ± 5.9	68.1 ± 2.9
Average Velocity (cm s^1)	20.3 ± 3.7	18.4 ± 0.8
Flow Rate (ml s^1)	140.9 ± 15.9	136.9 ± 6.7
Stroke Volume (ml)	132.9 ± 12.5	132.6 ± 7
Volume (l min^1)	8.3 ± 0.8	8.2 ± 0.4

Table 5.8: Values given as mean $\pm$ standard deviation (SD) represent the flow parameters obtained using real-time PC MRI for a subject across 15 heartbeats under free breathing condition. The acquisition was performed with slice and with (slice+read) motion-compensation gradients. The scan parameters were 7 spokes, spatial resolution $1.3 \times 1.3 \times 6$ mm^3 with TR/TE/α = 2.86/1.93 ms/10° and 3.77/ 2.88 ms/10° without and with motion-compensation, respectively.

Reordering Scheme	Large Tube (l min^{-1})	Small Tube (l min^{-1})
Sequential	3.8	3.7
Interleaved	3.5	3.8

Table 5.9: Flow parameters obtained for the flow phantom for different reordering schemes. The sequence parameters for the experiment: 255 spokes, VENC 150 cm s^{-1}, spatial resolution $1 \times 1 \times 8$ mm^3. TR/TE/α = 3.92/2.96 ms/8° with temporal resolution of 2 seconds per phase difference image. The flow rate of the pump was fixed to 3.5 l min^{-1} approximately.

time and temporal resolution per phase-contrast map remains constant for the two variants of flow encoding as represented schematically in Figure 5.23. In vitro studies were performed on the flow phantom which are shown Table 5.9. The volume rate as obtained from studies on the flow phantom do not show any major deviations from the flow meters values.

The flow-encoding schemes were further analyzed under in vivo conditions. The magnitude and phase-contrast maps obtained for different encoding schemes during the peak systole and diastole phase of the heart cycle are shown in Figure 5.24. The magnitude and phase-contrast maps of different encoding schemes do not show any significant differences. As there are no significant differences observed qualitatively, the two encoding schemes of real-time PC MRI were used for in vivo studies.

5.1.9 Parameters Influencing NLINV Reconstruction

The implementation of NLINV has been discussed in great detail in the chapter 4. NLINV, as an iterative reconstruction technique, consists of regularization terms for estimating the image and coil sensitivities. The choice of the regularization terms is dependent on factors such as
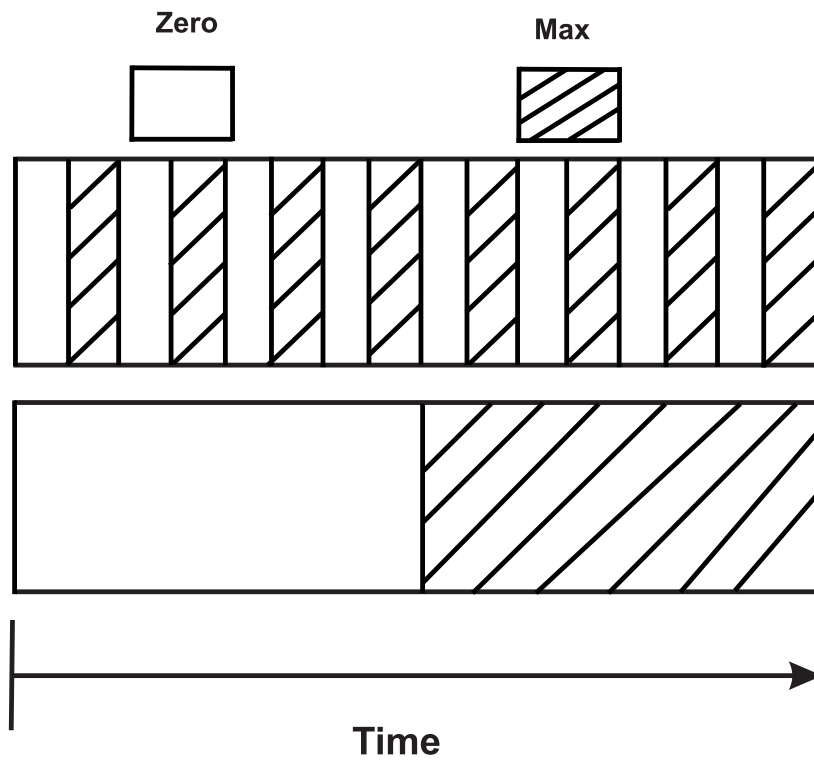
Figure 5.23: Schematic representation of sequential and interleaved acquisition schemes for the Zero-Max flow-encoding gradient mode.
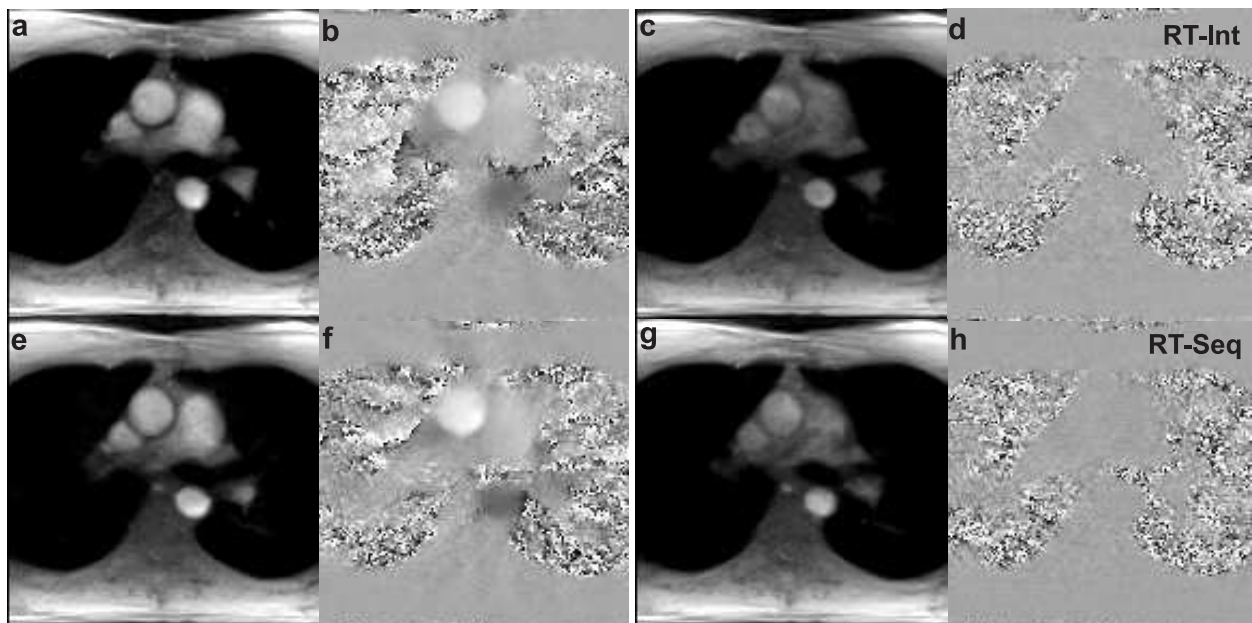

Figure 5.24: Transverse view of the human heart at the region of ascending aorta: magnitude images (a, c, e, g) and phase-contrast maps (b, d, f, h) during peak systole (a, b, e, f) and diastole (c, d, g, h) phase of the cardiac cycle obtained for sequential (RT-Seq) and interleaved (RT-Int) acquisition schemes of the real-time PC MRI.

region of interest, information pursued and the application concerned. This section focuses on the evaluation of the factors that determine the NLINV reconstruction technique.

Coil Sensitivity Smoothing Function

The iterative reconstruction process in NLINV, involves regularization terms for image content and coil sensitivities. The regularization term for the coil sensitivities strongly penalizes the high spatial frequencies in the coil sensitivities [76]. Improper regularization of the coil sensitivities lead to the formation of artifacts especially with respect to high spatial frequencies produced. These artifacts are avoided by the presence of coil sensitivity smoothing function during the iterative process. The coil sensitivity smoothing function is a weighted discrete Fourier transform multiplied with the coil sensitivity profile, which causes a Fourier weighting of the form $(1 + W_c|k|^2)^{16}$ where W_c is the coil smoothing factor. There are three variants of the coil smoothing factor such as 220, 440, 880 which is commonly used for real-time radial FLASH imaging. The coil smoothing factor has to be analyzed with respect to real-time PC MRI. Figure 5.25 represents the NLINV reconstructed images obtained with different smoothing factors from the real-time PC MRI. It is observed that the images of the variants 220 and 440 are corrupted with artifacts especially in the region of the lungs where no signal is present. However, coil smoothing factor 880 strongly removes the artifacts and produces clear magnitude image and phase-contrast maps. Higher factor of coil smoothing function of greater than 880 can have a negative influence in filtering important image content. Therefore coil smoothing factor 880 is used for obtaining coil smoothing function for real-time PC MRI.

Newton Steps

Number of iterations or Newton steps used in the iterative process determines the outcome of the images. High number of Newton steps can induce noise in the images, whereas low numbers can lead to blurring. Further the computation time for the entire reconstruction procedure increases proportionally to the number of Newtons steps used. For real-time PC MRI, clear delineation of the blood vessels or the region of interest is desired which aids in better quantitative analysis. The number of Newton steps for the NLINV reconstruction process was analyzed as shown in Figure 5.26. It was observed that images obtained from NLINV reconstruction with 8, 9 and 10 Newton steps produces increased noise. In contrast, images with 6 Newton steps were found to be blurred. In order to support clear delineation of the vessel structures and the better segmentation for the quantitative analysis software, 7 Newton steps were chosen as standard parameter for the NLINV reconstruction procedure.
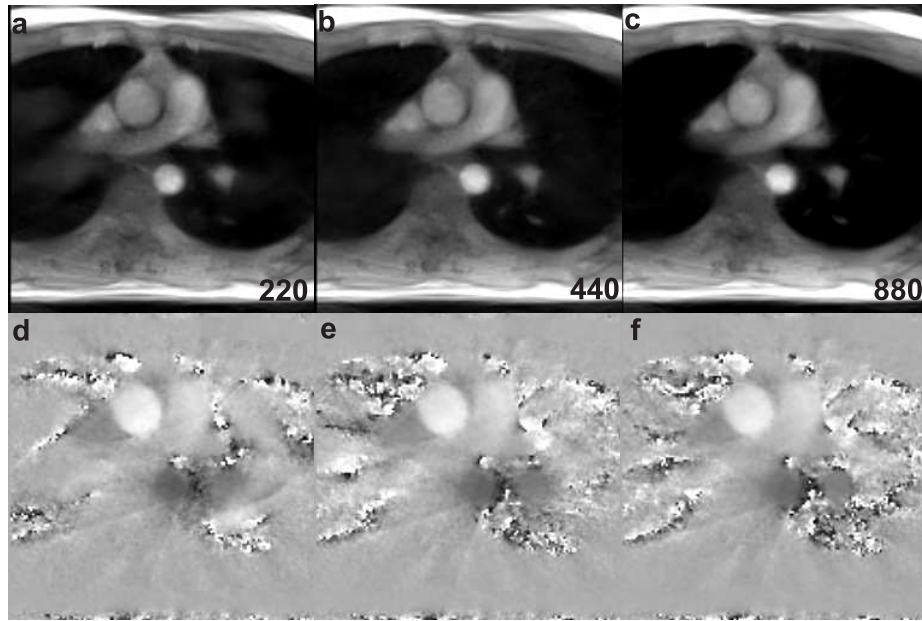
Figure 5.25: Transverse view of the human heart at the region of ascending aorta: magnitude images (a, b, c) and phase-contrast maps (d, e, f) obtained from NLINV reconstruction for different coil sensitivity smoothing factors (220, 440, 880). The sequence parameters for the experiment: 7 spokes, spatial resolution $1.3 \times 1.3 \times 6$ mm^3 with TR/TE/$\alpha = 2.86/1.93$ ms/10°.
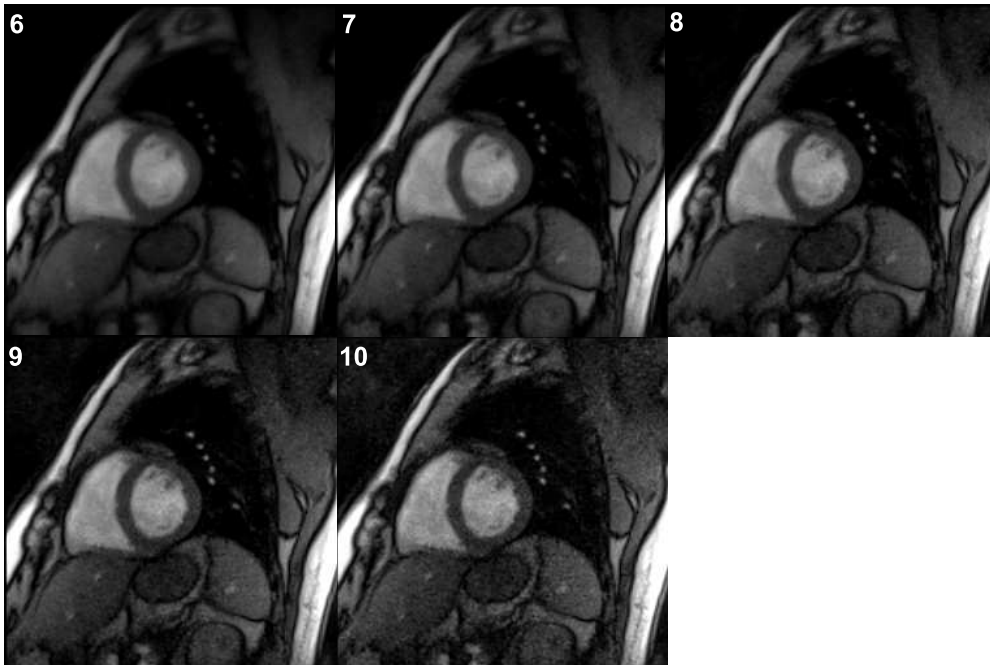

Figure 5.26: Short axis view of the human heart: magnitude images obtained from NLINV reconstruction using radial FLASH pulse sequence for different number of Newton steps or iterations (6, 7, 8, 9, 10). The sequence parameters for the experiment: 7 spokes, spatial resolution $1.5 \times 1.5 \times 8$ mm^3 with TR/TE/$\alpha = 2.23/1.46$ ms/8°.

Dampening Factor

The temporal regularization, as explained in chapter 4, mainly involves the usage of the previous frame as an initial estimate to the regularized NLINV reconstruction process. Prior to the temporal regularization, the previous frame is multiplied with a dampening factor which adjusts the degree of temporal regularization. The dampening factor consists of values between 0 and 1. Similar to Newton steps, the choice of the dampening factor influences the qualitative information of the reconstructed images. The dampening factor, for real-time imaging, is chosen with respect to the application and the anatomical structure imaged. Experiments were performed to analyze the influence of dampening factors (0.9, 0.7, 0.5, 0.3) on the magnitude images using real-time radial FLASH [76] and NLINV reconstructions as shown in Figure 5.27. Moreover, the NLINV reconstructions were performed with 7 iterations or Newton steps. It was observed that the decrease in dampening factor led to an proportionate increase in the blurring of images. The anatomical images reconstructed with the dampening factor 0.7 was found to be the best compromise for flow studies as it preserves the sharpness of the vessel structures. Therefore dampening factor of 0.7 and Newton Steps of 7 were used for in vivo real-time PC MRI studies.
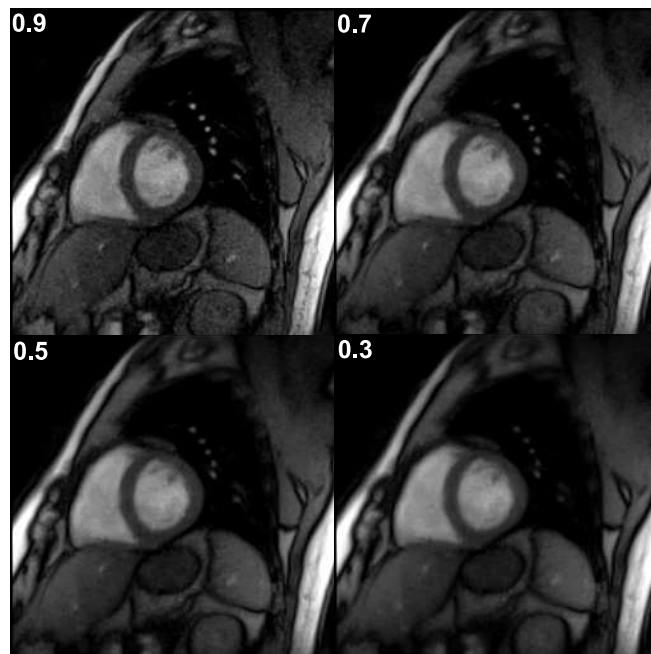

Figure 5.27: Short axis view of the human heart: magnitude images obtained from NLINV reconstruction using radial FLASH pulse sequence for different dampening factors (0.9, 0.7, 0.5, 0.3). Images were reconstructed with 7 Newton steps. The sequence parameters for the experiment: 7 spokes, spatial resolution $1.5 \times 1.5 \times 8$ mm^3 with TR/TE/α = 2.23/1.46 ms/8°.

Scan Parameters	Real-time Methods
TR	2.86 ms
TE	1.93 ms
α	10°
Slice Thickness (mm)	6
Radial Spokes	7
VENC (cm s^{-1})	200
FOV (mm)	192
FOV read (%)	100
Base Resolution	144
In-plane Resolution	1.3 mm
Temporal Resolution	40 ms
Newton Steps	7
Dampening Factor	0.7
Coil Smoothing Function	880
Flow Gradient Mode	Zero-Max
Flow Encoding Mode	Interleaved/Sequential

Table 5.10: Scan and reconstruction parameters for in vivo studies using real-time PC MRI.

5.1.10   Summary

The development of a realiable and robust real-time PC MRI was the primary aim of this thesis. The tedious process of development aims on different aspects such as pulse sequence development, acquisition schemes and the reconstruction. This section mainly focused on sequence implementation and optimization that are critical for achieving real-time PC MRI. The Cartesian and radial encoding schemes were compared through in vitro studies and the latter was preferred for achieving real-time PC MRI. NLINV reconstruction, which works with highly undersampled data, was adapted to phase-contrast imaging thereby providing high temporal resolution for real-time imaging. Temporal median filter which helps in reducing the streaking artifacts from magnitude images, was not used in the phase-contrast maps [118]. The pulse sequence was optimized for real-time PC MRI and the Zero-Max version along with overlapping gradients was preferred due to shorter TE and minimal phase offset errors. Flow compensation gradients were used only in the slice direction as introducing these gradients in the read directions increases the TE. Further parameters influencing the pulse sequence and NLINV reconstruction process were analyzed and fixed for real-time flow studies as shown in the Table 5.10. Figure 5.28 displays the magnitude image and phase-contrast map obtained from the real-time PC MRI using the defined sequence and reconstruction parameters.
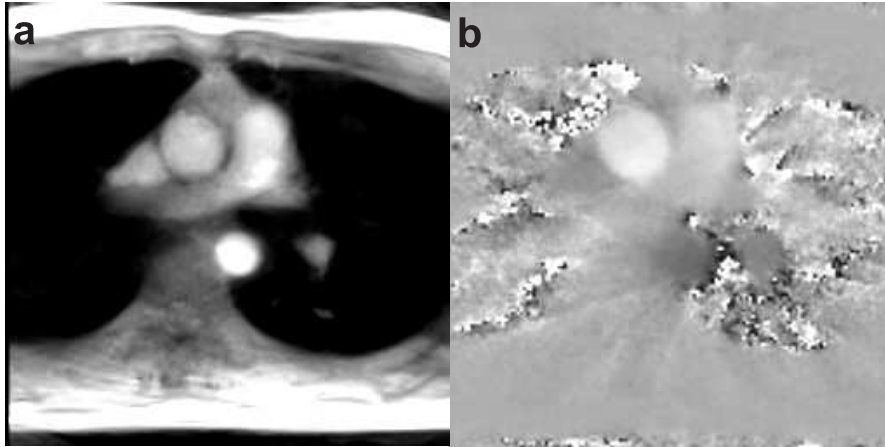
Figure 5.28: Transverse view of the human heart at the region of ascending aorta: magnitude image (a) and phase-contrast map (b) obtained from real-time PC MRI method. The sequence parameters for the experiment: 7 spokes, spatial resolution $1.3 \times 1.3 \times 6$ mm^3 with TR/TE/α = 2.86/1.93 ms/10°.

5.2   Validation

The developed method has to be compared with a standard method such as cine phase-contrast MRI to validate its applicability in the clinical environment. Real-time PC MRI being a quantitative method, has to be quantitatively analyzed for flow parameters under in vivo conditions. This section presents the quantitative analysis performed under in vivo conditions using real-time PC MRI. For better understanding, an overview of the anatomy of the human heart is presented along with the description of the desired region of interest for quantitative cardiovascular studies.

5.2.1   Human Heart

The heart is one of most important organs of the human body. The primary function of the human heart is to pump the deoxygenated blood to the lungs and oxygenated blood to the rest of the body. Blood vessels that are connected directly to the heart are larger in diameter (approximately 3 cm) in comparison to peripheral blood vessels. The human heart consists of four chambers comprising the right and left atrium and ventricles. The atrium collects the blood coming from other regions of the body. Ventricles on the other hand are responsible for transportation of blood to other regions of the body. The passage between the right atrium to right ventricle is guarded by tricuspid valve and left atrium to left ventricle by bicuspid or mitral valve. The right atrium is connected to superior and inferior vena cava which brings the deoxygenated blood from the whole body to the right atrium. The deoxygenated blood is pumped from the right ventricle to the lungs through pulmonary artery. The pulmonary artery is divided into right and left pulmonary artery which transports the deoxygenated blood to

64

the respective lung regions. The oxygenated blood from the lungs is brought back to the left atrium by pulmonary veins which is then transported to the rest of the body through the aorta.
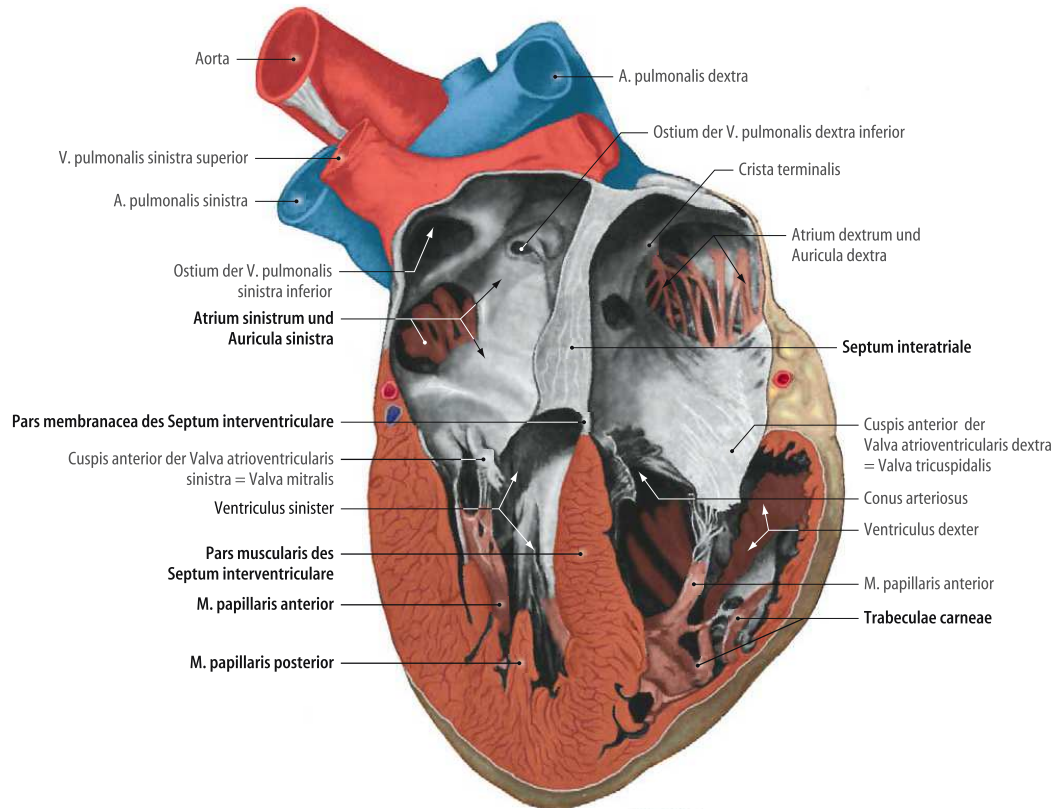
Aorta

A. pulmonalis dextra

Ostium der V. pulmonalis dextra inferior

V. pulmonalis sinistra superior

Crista terminalis

A. pulmonalis sinistra

Atrium dextrum und
Auricula dextra

Ostium der V. pulmonalis
sinistra inferior

**Atrium sinistrum und
Auricula sinistra**

Septum interatriale

Pars membranacea des Septum interventriculare

Cuspis anterior der
Valva atrioventricularis dextra
= Valva tricuspidalis

Cuspis anterior der Valva atrioventricularis
sinistra = Valva mitralis

Conus arteriosus

Ventriculus sinister

Ventriculus dexter

**Pars muscularis des
Septum interventriculare**

M. papillaris anterior

M. papillaris anterior

Trabeculae carneae

M. papillaris posterior

Figure 5.29: Schematic representation of the human heart along with its chambers and blood vessels as represented in "Altlas der Anatomie des Menschen" [119].

The individual regions of the heart function periodically to maintain constant flow of blood to the other regions of the body. This periodic property of the heart can be verified by electrical signals produced during the functioning of heart. These recorded electrical signals are called as electro-cardio graphs (ECG). Since the ECG signals are periodic in nature the heart rate (beats min^{-1}) is calculated from time between the peak of two ECG signals (R-R interval). The cardiac phase can be divided into systole and diastole referring respectively to the contraction and relaxation phases of the heart. During systole the blood is pushed away from the ventricles to the blood vessels, whereas during diastole the heart muscles relax and the blood flows into the ventricles from the atrium. The systolic phase of the heart measures around 200 ms and is time invariant even at different heart rates [120]. Taking into consideration the systolic upstroke waveform, acquiring phase difference images with temporal resolution lesser than 50 ms are required to perform quantitative analysis.

Physiological Parameters

Physiological parameters are diagnostic indicators of health which are used by the clinicians as reference for determining diseases. The physiological parameters[1] used by physicians for the analysis of cardiac flow are as follows.

Peak Velocity (cm s^{-1}): The maximum velocity of flow for a particular region of interest. The values obtained are dependent on the slice position and region of interest. The peak velocity of ascending aorta is normally around 100-120 cm s^{-1}.

Average Velocity (cm s^{-1}): It is the spatial average of pixels over the lumen of a vessel in a phase-contrast map. It is also considered as an important parameter for calculation of flow rate. The average velocity obtained in the ascending aorta is around 60-80 cm s^{-1}.

Flow Rate (ml s^{-1}): It is *Average Velocity$\times$ Area* which represents the rate of flow per phase-contrast map. The flow rate (ml s^{-1}) can be calculated by multiplying average velocity and area of region of interest (ROI). The flow rate obtained in the aorta is around 80-100 (ml s^{-1}).

Stroke Volume (ml beat^{-1}): It is a quantity representing the volume of blood leaving the ventricles per heart beat. It is used as an important diagnostic parameter to understand the volume fluctuation over different heart cycles. The normal range measured in the aorta is 60-100 ml beat^{-1}. From the phase-contrast maps, stroke volume is calculated by integrating the flow rates obtained from the images of a single heartbeat.

Cardiac Output (l min^{-1}): It is the volume of blood that flows out of ascending aorta in a minute. Cardiac Output is dependent on many factors such as flow rate and heart rate variations. It is normally expected to be between 5-8 l min^{-1}.

5.2.2 Real-time PC MRI of Cardiovascular Blood Flow

Performing cardiovascular studies for qualitative and quantitative diagnostic information requires specific imaging planes. The imaging planes are generally chosen according to the region of interest and the targeted information. For cardiovascular flow studies using PC MRI, axial or transverse view at the region of aorta is preferred as it provides quantitative information of through-plane flow in major blood vessels such as ascending aorta, descending aorta, pulmonary artery and superior vena cava.

---

[1]www.edwards.com/Products/MinInvasive/Pages/hemodynamicpocketcard.aspx
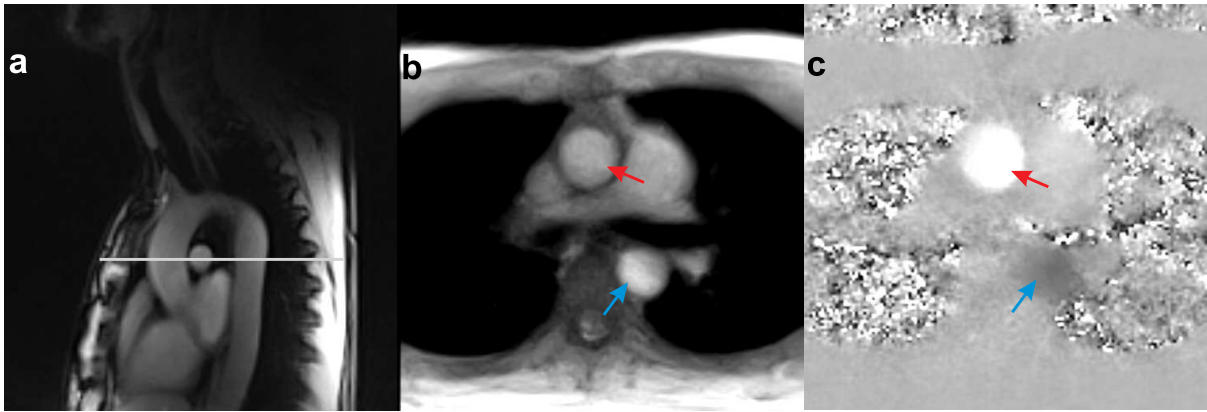
Figure 5.30: Real-time PC MRI of through-plane flow in the ascending aorta. (a) sagittal view of the human aortic arch with transverse slice orientation, (b) magnitude image and (c) phase-contrast map of the transversal view. Arrows indicate the flow in ascending aorta (red) and descending aorta (blue).

The magnitude image and phase-contrast map from a real-time PC MRI acquisition during strong systolic flow are displayed in Figure 5.30. The regions of ascending aorta and descending aorta are marked in red and blue arrows, respectively. The phase-contrast maps have regions of ascending aorta and descending aorta represented as white and black, respectively, according to the direction of flow. The magnitude image and the phase-contrast map obtained are of good quality even at extreme undersampling factor of 32, that is 7 spokes relative to formally required number of $144 \times \frac{\pi}{2} = 226$ spokes. Marginal streaking artifacts outside the region of interest are sometimes observed in the phase-contrast map which has no temporal filtering. For quantitative flow studies, the quantification of ascending aorta is significant as the flow parameters obtained indicate the physical state of the left ventricle.

Flow images acquired by MRI using phase-contrast imaging technique consists of three dimensions, two spatial and one velocity dimension with time as the fourth dimension for the real-time PC MRI. Two dimensional flow profiles can be displayed from the phase information obtained from the phase-contrast maps. Figure 5.31 visualizes the two-dimensional flow profile within the ascending aorta by color-coded velocities ranging from 0 (blue) to 100 cm s^{-1}(red). The flow profiles gives important insights into the flow properties in the blood vessel. Flow in the human body is mostly believed to be laminar in nature which is clearly seen in Figure 5.31. Flow in the human body can also be turbulent or complex in nature depending on the region imaged (e.g. ventricles of heart). Flow profiles over time provide large amount of data for quantitative analysis. The flow profiles for cardio-vascular studies can be compared within and between cardiac cycles.

Figure 5.32 shows the dynamic distributions of flow in the ascending aorta from the real-time
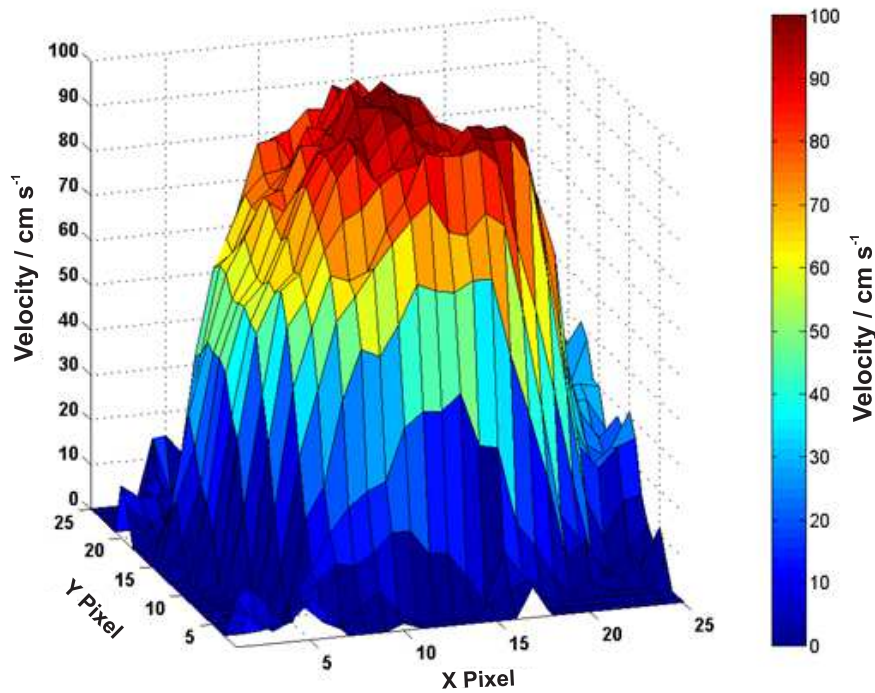
Figure 5.31: Real-time flow velocities (color-coded range from 0 to 100 cm s^{-1}) over the lumen of the ascending aorta during the peak systolic phase of a single cardiac cycle.

data at a temporal resolution of 40 ms. The flow profiles represented are from the systole and diastole of a single cardiac cycle. The through-plane flow in the ascending aorta is mainly laminar in nature as observed from the images. A series of 12 consecutive profiles (total duration, 480 ms) covering the early phase of a single cardiac cycle is shown from top view in Figure 5.33. In this subject, the velocity increases to a peak value of 90 cm s^{-1}(red) within about 150 ms (three frames). During the diastolic phase of the heart, a percentage of blood ejected through ascending aorta flows back to the coronary artery. This phenomenon can be clearly observed in Figure 5.33 where the reverse flow of blood with velocities of up to 30 cm s^{-1} is indicated in dark blue and arrow in frames 6 to 10.

Since the descending aorta can also be viewed from the transversal view, respective flow parameters can also be obtained from descending aorta. Figure 5.34 shows flow rate of ascending and descending aorta for single cardiac cycle. On a closer observation, a shift between the peak flow values of ascending and descending aorta can be noticed. This shift of around 80 ms in peak values is mainly observed due to the high temporal resolution (40 ms) obtained from real-time PC MRI.

Further the variation of flow over ascending and descending aorta can be observed in Figure 5.35 for 15 cardiac cycles. Flow rate in descending aorta is lower than in the ascending aorta
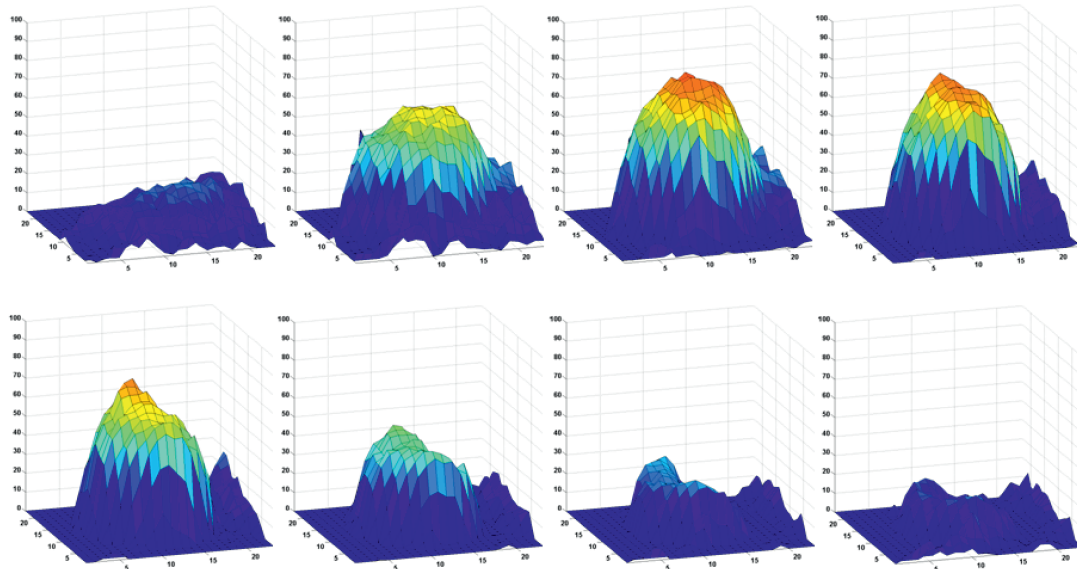
Figure 5.32: Real-time flow velocities (color-coded range from 0 to 100 cm s^{-1}) over the lumen of the ascending aorta during a single cardiac cycle.
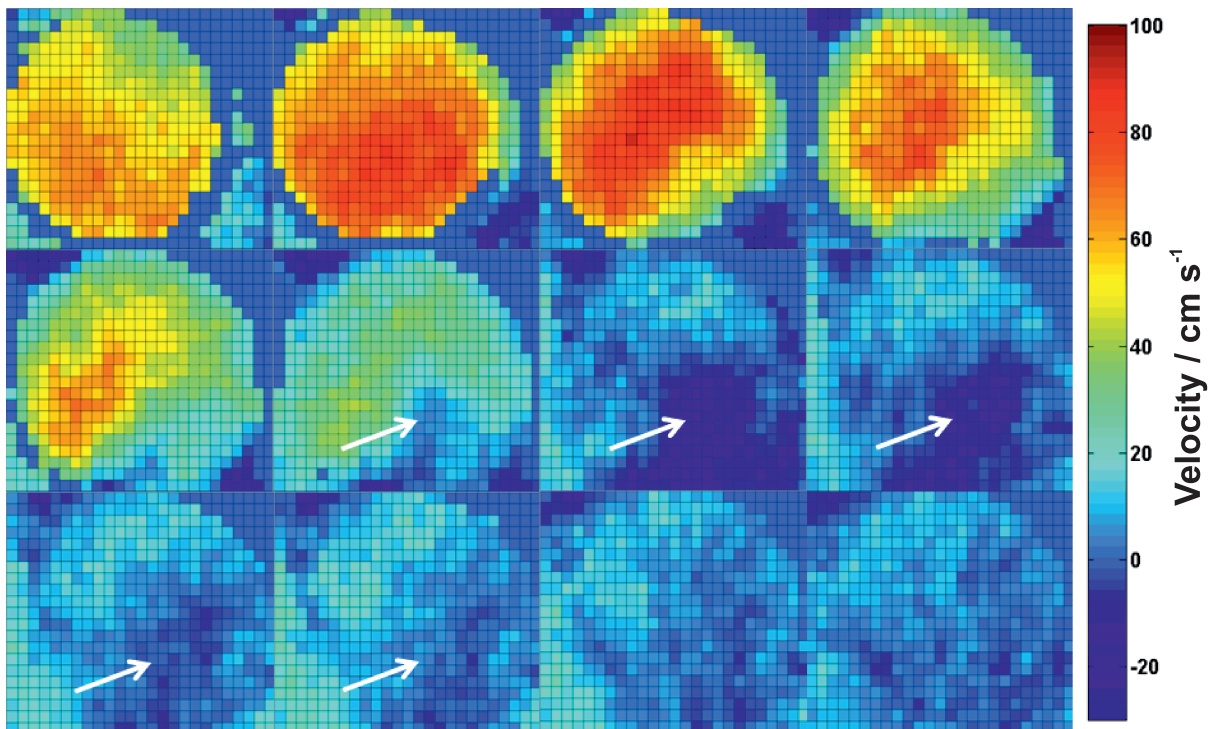

Figure 5.33: Real-time flow velocities (color-coded range from -30 to 100 cm s^{-1}) within the ascending aorta (25 × 21 pixels) at 12 consecutive time points during the early phase of a single cardiac cycle (spatial resolution 1.3 × 1.3 × 6 mm^3; temporal resolution 40 ms; total duration 12 × 40 ms = 480 ms). Arrow indicates back flow (blue).
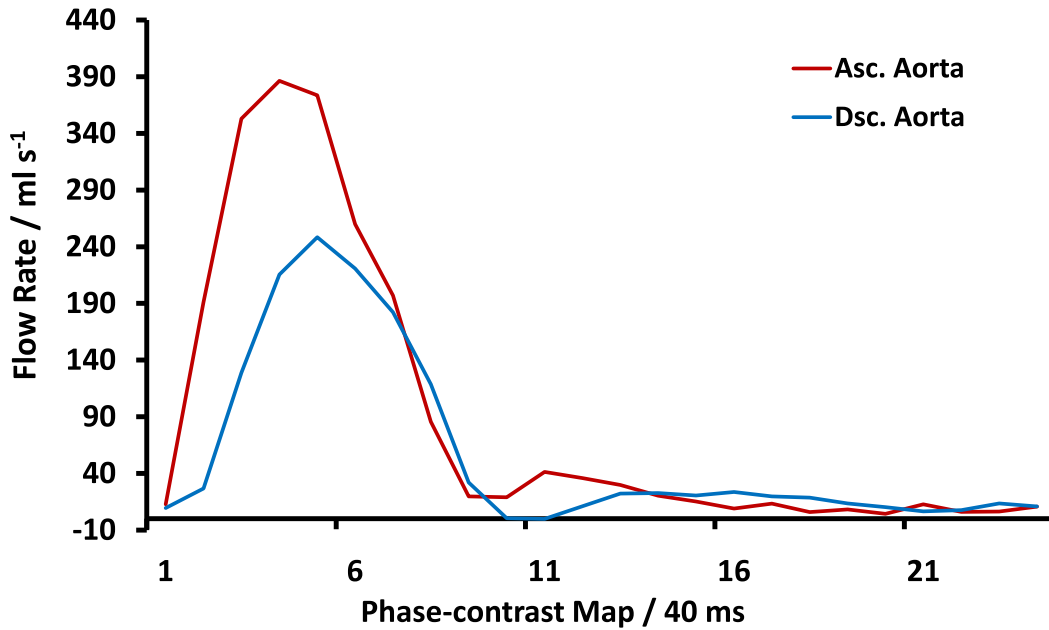
Figure 5.34: Graph represents the flow rate in ascending and descending aorta for a single cardiac cycle.

due to the arterial blood supply of the brain/head. The variation of flow rates over cardiac cycles proves the importance of real-time PC MRI to observe the variations in quantitative values. On a closer analysis, the variation of maximum flow rates for ascending and descending aorta correlates to respiration if fitted with the breathing curve. Inter-variability of flow is also consistent with physiology of heart where flow varies with heart rate and respiration. These results indicate the advantage of real-time PC MRI whose quantitative values are close to predicted physiology of the heart.

Quantitative results obtained for a subject using real-time PC MRI is summarized in Table 5.11 for free breathing. All flow parameters (mean ± standard deviation) of ascending and descending aorta indicate the values across 15 cardiac cycles. The observed standard deviation in flow parameters represent the physiological variation of hemodynamics in response to parameters such as, for example, body composition, blood pressure and alertness during MRI. Higher peak velocity and average velocity is observed in descending aorta as compared to ascending aorta. On the other hand flow rate, stroke volume and volume were higher for ascending aorta. The values observed for flow parameters were found to be normal in accordance with the literature.

5.2.3 Cine PC MRI

The standard phase-contrast MRI technique used over the years for flow studies is called Cine PC MRI. Cine PC MRI involves the interpolation of data acquired from multiple cardiac cycles
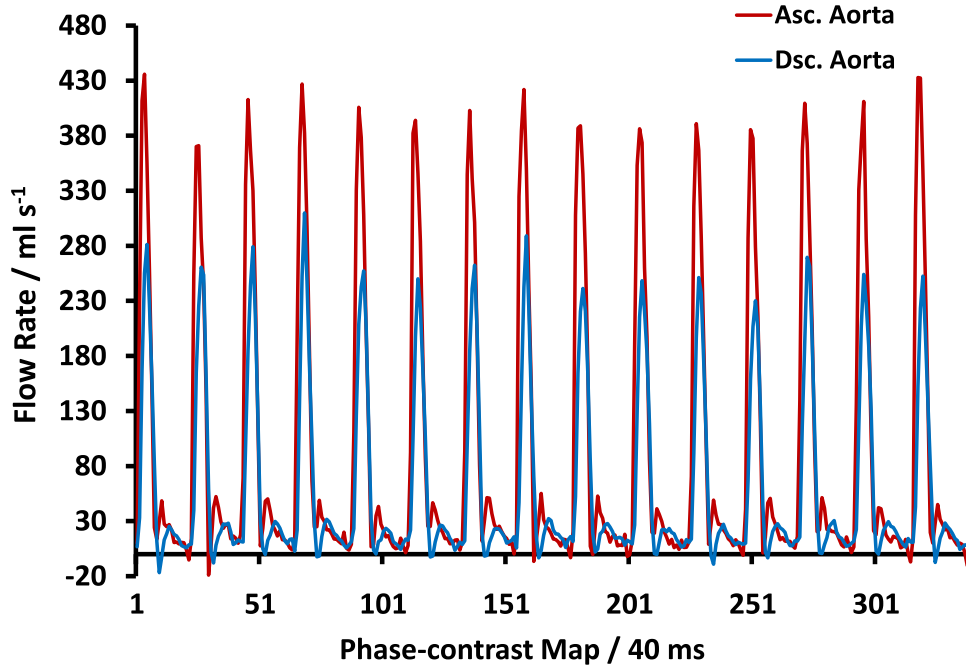
70

Figure 5.35: Graph represents the flow rate over phase-contrast maps in ascending and descending aorta for 15 cardiac cycles obtained through real-time PC MRI.

Flow Parameters	Ascending Aorta	Descending Aorta
Heart Rate (Beats min^1)	62 ± 3	62 ± 3
Peak Velocity (cm s^1)	90 ± 7	103 ± 7
Average Velocity (cm s^1)	14 ± 0	18 ± 0
Flow Rate (ml s^1)	94 ± 3	61 ± 2
Stroke Volume (ml)	91 ± 3	59 ± 2
Volume (l min^1)	5.6 ± 0.2	3.6 ± 0.1

Table 5.11: Values are given as mean $\pm$ standard deviation (SD) represent the flow parameters obtained using real-time PC MRI for a subject across 15 heartbeats under free breathing condition.

into images of a single cardiac cycle [121]. Cine imaging is performed under both free breathing and breathhold conditions [122–126]. In cine imaging, each cardiac cycle is divided into cardiac phases according to ECG triggering for the effective acquisition of k-space lines as shown in Figure 5.36. For each cardiac cycle, the k-space lines acquired are sorted according to the cardiac phases and ECG trigger times. This process is repeated for multiple cardiac cycles until k-space is filled completely. Each cardiac phase represents a complete k-space and subsequently an image obtained from Fourier transformation. Cine breathhold requires the subject to hold breath for about 15 s during the image acquisition phase to avoid artifacts. This procedure can be strenuous to patients suffering from cardiovascular diseases. Moreover, the flow values obtained under breathholding condition can be higher to actual physiological condition due to increased high intra-thoracic pressure involved [127]. Free breathing for cine phase-contrast imaging is usually performed with navigator ECG gating which help to retrospectively reconstruct the acquired data. Navigator pulses are used to acquire lines in k-space only at constant phase of respiratory cycle. Further, it assumes that the physiological parameters such as heart rate remain constant over all cardiac cycles and interpolates the acquired data to one synthetic cardiac cycle. This technique is susceptible to abnormal cardiovascular conditions such as cardiac arrhythmias where irregular heartbeats are observed. The imaging time for cine free breathing is around 3 minutes which is quite long considering multiple measurements for a diagnostic test.
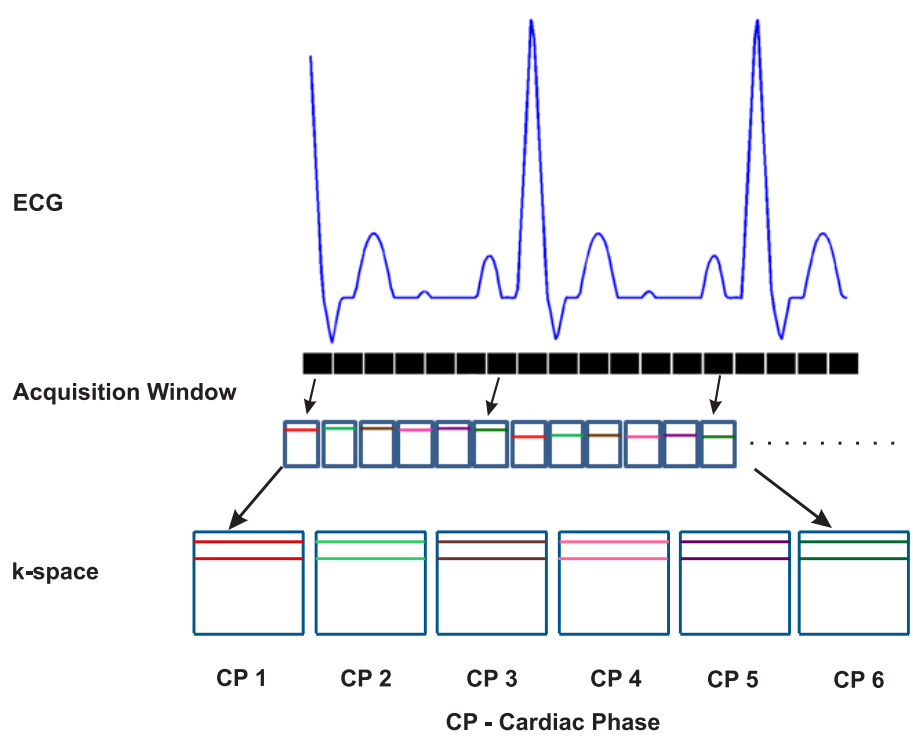

Figure 5.36: Schematic representation of cine imaging for the acquisition of images from five cardiac phases (CP) of the ECG synchronized heart cycle.

5.2.4 Evaluation of Real-time PC MRI

Clinical evaluation of any imaging method is essential in order to be used for patient diagnosis. Real-time PC MRI as quantitative method has to be evaluated extensively to prove its applicability in diagnostic imaging. During the past decade, flow studies using phase-contrast imaging have been performed with ECG-synchronized cine acquisitions which is considered as the gold standard for flow studies [128]. A study was conducted to evaluate real-time PC MRI for through-plane flow of ascending aorta at high spatial and temporal resolutions. The results discussed are also part of a journal paper by the author of this thesis [117].

Volunteers (n = 10, male) between the age 20 - 30 with no known illness were used for this study. Cine breathhold and free breathing methods normally used in the clinical setup provided by the vendor were used for the purpose. The improved version of the real-time PC MRI sequence consisting of overlapped motion compensation slice gradients, flow gradients, and read dephasing gradients were used for this study. The improved version of real-time PC MRI allows imaging with high temporal resolution of 40 ms. The spatial resolution of the free breathing cine and real-time methods were kept constant $1.3 \times 1.3 \times 6$ mm^3 for evaluation. The parameters used for real-time and cine imaging are shown in the Table 5.12. The cine phase-contrast maps were reconstructed using GRAPPA [71] with an acceleration factor of 2 and 24 reference lines. Two variants of real-time PC MRI such as sequential and interleaved, as explained previously was used for the study. Reconstructed real-time magnitude images and phase-contrast maps were displayed online at the scanner console which was possible through the bypass of measured k-space data to an external reconstruction system consisting of two packs of four graphical processing units (GPU) [88]. The measurements for the real-time methods consisted of a acquisition time around 15 s producing about 370 magnitude images and phase-contrast maps. Images for all the methods were acquired with electrocardiographic (ECG) time stamps which were necessary for cine and real-time methods for cine retrospective reconstruction and multiple cardiac cycles analysis, respectively. For each subject, the cine and real-time methods were repeated threefold in a pseudo-randomized order with the total measuring time of 30 minutes per subject. Additionally, phantom measurements were performed for each subject for the analysis of the generated phase offset errors. Simulated ECG signal was used for phantom measurements along with the same scan parameters as used for ascending aorta. Ten continuous cardiac cycles data obtained from the real-time methods were used for analysis.

The magnitude images and phase-contrast maps from the systolic and diastolic phases obtained from the cine free breathing, cine breathhold, real-time sequential and real-time interleaved are displayed in the Figure 5.37. It is observed that the real-time methods provide good quality images for systolic and diastolic phase of the cardiac cycles. Large FOV is used for cine imaging

73

Scan Parameters	Cine Free Breathing	Cine Breathhold	Real-time Methods
TR/TE/α	20.05/2.18 ms/25°	46.90/1.92 ms/25°	2.86/1.93 ms/10°
Slice Thickness (mm)	6	6	6
Radial Spokes	-	-	7
VENC (cm s^{-1})	200	200	200
Averages	3	1	1
Segments	2	5	-
FOV (mm)	320	320	192
FOV read (%)	75	68.8	100
Base Resolution	256	192	144
Cardiac Phases	30	20	-
Reconstruction	GRAPPA	GRAPPA	NLINV

Table 5.12: Scan parameters used for the evaluation between cine and real-time PC MRI
.

Methods	Maximum Spatial Average Velocity (cm s^{-1})	Average Velocity (cm s^{-1})
Cine Breathhold	1.65	1.10
Cine	-0.21	-0.12
Real-time Interleaved	2.88	0.07
Real-time Sequential	2.38	0.05

Table 5.13: Phase offset values in cm s^{-1} (mean $\pm$ SD) for the ascending aorta. Cine imaging: n = 10 subjects; real-time methods: n = 10 subjects, 10 heartbeats.

in order to avoid aliasing artifacts. In contrast, real-time images with small FOV suffers only from minimal streaking artifacts. Small FOV in real-time images help in better delineation of the region of interest. Moreover, real-time methods provide better images with good contrast in diastolic phase as compared to cine imaging which can influence the image segmentation and quantitative analysis.

The evaluation of phase offsets through maximum spatial average velocity and spatio-temporal average velocity is represented in Table 5.13. Real-time methods produce errors in terms of maximum spatial average velocity and average velocity of around 1% and lesser than 1% respectively. These values are well below the prescribed acceptable limits of 5% [116].

The spatially averaged peak velocities over ascending aorta obtained using the cine and real-time methods is shown in Table 5.14. There is no significant difference between the velocity values obtained from real-time methods and cine breathhold. Minor deviations of 2.6 % occur between real-time methods and cine free breathing method. These results show that real-time methods produce comparative results to cine imaging.
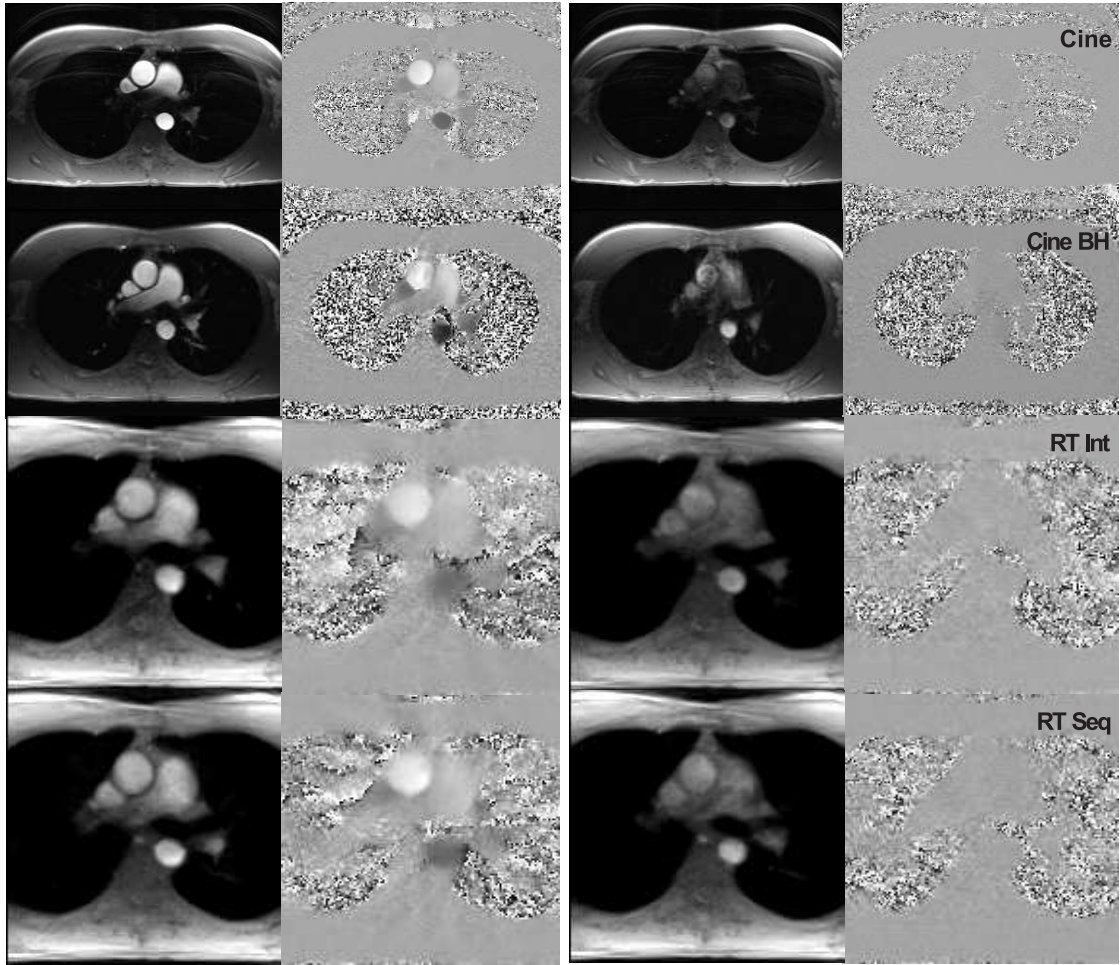
Figure 5.37: Transverse view of the human heart at the region of ascending aorta: magnitude images and phase-contrast maps as obtained by cine free breathing (cine), cine breathhold (Cine BH), real-time interleaved (RT Int) and real-time sequential (RT Seq) during the peak systolic (left) and diastolic phases (right) of the heart.

Methods	Spatial Average Velocity
Cine Breathhold	82.9 ± 7.9
Cine	80.6 ± 6.6
Real-time Interleaved	82.8 ± 10.2
Real-time Sequential	82.6 ± 10.1

Table 5.14: Spatial average velocity in cm s^{-1} (mean $\pm$ SD) for ascending aorta. Cine imaging: n = 10 subjects, 3 repetitions; real-time methods: n = 10 subjects, 3 repetitions, 10 heartbeats.

The flow profile of real-time interleaved and sequential methods of a single subject for 10 consecutive cardiac cycles is represented in Figure 5.38. It is observed that interleaved and sequential methods have no major differences in flow profiles with dips below zero occurring for few cardiac cycles of sequential method. The peak of flow rates for each cardiac cycle show fluctuations according to the respiratory cycle (3-4 s, respiration rate of 15-20 min^{-1}).
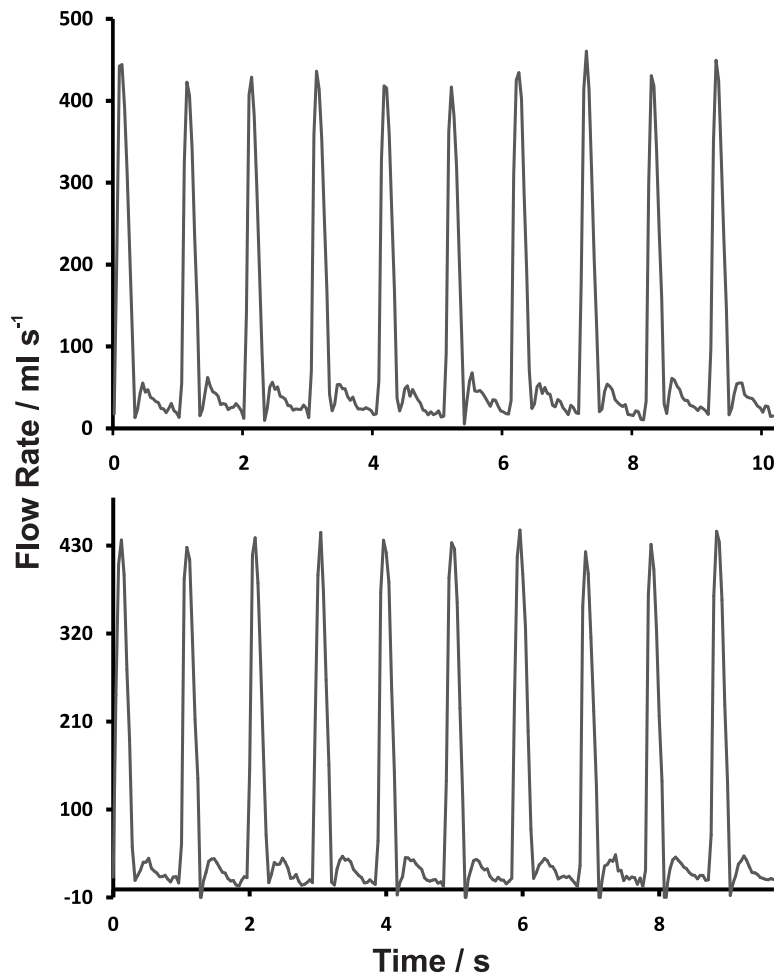

Figure 5.38: Representation of flow rates of 10 consecutive cardiac cycles for real-time interleaved (top) and sequential methods (bottom) methods over the ascending aorta.

The comparison of peak velocity for cine acquisitions and real-time MRI methods is displayed in Figure 5.39. The peak velocity values between real-time acquisitions and cine recordings are similar for lower peak velocity values, whereas for higher velocities the real-time methods show higher values to cine recordings. The correlation coefficient (r^2) between interleaved-cine, sequential-cine and interleaved-sequential were 0.817, 0.826 and 0.932, respectively. The peak velocities obtained from real-time interleaved and real-time sequential were similar to each other with no major differences. Bland-Altman analysis [129], which is a method to compare a

76

standard reference method with new method, was also performed on cine and real-time acquisitions. The bias in peak velocity for real-time methods was 4% (around -7 cm s^{-1}) less than cine recordings. The minimal bias of -0.2 cm s^{-1} between the real-time methods indicate that the similarity in peak velocity values and robustness of the real-time methods for velocity measurements. The limits of agreement for cine-interleaved, cine-sequential and interleaved-sequential were -29.2 to 15.5 cm s^{-1}, -28.6 to 14.5 cm s^{-1} and -11.5 to 11 cm s^{-1}, respectively. Higher peak velocities are observed for real-time PC MRI for high-flow conditions above 120 cm s^{-1}. This may be indeed correct as lower values in cine recordings is possible by phase averaging due to the usage of data from multiple heartbeats. These explanations are consistent with findings reported that cine MRI leads to lower peak velocities than observed by Doppler ultrasound techniques [109]. Further, these results questions the reliability of cine MRI methods as a standard reference method for in vivo flow measurements. It should be noted that for cine recordings it is difficult to show exactly the cardiac cycle where the peak velocity values were obtained as the measurement generally covers multiple cardiac cycles and phases.

Comparison of stroke volume for cine acquisitions and real-time MRI methods is shown in Figure 5.40. Correlation coefficient r^2 between interleaved-cine, sequential-cine and interleaved-sequential were 0.952, 0.956 and 0.978, respectively. Higher stroke volume values are observed for real-time interleaved in comparison to cine recordings and real-time sequential method. Cine recordings have higher stroke volumes compared to real-time sequential method. These results can also be validated through the Bland-Altman plots where the bias for cine-interleaved, cine-sequential and interleaved-sequential were -5.7 ml cycle^{-1}, 3.3 ml cycle^{-1} and 9.1 ml cycle^{-1}. The limits of agreement for cine-interleaved, cine-sequential and interleaved-sequential were -12.5 to 1.1 ml cycle^{-1}, -3.1 to 9.9 ml cycle^{-1} and 13.3 to 4.9 ml cycle^{-1}. The mean difference in stroke volume obtained for both real-time methods was below 5% of the standard stroke volume, which is acceptable to clinical standards.

Stroke volume represents the flow, which is a function of aortic areas and spatially averaged velocities, integrated over the duration of the cardiac cycle. Therefore the analysis of spatial averaged velocity would aid in understanding the observed deviations between the real-time methods in stroke volume. Figure 5.41 represents the comparison of spatially averaged velocities as obtained for real-time methods (mean ± SD, 1 subject, 3 repetitions, 10 heartbeats). The phase-contrast maps of 3 repetitions for each method were combined into a single dataset with the individual images sorted according to the ECG time stamps. The spatial average velocity profile clearly shows the difference between real-time interleaved and sequential methods. The velocity profile of sequential method during the systolic phase is narrower compared to interleaved method. Further during the diastolic phase, the velocity values obtained are lower
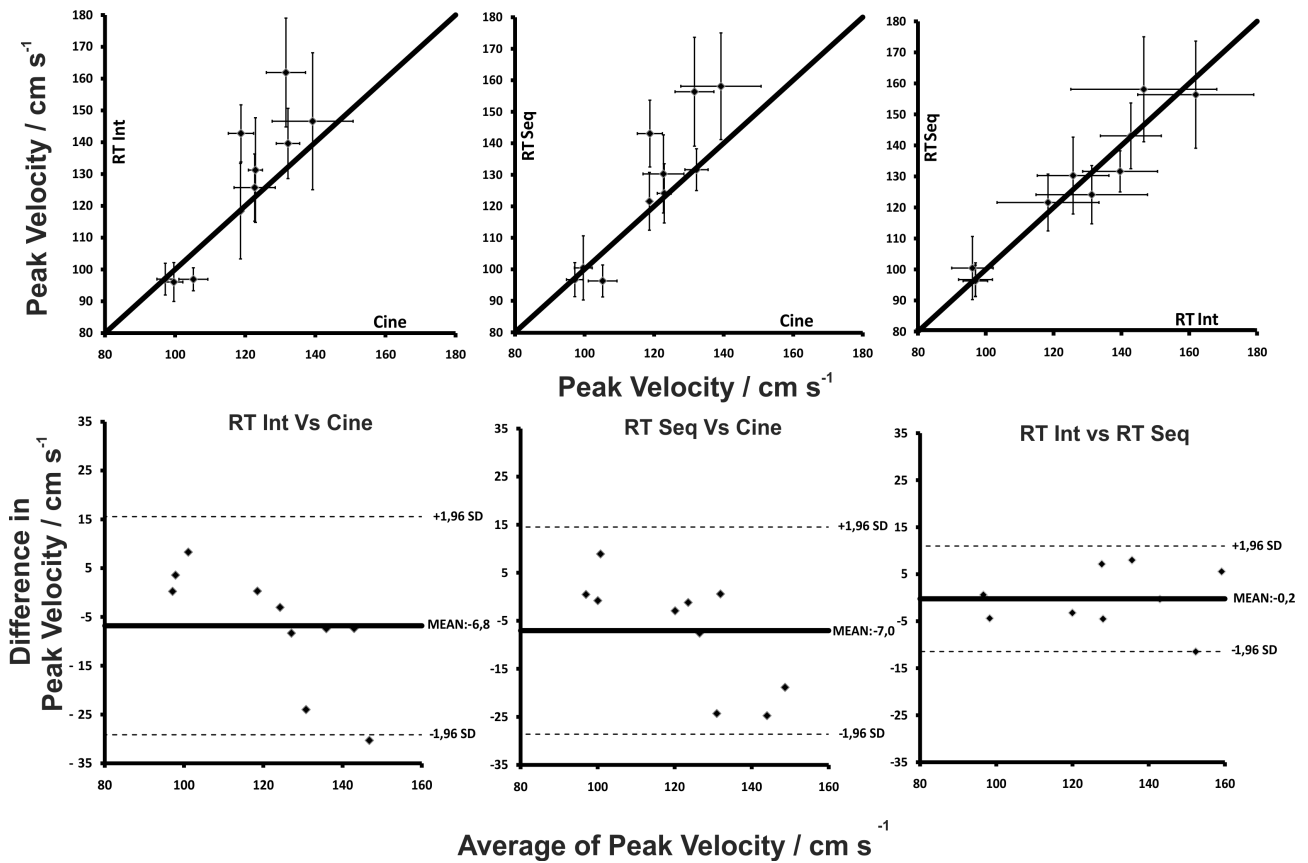
Figure 5.39: Comparison of peak velocities between real-time methods and cine imaging; (Top) Peak velocities (mean ± SD) for real-time flow MRI with interleaved (RT Int) and sequential (RT Seq) flow encoding (10 subjects, 3 repetitions, 10 heartbeats) vs cine MRI recordings during free breathing (Cine, 10 subjects, 3 repetitions). (Bottom) Corresponding Bland-Altman plots of the difference in peak velocity between cine MRI and real-time MRI. Broken lines refer to ± 1.96 SD indicating limits of agreement.
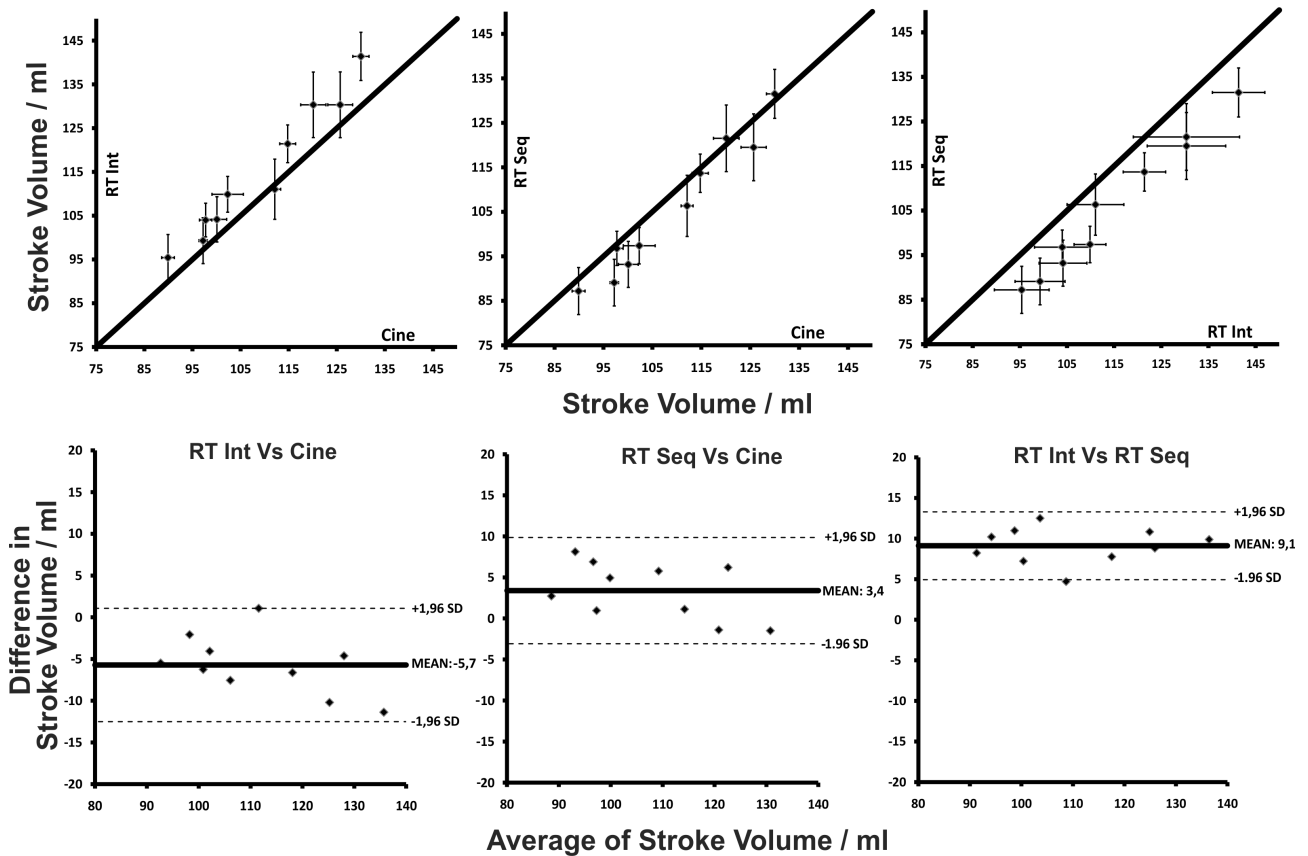
Figure 5.40: Comparison of stroke volume between real-time methods and cine imaging; (Top) Stroke volumes (mean ± SD) for real-time flow MRI with interleaved (RT Int) and sequential (RT Seq) flow encoding (10 subjects, 3 repetitions, 10 heartbeats) vs cine MRI recordings during free breathing (Cine, 10 subjects, 3 repetitions). (Bottom) Corresponding Bland-Altman plots of the difference in stroke volume between cine MRI and real-time MRI. Broken lines refer to ± 1.96 SD indicating limits of agreement.

compared to interleaved method. It has been already shown that interleaved and sequential methods differ in the order of k-space acquisition with flow gradients. In the current implementation, the actual time span over which the bipolar velocity gradient is applied to define a phase-contrast map for interleaved and sequential version were 40 and 20 ms, respectively. This is because in the Zero-Max case used here the other image is without any flow-encoding gradient. This feature aids in observing minor details using sequential method such as the velocities below zero in the late systolic phase. The lower traces or dip in velocities observed through sequential method is a physiological phenomenon caused by the rapid closure of the aortic valves and usually not observed for MRI sequences.
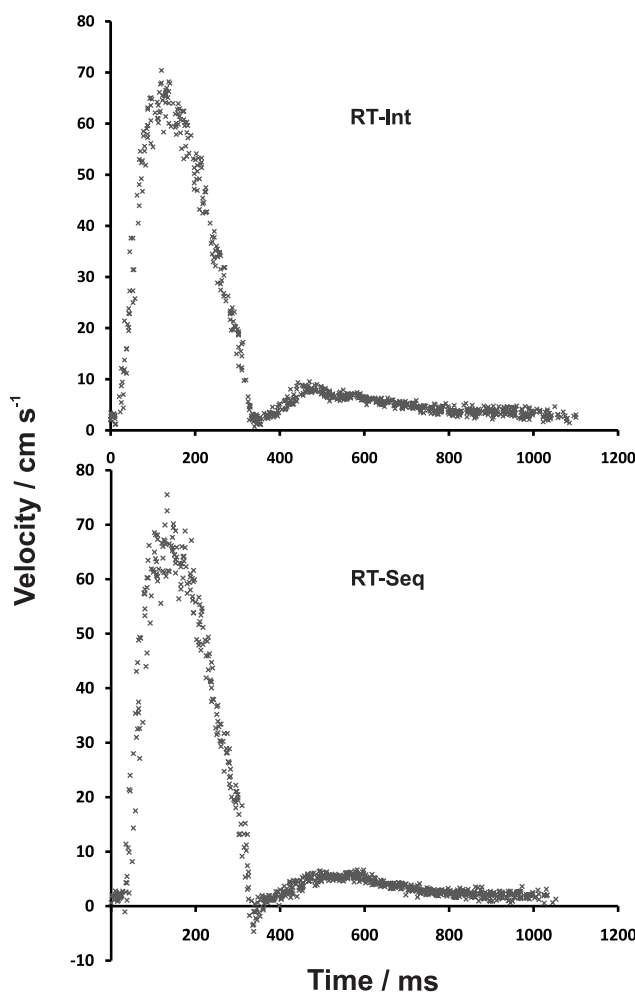

Figure 5.41: Representation of spatially averaged velocities for single subject (repetitions = 3, cardiac cycles = 10) for real-time interleaved (top) and sequential methods (bottom) sorted according to the R wave.

In this study, the real-time methods provided results comparable to cine imaging at high spatial and temporal resolution. Further the images obtained from real-time methods were of adequate

quality. In comparison to conventional cine phase-contrast MRI with free breathing, which emerges as a widespread clinical standard, real-time MRI offers a substantial gain in measuring time. Moreover, quantitative evaluations are within clinically acceptable standards and confirm the ability to obtain reliable flow parameters.

5.2.5 Summary

A quantitative validation of the real-time PC MRI methods under in vivo conditions is of utmost importance for clinical acceptance. Cardiovascular blood vessels such as the ascending and descending aorta were selected for the quantitative analysis due to their importance in blood transportation. Analysis of flow in these vessels act as a bio-marker for potential cardiovascular diseases. The developed real-time PC MRI technique was evaluated and validated with the conventional Cine PC MRI technique under free breathing conditions. The results show that real-time PC MRI methods are reliable and produce comparable results to conventional PC MRI. However, the usage of cine PC MRI as a gold standard or reference for comparison with real-time studies is questionable as the values obtained from cine recordings are due to the interpolation of phase data from multiple cardiac cycles. Differences in the quantitative flow parameters were observed in the real-time interleaved and sequential methods. The differences occur due to the actual physical implementation. Although these differences are minimal, its impact on the quantitative analysis would be highly dependent on the nature of flow measured. It is assumed that the differences between real-time methods will only be observed during high flow conditions which is equal or faster than 40 ms temporal resolution per phase-contrast map. As sequential method would assist in all flow conditions, it is more preferred for future use. The quantitative analysis and comparable results to the conventional cine PC MRI suggest that the real-time method can be implemented for clinical diagnosis and patient studies. Apart from reducing the total acquisition time, real-time flow MRI provides unique access to physiological variances in flow during different cardiac cycles. This property of real-time PC MRI allows for the assessment of irregularities from heartbeat to heartbeat which is not possible through ECG-dependent cine recordings.

Chapter 6

Methodological Extensions

Real-time PC MRI technique, as shown in previous chapter, has demonstrated its reliability and applicability to monitor irregular cardiovascular physiology thereby achieving the primary goals of this thesis. Extensions focusing on further improvements and modifications to the real-time PC MRI method were performed as part of this thesis. This chapter illustrates two such extensions, namely dual-echo real-time PC MRI and multi-directional flow. While dual-echo real-time PC MRI was primarily experimented to attain higher temporal resolutions, multi-directional flow MRI aims to extend the velocity encoding to other gradient axes.

6.1 Dual-Echo Real-time PC MRI

The development of real-time PC MRI primarily focuses on achieving high temporal resolution and short acquisition time. These properties are very important for many diagnostic applications especially cardiovascular imaging. The real-time PC MRI technique, as discussed in previous chapters, achieved a temporal resolution of 40 ms and short examination times of a few seconds. Although high temporal resolution has been achieved from real-time PC MRI implementation, a consistent effort is always directed into exploring ways to increase temporal resolution. In this section, a strategy of employing dual-echo in real-time PC MRI for achieving shorter acquisition time and higher temporal resolution has been experimented. The principle and implementation of dual-echo real-time PC MRI are explained with the results obtained. Further the limitations of using this technique for future real-time PC MRI studies are discussed.

6.1.1 Principle

Phase-contrast MRI using multiple echoes was proposed by Firmin et al. [130], where velocity mapping was performed using echo-planar imaging [13,14]. Echo-planar imaging is a single-shot

technique which acquires multiple views of k-space through multiple echoes thereby achieving high temporal resolution. This method was evaluated for cine PC MRI in both in vitro and in vivo conditions by Debatin et al. [131] along with further modifications [47, 132, 133]. Johnson et al. [134] used dual echoes and radial undersampling to acquire phase-contrast maps. Here the phase-reference and velocity-encoded scan were acquired at different repetitions with two echoes primarily used to increase the information content for reconstruction. Pai [135] proposed a different dual-echo PC MRI method where velocity encoding gradients were placed between two echoes with Cartesian encoding scheme. Since phase-reference and velocity-encoded information were acquired within a single repetition, it led to a decrease in total acquisition time. Rolf et al. [136] evaluated the implementation of Pai [135] for cardiac output measurements and found the method to produce inconsistent quantitative results. It was also inferred that phase-contrast maps were sensitive to fat-water shifts and B_0 offsets. Further, a strong drift of velocity offset over time due to the high duty cycle of the gradients was noticed. Rolf et al. [136] further suggested that implementation of the dual echo PC MRI at higher static magnetic fields such as 3T is feasible, as phase offsets generated are minimal due to the minimization of fat-water shifts.

The previous studies employed undersampled Cartesian encoding scheme along with cine imaging where artifacts due to pulsatile blood flow were observed in the phase encoding direction. Since radial encoding scheme is robust to motion and less sensitive to undersampling, it could reduce many artifacts discussed in previous studies. Further, NLINV can reconstruct qualitative images even at higher undersampling. In this study, the feasibility of combining dual-echo PC sequence with radial encoding scheme and NLINV reconstruction for real-time PC MRI is studied.

The principle of real-time radial FLASH dual-echo PC MRI is depicted as a schematic representation in Figure 6.1. A flyback gradient is present in between the two echoes represented by their respective echo times (TE1 and TE2). The bipolar flow gradients are also played in the slice selection (z) direction along with the flyback gradient. The sequence from overlapping of gradients (slice, x, y), was optimized in order to obtain the shortest repetition time. The scan parameters used for the study were flip angle 10°,TR/TE1/TE2 = 4.16/1.36/3.4 ms, spatial resolution of $1.8 \times 1.8 \times 8$ mm^3 and 7 spokes providing a temporal resolution of 29 ms. In order to analyze the phase offset generated, each measurement was repeated twice with and without flow gradients and respective phase-contrast maps were obtained.

6.1.2   In Vitro Studies

In vitro studies were performed on tubular phantom in order to validate dual-echo PC MRI. The magnitude and phase-contrast maps obtained with and without velocity encoding gradi-
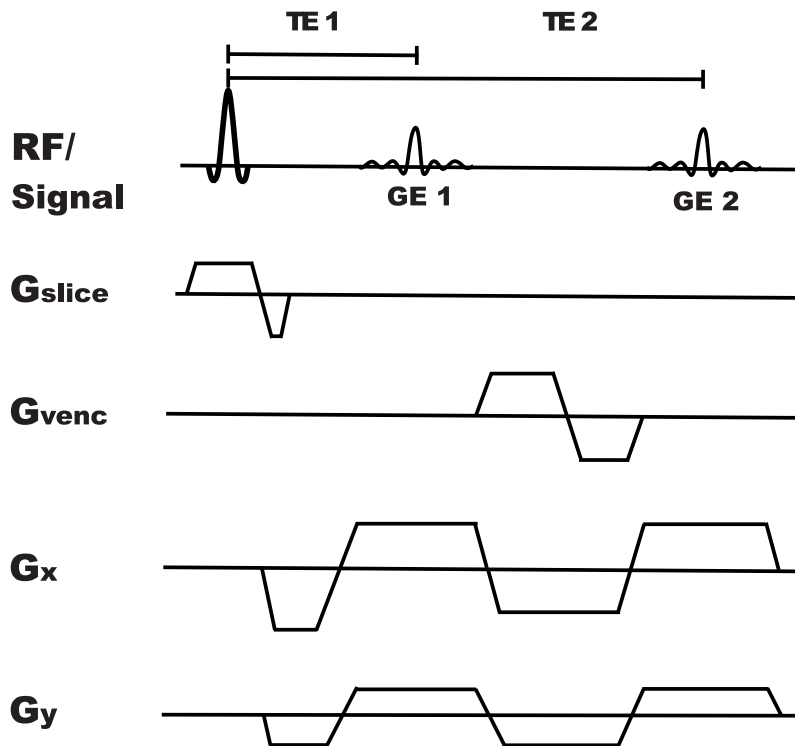
Figure 6.1: Schematic representation of the pulse sequence used for real-time dual-echo PC MRI. The sequence is based on the radial encoding scheme. The independent bipolar flow gradients are represented separately in G_{venc}. The flyback gradients separate two echoes acquired.

ents are displayed in Figure 6.2. A constant flow of around 4.5 l min^{-1} is maintained within the tube. No major artifacts are observed in the magnitude images even at high undersampling of 7 spokes per image. Minimal streaking artifacts associated with radial encoding scheme is observed away from the flow regions. The through plane flow within the tubes of the tubular phantom is clearly observed from the phase-contrast maps. The phase-contrast map obtained without the flow encoding gradient is fairly homogeneous in nature which indicates a constant phase offset present.

Large tube with a large diameter within the tubular phantom was chosen to analyze flow due to its similarity to the large blood vessels of human body and presence of negligible turbulent flow. Figure 6.3 shows the spatial average velocity profile obtained from the phase-contrast maps with and without velocity encoding gradients. The mean velocity as observed in the figure represents a constant flow within the tube and was calculated to be around 4.5 l min^{-1} with phase offset correction. The phase offset values obtained as represented in the figure were also constant without any major deviations.
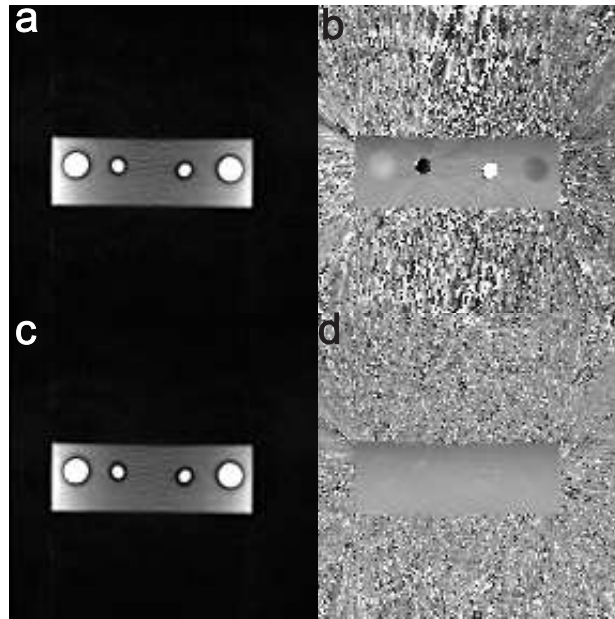
Figure 6.2: (a, c) Magnitude images and (b, d) phase-contrast maps obtained (a, b) with and (c, d) without velocity encoding on the flow phantom using real-time dual-echo PC MRI.
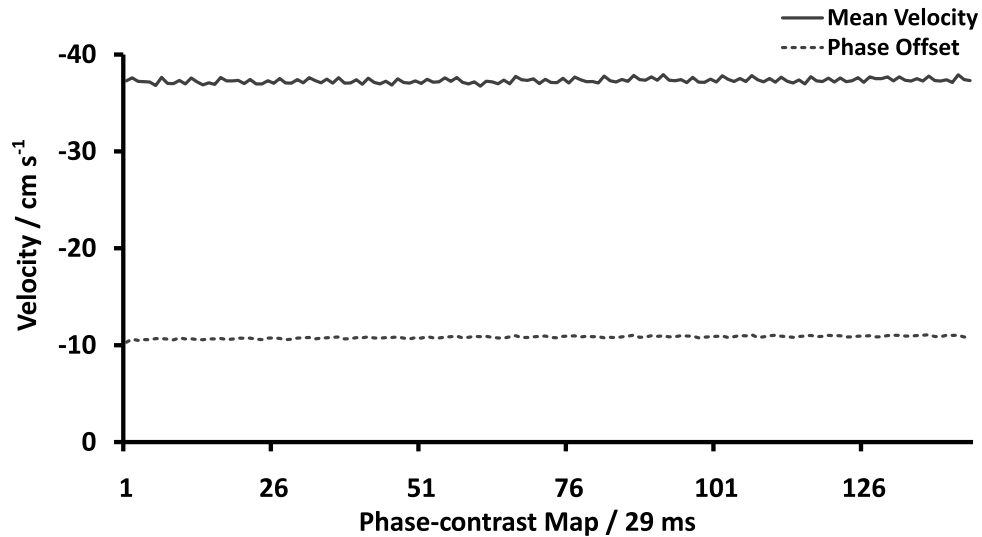

Figure 6.3: Representation of spatial average velocity and phase offset obtained from phase-contrast maps for a region of interest (large tube) under constant flow conditions. The phase offset represents the additional phase induced by B_0 inhomogenities.

6.1.3 In Vivo Studies

In vivo studies using the real-time dual-echo PC MRI were performed with ascending aorta as the region of interest. Experiments were performed with the same parameters as used for in vitro studies. Figure 6.4 shows the magnitude and phase-contrast maps obtained with and without velocity encoding gradients. The magnitude images and phase-contrast maps are reconstructed without the application of median filter. The muscles and blood vessels of the heart are clearly observed without any major artifacts in the magnitude images. Clear delineation of the muscle structures in the magnitude images is due to echo times at in-phase/opposed-phase. No major artifacts are observed in the respective phase-contrast maps obtained.
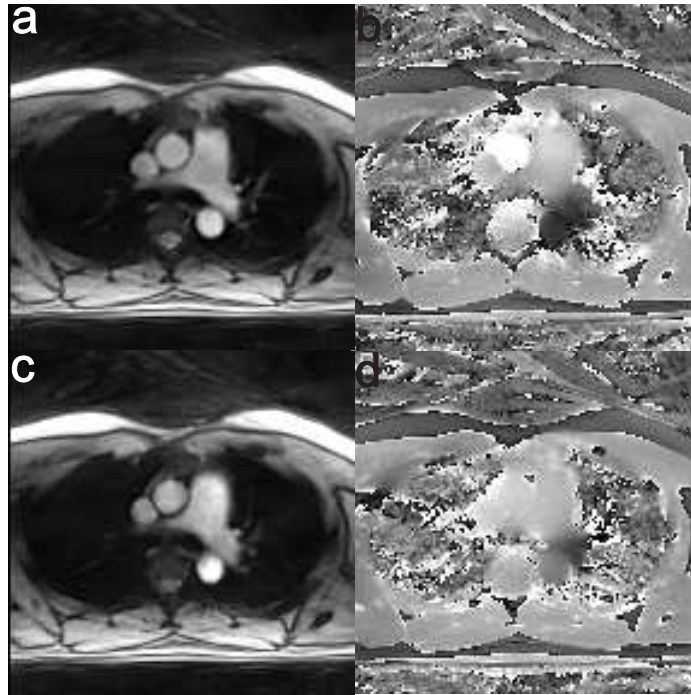

Figure 6.4: Transverse view of the human heart at the region of ascending aorta: (a, c) magnitude images and (b, d) phase-contrast maps obtained (a, b) with and (c, d) without velocity encoding using real-time dual-echo PC MRI.

Spatial average velocity profile at the ascending aorta from phase-contrast maps with velocity encoding gradient is represented in Figure 6.5. The flow profiles for individual cardiac cycles are similar to those obtained from standard phase-contrast imaging. However, fluctuations in velocity profiles are present especially in the diastolic part of the individual cardiac cycles. Further, the superimposition of breathing cycle for multiple cardiac cycles is also observed. The influence of breathing cycle is proven from the spatial average velocity profile obtained from phase-contrast maps without velocity encoding gradient as shown in Figure 6.6. This velocity profile representing the phase offset present due to B_0 inhomogenities has to be constant as

observed from in vitro studies. However, it is clearly observed that the breathing cycle has its influence on the fluctuations of phase offset values.
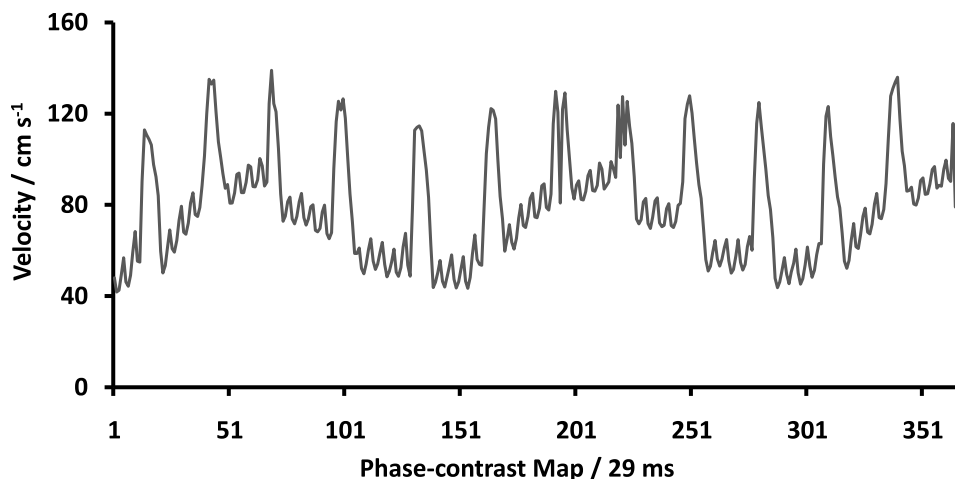

Figure 6.5: Representation of spatial average velocity obtained from phase-contrast maps with flow gradients for ascending aorta under free breathing conditions.
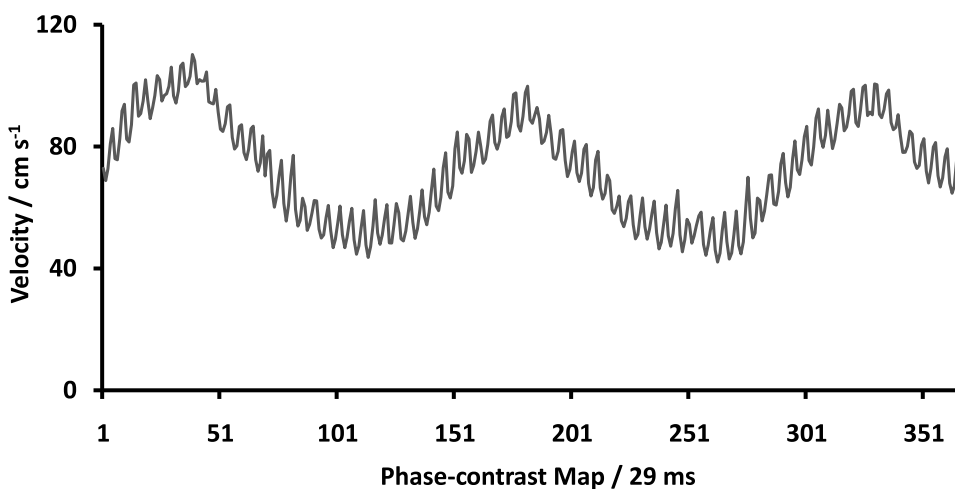
Figure 6.6: Representation of spatial average velocity (phase offset) at the region of ascending aorta obtained from phase-contrast maps without flow gradients. The fluctuations represent the influence of breathing cycle on phase offset values.

6.1.4 Limitations and Outlook

From the in vitro and in vivo studies, it is shown that real-time dual echo PC MRI provided qualitative magnitude images and phase-contrast maps. Constant phase offset, as obtained in in vitro studies, are required for phase offset corrections. In such conditions, a reference phase offset map can be obtained practically at the beginning of the measurement for the correction

of phase-contrast maps. Since the phase offset obtained from in vivo studies is influenced by the breathing cycle, the possibility of using such a reference phase offset map cease to exist. If a reference phase offset map is measured together with each phase-contrast map the temporal resolution prolongs to 2×29 ms which is longer than the single echo measurement (40 ms). However, real-time dual echo PC MRI could be suitable for cerebro-spinal fluid or peripheral circulatory system flow studies, where the influence of respiratory cycle is minimal. Further these region consists of properties like low velocities, less pulsality and uniform surrounding tissue which can be favorable to obtain reference phase offset map. It remains to be seen whether a suitable post-processing strategy may be developed to separate the flow phase from the dynamic phase offset.

6.1.5 Summary

The implementation and results pertaining to radial-based dual-echo PC MRI have been presented in this section. The dual-echo PC MRI along with NLINV reconstruction achieved a temporal resolution of 29 ms per phase-contrast map for an in-plane resolution of 1.8 mm. This was higher compared to the developed real-time PC MRI where temporal resolution of 40 ms was achieved. Since the radial encoding scheme is robust to motion, the current dual-echo PC MRI implementation was able to overcome many problems reported in the previous Cartesian-based studies. Although the implementation of radial encoding based dual-echo PC MRI was successfully developed, it cannot be used for real-time PC MRI due to its critical limitations.

6.2 Multi-directional Velocity Encoding

Motion of spins, according to region of interest and application, can be of complex nature with velocity components extending to different dimensions. This holds true even for the fluid flow in the human body where turbulence is prevalent, for example, in the cardiovascular system. Three dimensional information of velocity and flow components can provide additional information of the concerned system. The current available implementations of 3D PC MRI are based on cine imaging and consume long acquisition time. Hence, they are not normally preferred for quantitative studies in the clinical environment. The previous chapters deal with the development of two-dimensional real-time PC MRI, where velocity is encoded in a single direction to image through plane flow. This technique can be extended to other velocity dimensions to realize real-time multi-directional PC MRI. This section presents the preliminary work performed on the development of real-time multi-directional PC MRI along with the initial results obtained from in vitro and in vivo studies.

6.2.1　3D Velocity Mapping

Different approaches to the 3D phase-contrast imaging have been performed in the past such as performing 2D PC MRI at multiple slice positions in a 3D volume [137] and velocity mapping performed in three dimensions [46, 126, 138]. The latter method of three-dimensional velocity mapping in combination with temporal dimension is called "4D velocity mapping" and is used frequently for the study of multiple diseases [139–142]. Although multi-directional velocity mapping provides flow information in multiple directions, it has a drawback of long scanning times generally around 10 minutes. Moreover, it is performed with ECG and respiratory gating for retrospective reconstructions.

In this thesis, initial studies have been performed to prove the feasibility of extending real-time 2D PC MRI using undersampled radial FLASH and nonlinear inverse reconstruction for real-time 3D velocity mapping. The Figure 6.7 shows the real-time multi-directional PC sequence consisting of velocity encoding in three directions with respect to the image orientation which results in the imaging of in-plane and through-plane flow. The first interval consisted of no velocity encoding in order to obtain reference image for the phase difference calculation. The flow encoding gradients, contrary to the real-time 2D PC MRI sequence [118], were kept independent. No flow compensation gradients were used to acquire the reference image. The sequence is designed to acquire each radial spoke with no flow and flow gradients in interleaved and sequential acquisition schemes as performed for real-time 2D PC MRI. NLINV reconstruction technique, as in Joseph et.al. [118], was further modified to accommodate the reconstruction of real-time multi-directional PC MRI images. A total of four images consisting of one magnitude image and three phase-contrast maps from different directions were displayed after reconstruction. The three phase-contrast maps are combined for velocity representations as shown in equation.

$$\vec{V} = (V_x, V_y, V_z) \tag{6.1}$$

Various methods such as vector representations, streamlines, particle tracing [143–145] are generally used to visualize multi-directional flow. Vector representation was adapted for this thesis because of its simplicity to represent three-dimensional phase information. Development of a visualization software with complex methods such as streamlines and particle tracing is beyond the scope of this thesis.
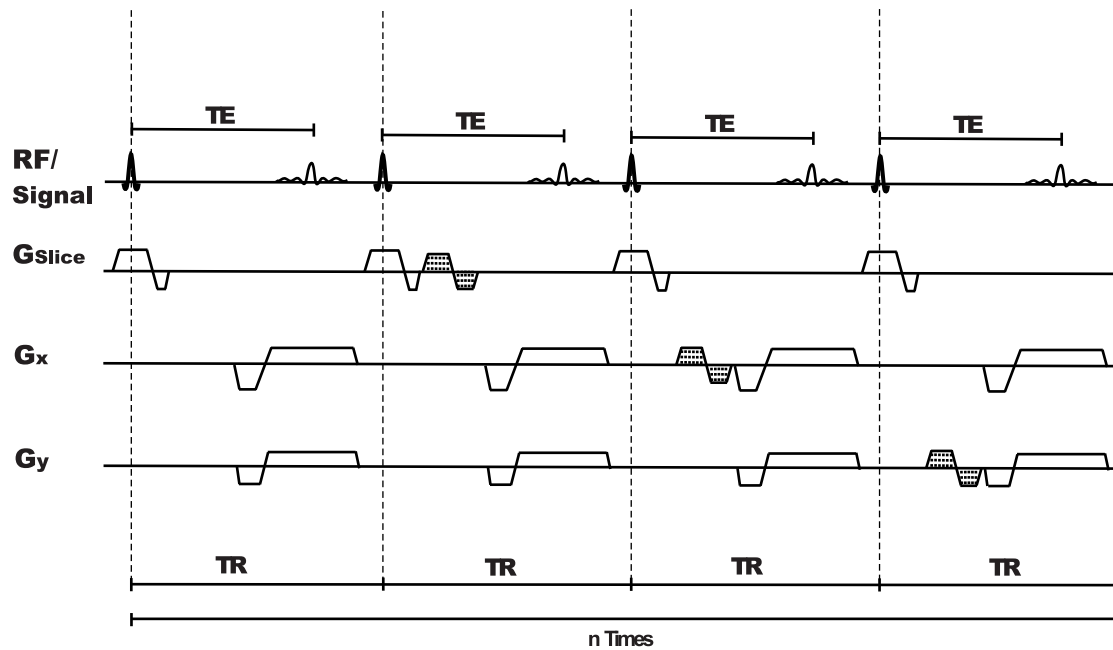
Figure 6.7: Schematic representation of the pulse sequence for radial multi-directional PC MRI. The bipolar gradients (shaded) represent velocity encoding in each physical gradient axis direction.

6.2.2 In Vitro Studies

In vitro studies were performed on tubular phantom with real-time multi-directional PC MRI sequence with a constant flow of around $3\,\mathrm{l\,min^{-1}}$. Tubular phantom was used for in vitro studies as it mimics the flow within the aortic arch. The experiments were performed with FOV 256 mm, base resolution 128 providing an in-plane resolution of 2 mm. The other scan parameters were VENC 150 cm $\mathrm{s^{-1}}$, slice thickness 6 mm, 4×7 spokes, flip angle 10 degrees, TR/TE 4.19 / 3.39 ms and temporal resolution of 112 ms per dataset. Figure 6.8 shows the magnitude and the phase-contrast maps obtained from NLINV reconstruction. The images obtained, as seen from the figure, consisted of high SNR and minimal artifact even at high undersampling. The phase-contrast maps clearly show the flow in the tubes at different directions. The inflow and outflow of water is especially observed in the smaller tube in the head-feet direction (Figure 6.8d).

6.2.3 In Vivo Studies

In vivo studies were performed to qualitatively prove the use of real-time 3D PC MRI for measuring flow values. The scan parameters used for in vitro were also employed for in vivo studies. The imaging time for single measurement was around 5 seconds covering 4 cardiac cycles which produced about 100 magnitude and phase-contrast maps. The sagittal plane of
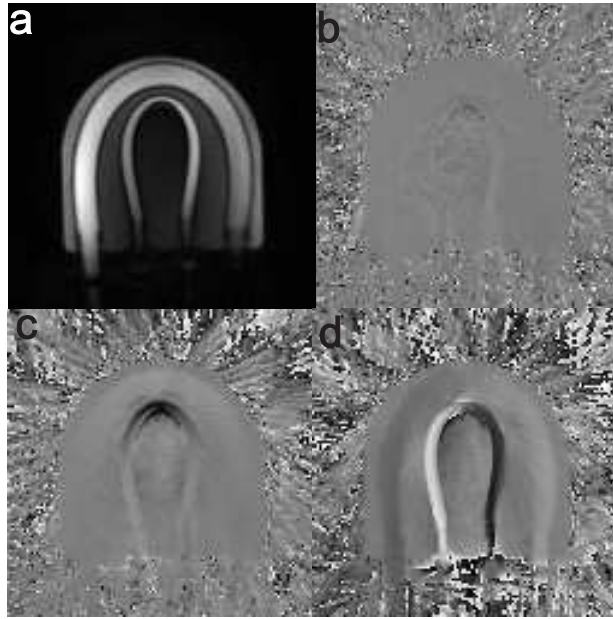
Figure 6.8: (a) Magnitude image and (b, c, d) phase-contrast maps obtained from in vitro studies for different flow directions (b) perpendicular, (c) left-right, (d) head-feet.

the thoracic cavity consisting ascending aorta, aortic arch and descending aorta was used as the imaging position. This image position is ideal for multi-directional flow studies as the flow through the aorta is in different directions and complex in nature. Figure 6.9 shows the results obtained from the real-time multi-directional PC MRI in a systolic phase. The flow in head-feet (d) and left-right (c) direction is clearly observed from the phase-contrast maps. Less or no flow is observed in the perpendicular flow direction (b) to the imaging plane. The vector representation depicted in Figure 6.10 also show the flow velocity and direction within the aorta. The vector representations on magnitude images clearly indicates the motion of flow during the systolic and diastolic phases of the cardiac cycle. The colormap used for the vector representations extends from low (red) to high (yellow) velocities. The complex turbulent flow within the different chambers and blood vessels of the heart is also observed.

6.2.4 Summary

In this section, the development of real-time multi-directional PC MRI using radial FLASH and NLINV reconstruction for three-dimensional velocity quantification is shown. The results from in vitro and in vivo studies, although preliminary, demonstrate the successful implementation of the method. It was also shown that real-time multi-directional PC MRI drastically reduces the scan time to few seconds which is very short compared to cine-based implementations. Moreover, the proposed method provides real-time 3D movies without prospective and retrospective gating. The present implementation consisted of independent flow gradients achieving

Figure 6.9: Sagittal view of the human heart and aorta: (a) magnitude image and (b, c, d) phase-contrast maps obtained for different flow directions (b) perpendicular, (c) left-right, (d) head-feet.
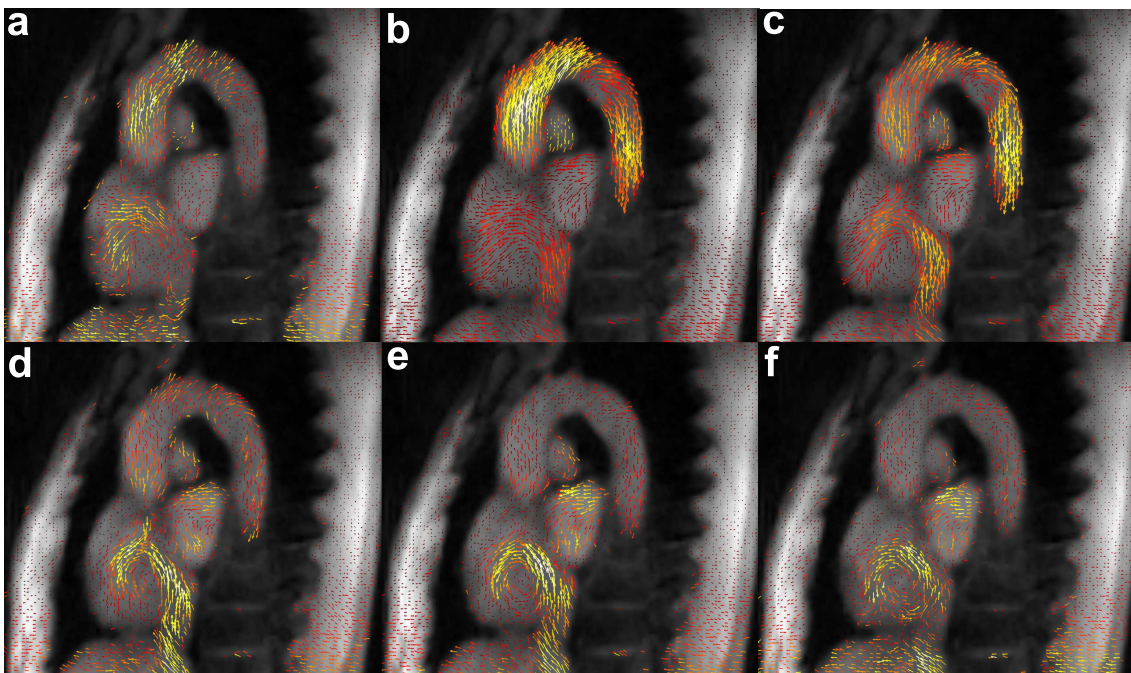
Figure 6.10: Sagittal view of the human heart and aorta: vector representation of the flow in different directions obtained during single cardiac cycle (a) early systole, (b) systole, (c) late systole, (d) early diastole, (e) diastole, (f) late diastole. The colormap of the vector lines extend from red to yellow representing the low and high velocities, respectively. The orientation of the vector line represents the direction of flow.

93

a temporal resolution of 116 ms for the acquisition of three phase-contrast maps without the use of flow compensation gradients. In future, the gradients can be combined or overlapped in order to obtain better temporal resolution in the order of 80 ms. In addition to cardiovascular applications, real-time multi-directional PC MRI can potentially be used to visualize the complex flow in different blood vessels such as carotid arteries, cranial arteries and portal vein.

Chapter 7

Applications of Real-time PC MRI

Over the years MRI has been the preferred technique for morphological and functional imaging. The continued development and acceptance of MRI as an important tool in clinical imaging has been mainly aided by innumerable applications explored in different fields during the past decades. The development of real-time MRI overcame the major drawback of long acquisition time previously associated with MRI. Real-time imaging not only aided in reducing the scan times but also provided additional anatomical and functional information of human body. Various applications of real-time imaging have been explored over the years [59, 66, 76–78, 146, 147]. Similarly the potential of real-time phase-contrast MRI in the field of diagnostic imaging is enormous. This chapter tries to give a view of the wide range of potential real-time PC MRI applications. These applications, explored in the following sections, radiate to different fields of functional and quantitative imaging.

7.1 Quantification of Mild Aortic Valve Insufficiency

The real-time PC MRI, as discussed in previous chapter, provides information on actual physiological variations. Moreover, it can be used for quantitative imaging under disease conditions such as arrhythmia, mild aortic valve insufficiency where irregular heart cycles and flow is encountered respectively. Mild aortic valve insufficiency refers to improper closure of aortic valves. The non closure of the aortic valves leads to chaotic flow patterns in aorta. Moreover reverse flow of blood from aorta to ventricle during the diastolic phase of the cardiac cycle can also be observed. The percentage of back flow of blood is generally used as an important parameter for clinical diagnosis.

Real-time PC MRI was performed on a subject with mild aortic valve insufficiency. The magnitude and phase-contrast maps of systolic phase obtained from ascending aorta are shown in Figure 7.1. The non-laminar flow in ascending aorta is observed from the phase-contrast maps

and flow profile. Turbulence in aorta, due to the improper closure of the aortic valves, induces dephasing of moving spins or mixing of velocities. In the magnitude image, the dark region of blood in the ascending aorta indicates the occurrence of signal loss due to dephasing of spins. These effects are clearly captured by real-time PC MRI due to shorter TE (around 1.84 ms) used. It is widely discussed in the literature that use of shorter TE's aid in reducing the effects of turbulence on quantitative values [36, 102]. Flow parameters were analyzed from aorta and displayed as mean ± SD in Table 7.1. High peak velocity (mean and SD) was observed in ascending aorta. The presence of high standard deviation values indicate the disease condition due to mild aortic valve insufficiency. Average velocity, flow rate and cardiac output were significantly lower in comparison to healthy subjects. On the other hand, the flow parameters obtained from descending aorta were comparable to healthy individuals.

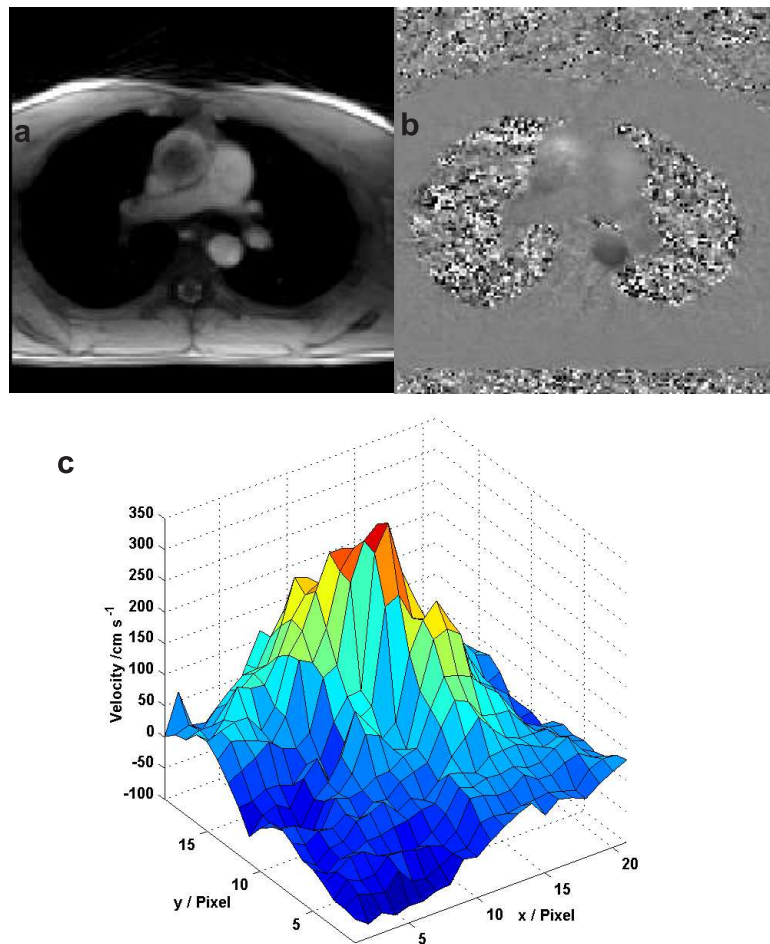Figure 7.1: Transverse view of the human heart at the region of ascending aorta: (a) magnitude image, (b) phase-contrast map and (c) flow profile of blood flow during mild aortic valve insufficiency using real-time PC MRI. The scan parameters were $TR/TE/\alpha = 2.64/1.84$ ms/10°, spatial resolution $1.3 \times 1.3 \times 6$ mm^3, 2×7 spokes and 5 interleaves, VENC 250 cms^{-1}, temporal resolution 37 ms, 27 fps.

Flow Parameters	Ascending Aorta	Descending Aorta
Heart Rate (beats min⁻¹)	53 ± 6	53 ± 6
Peak Velocity (cm s⁻¹)	189 ± 51	110 ± 7
Average Velocity (cm s⁻¹)	7 ± 1	14 ± 1
Flow Rate (cm s⁻¹)	65 ± 8	50 ± 5
Stroke Volume (ml)	74 ± 6	57 ± 4
Volume (l min⁻¹)	3.9	3.0

Table 7.1: Quantitative analysis performed on a subject with mild aortic valve insufficiency, the values are represented as mean $\pm$ standard deviation (SD).

Blood back flow from the aorta to the left ventricle can be clearly seen in Figure 7.2 with the imaging slice positioned below the aortic valves. Magnitude image and phase-contrast maps of the systolic and diastolic phase of the heart cycle obtained with VENC = 400 cm s⁻¹ are displayed. These images separated from each other by around 400 ms show the appearance of regurgitation at the late diastolic phase of the cardiac cycle which is in line with the physiology of mild aortic valve insufficiency. The back flow is observed in both magnitude image and phase-contrast map. Imaging of mild aortic valve insufficiency demonstrates the applicability of real-time PC MRI for disease condition which is frequently observed in clinical environment.
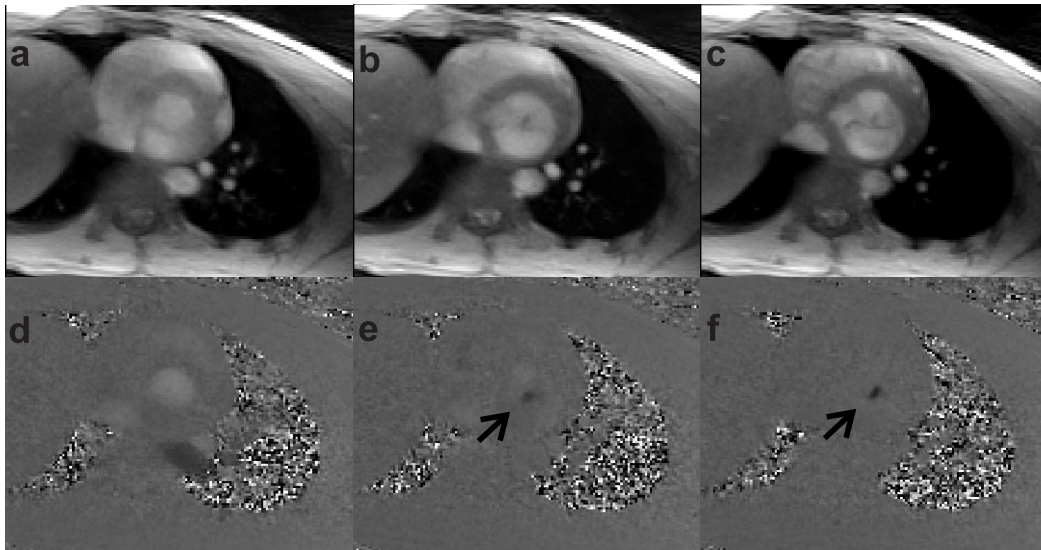

Figure 7.2: Transverse view of the human heart at the region of aortic valve: (a, b, c) magnitude images and (d, e, f) phase-contrast maps of a subject with mild aortic valve insufficiency obtained during systolic phase, diastolic phase and regurgitation. Arrow indicate regurgitation.

7.2   Valsalva Maneuver

A physiological stress test is generally considered to be an early diagnostic indicator for potential diseases. In cardiovascular imaging, these tests can provide valuable information of the condition of heart. The physiological stress test is usually performed in combination with exercises where the heart is made to work under extreme stress conditions in a short span of time. Under stress, the heart reacts differently in order to stabilize or compensate blood circulation to other regions of the body. Such reaction of heart under stress may induce change in flow parameters such as peak velocity, flow rates and heart rate. The observation of these parameters might act as a possible pre-clinical indicator between healthy subjects and patients.

The Valsalva maneuver is a physiological stress test where the effect of increase in intrathoracic pressure on cardiovascular flow parameters for a short time span is studied [148, 149]. Echocardiography is the most preferred technique to study the flow parameters obtained from Valsalva maneuver. The drawbacks of echocardiography are high operator dependence and inability to analyze multiple blood vessels simultaneously. These drawbacks are easily overcome by MRI which provides standardized and consistent results. However, stress tests such as Valsalva maneuver, where extreme intercardiac variation of flow parameters exists, cannot be performed with Cine PC MRI. Although imaging of Valsalva maneuver through PC MRI was experimented previously [150, 151], these studies were performed with poor spatial and temporal resolution and lacked extensive quantitative analysis of the parameters. In this thesis, the effects on flow parameters through valsalva maneuver were studied in detail for ascending aorta and superior vena cava while maintaining high spatial and temporal resolution.

Studies were conducted on normal healthy subjects (n=20) under heterogeneous ages groups using real-time PC MRI. The duration of the experiment was 40 s which was divided in to different phases consisting of 1) preparation phase of 10 s, 2) maneuver phase of 10 s and 3) rest phase of 20 s. Each measurement produced about 1000 phase-contrast maps and magnitude images which were quantitatively analyzed for ascending aorta and superior vena cava. The subjects were instructed to maintain an intrathoracic pressure of about 40 mmHg during the maneuver phase of 10 s. Real-time visual feedback of pressure readings was given to subjects as a control parameter. ECG triggering was used to obtain time stamps which were used to sort real-time images according to different cardiac cycles.

The magnitude images and the phase-contrast maps obtained during different phases of Valsalva maneuver are displayed in Figure 7.3. Differences between magnitude and phase-contrast maps can be observed visually for different maneuver phases of the experiment. The variations
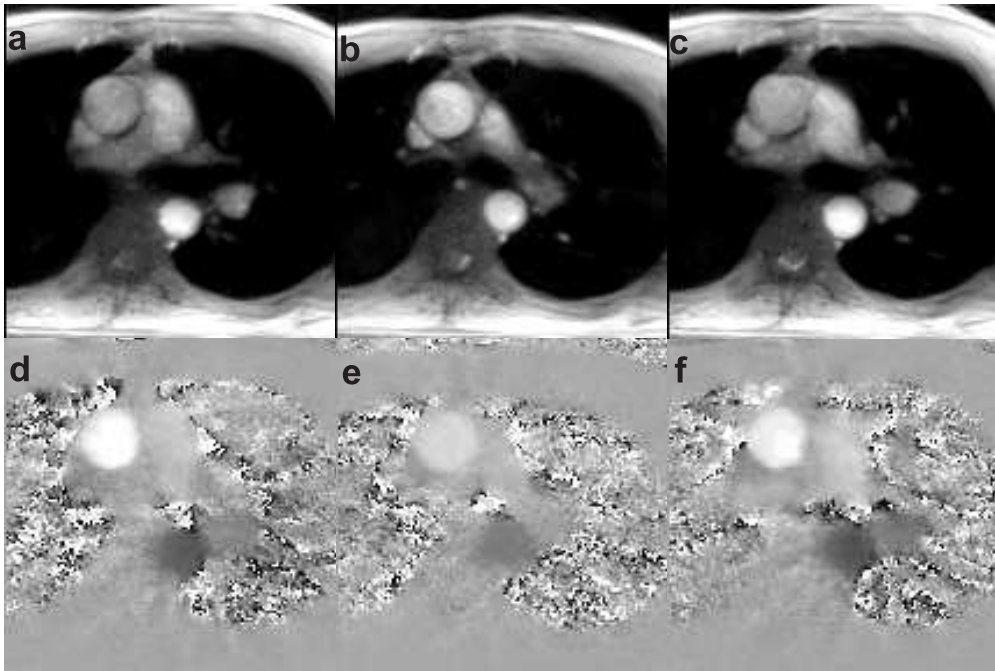
Figure 7.3: Transverse view of the human heart at the region of ascending aorta: (a, b, c) magnitude images and (d, e, f) phase-contrast maps obtained during (a, d) preparation, (b, e) maneuver and (c, f) resting phase. The scan parameters were VENC 200 cms^{-1}, TR/TE/α 2.86 ms/1.93 ms/10°, in-plane resolution 1.3 mm, slice thickness 6 mm, FOV 192 mm, 2×7 spokes, 40 ms temporal resolution.

in flow parameters of ascending aorta for different phases of the maneuver are shown in Figure 7.4. The velocity represented indicates the spatial average per phase-contrast map over a region of interest. The flow parameters such as velocity and stroke volume is reduced by a factor of 2 during the maneuver phase which recovers to normal values during the rest phase. Fluctuations in flow parameters during the preparation and resting phase are mainly due to the influence of respiration. At the start of the maneuver the velocity and stroke volume initially increases for few heart cycles before descending to lower values. After the maneuver phase, circulation of blood in lungs and other regions have a recovery time to bring the cardiac output to the levels of pre-maneuver phase. Further, the increase in heart rate during the maneuver phase can also be observed which stabilizes after the heart has fully recovered. During the maneuver phase the cardiovascular system increases the heart rate to compensate for the decrease in the volume of blood received by the others parts of the body.

Changes in flow parameters during the maneuver phase can also be observed in superior vena cava (Figure 7.5). Velocity and flow profiles observed in superior vena cava are similar to ascending aorta. The velocity and stroke volume decreases strongly and rapidly even to negative values during the maneuver phase. Contrary to ascending aorta, superior vena cava reacts
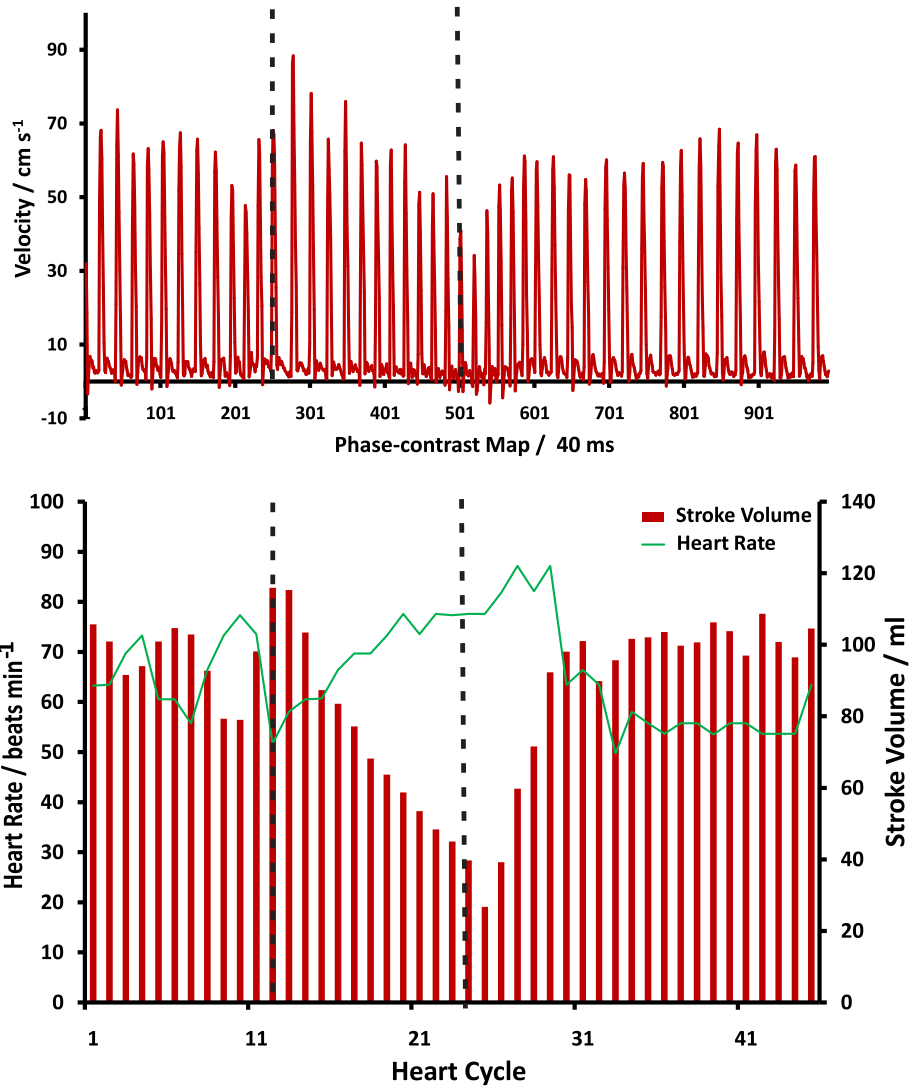
Figure 7.4: Quantitative flow parameters obtained in ascending aorta during preparation, maneuver and relaxation phase of the Valsalva maneuver. (Top) Spatial average of velocities represented over time. (Bottom) Stroke volume per heartbeat in red and heart rate in green obtained over heart cycles. Vertical lines indicate different phases of the measurement.

rapidly to high intrathoracic pressure by decreasing the velocity and stroke volume to minimum as observed at the start of the maneuver phase. Stroke volumes as high as 90 ml are observed at the beginning the relaxation phase which occurs to stabilize the flow to the heart. It is assumed, the sudden variations in velocity and flow profiles in superior vena cava occurs due to reduced vessel wall elasticity.
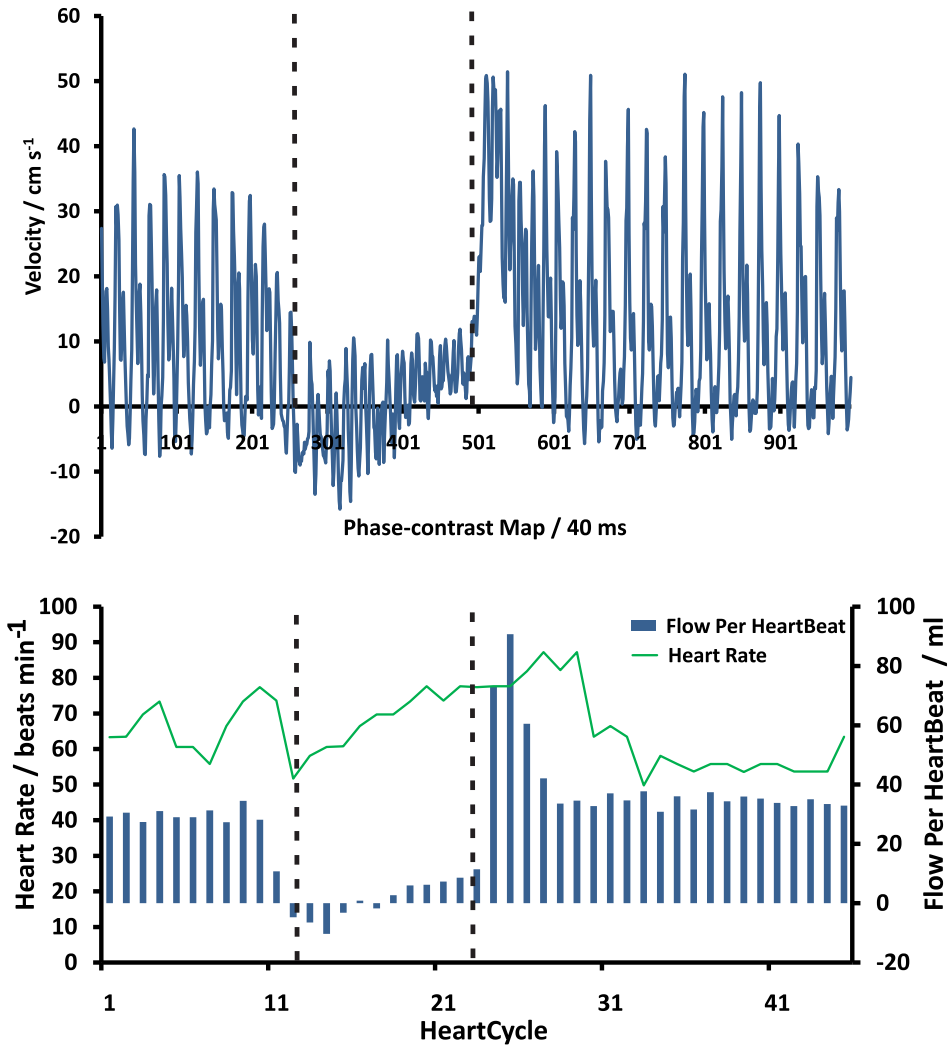
Figure 7.5: Quantitative flow parameters obtained in superior vena cava during preparation, maneuver and relaxation phase of the Valsalva maneuver. (Top) Spatial average of velocities represented over time. (Bottom) Stroke volume per heartbeat in blue and heart rate in green obtained over heart cycles. Vertical lines indicate different phases of the measurement.

This study shows the application of real-time PC MRI to obtain qualitative and quantitative flow information from complex maneuvers. The high temporal resolution of real-time PC MRI makes it possible to observe sudden variations in physiological flow parameters during exercise, stress tests or complex maneuvers. Also the advantage of real-time PC MRI over Cine in

imaging complex intercardiac cycle variations is demonstrated. Further these results from Valsalva maneuver indicate the use of real-time PC MRI on patients under disease conditions such as arrhythmia where high degree of intercardiac heart rate variability is present. It is presumed that complex maneuvers like Valsalva can be used as early diagnostic tool to identify potential cardiac insufficiency patients. Therefore real-time PC MRI can contribute immensely in the clinical environment.

7.3 Peripheral Circulation

The application of real time PC MRI for cardiovascular imaging has been discussed in the previous sections. This technique can also be extended to peripheral circulatory system which consists of arteries and veins of small diameters. The flow in the arteries is pulsatile in nature due to its elastic properties. The veins, due to its minimal elastic properties, consist of valves to prevent back flow. Exact quantification of flow velocities in deep veins and arteries of lower limbs is challenging as the flow velocities present are lesser than 10 cm s^{-1}and 30 cm s^{-1}, respectively. Further, the associated blood vessels have small vessel diameters which makes the imaging and quantitative analysis difficult.

Arterial Flow

Peripheral circulation system of lower limbs were analyzed with the region of interest around the calf muscles. This region consisted of deep veins and arteries such as anterior tibial artery, peroneal artery and posterior tibial artery. Real-time PC MRI was performed in this region with an in-plane resolution of 1.3 mm and slice thickness of 6 mm. Sensitivity to low velocities in arteries was increased by adjusting the VENC to 60 cm s^{-1} which led to TR/TE/α 3.54 ms/2.65 ms/10° and temporal resolution of 50 ms. The experiment was performed at resting state of the lower limbs. The magnitude image and phase-contrast map obtained are displayed in Figure 7.6. Anterior tibial artery, peroneal artery and posterior tibial artery can be clearly observed from the magnitude image and phase-contrast map. In phase-contrast map, the arteries are represented in black region as the subject was placed in the feet first and supine position inside the scanner. It can be noticed that deep veins are not observed in the images. The possible reason to non-appearance of deep veins is either because of flow with very low velocities or usage of higher VENC. The quantitative analysis of three arteries were performed and spatially averaged velocity per phase-contrast map are displayed as shown in Figure 7.7. The spatially averaged velocities obtained from the peripheral arteries were around 9 cm s^{-1}. On a closer analysis, these arteries also display the pulsatile flow nature as observed in cardiovascular blood vessels.

Figure 7.6: Magnitude image (left) and phase-contrast map (right) of peripheral arterial flow obtained from lower limbs at the region of the calf muscles using real-time PC MRI. Region of interests include anterior tibial artery (green), peroneal artery (blue) and posterior tibial artery (red).
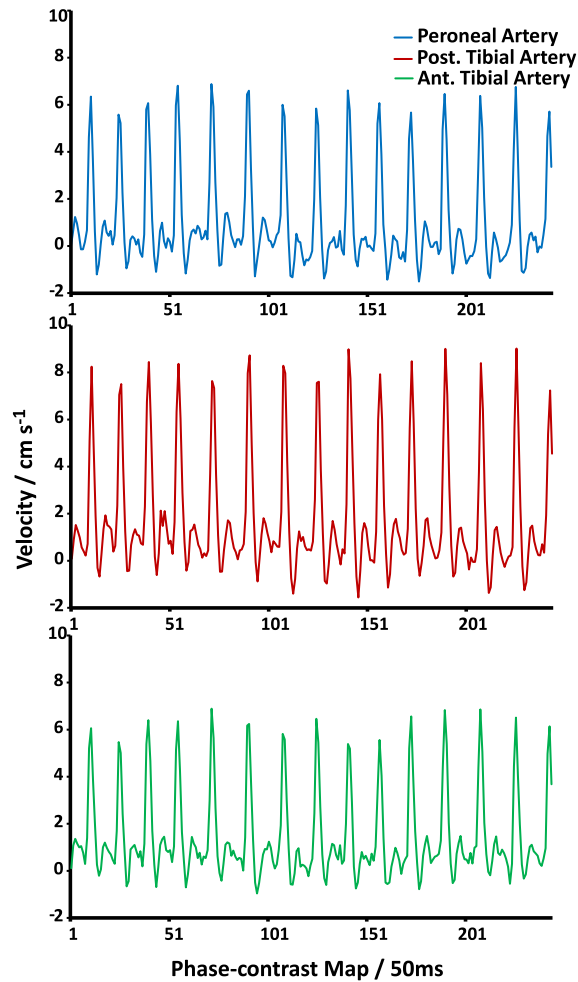
Figure 7.7: Flow parameters representing peripheral arterial flow obtained from lower limbs at the region of the calf muscles using real-time PC MRI. Region of interests include anterior tibial artery (green), peroneal artery (blue) and posterior tibial artery (red).

Venous Flow

The flow in the veins is mainly due to the pressure gradient created between the heart and cap-
illaries and is additionally assisted by other factors such as heart rate, respiration, contraction
of the surrounding muscles [152–154]. MR has been previously used in the field of venography
to image the deep veins in the body [155–157] but these studies could obtain only anatomical
images and relied on doppler ultrasound for quantitative analysis of flow and velocity. The
applicability of real-time phase-contrast sequence to understand the properties of deep veins
would be of great interest. Venous flow studies conducted recently [158, 159] rely on gated flow
sequences or sliding window reconstructions. The real-time PC MRI performed for peripheral
circulation system at resting state, as demonstrated previously, was only able to detect the
pulsatile flow in arteries. However, the deep veins such as anterior tibial, fibular and posterior
tibial were observed when flexion and extension of the foot was performed. This alternating
flexion and extension of the foot results in contraction of leg muscles which subsequently helps
in imaging venous flow. The venous flow due to muscle contractions can also be verified from
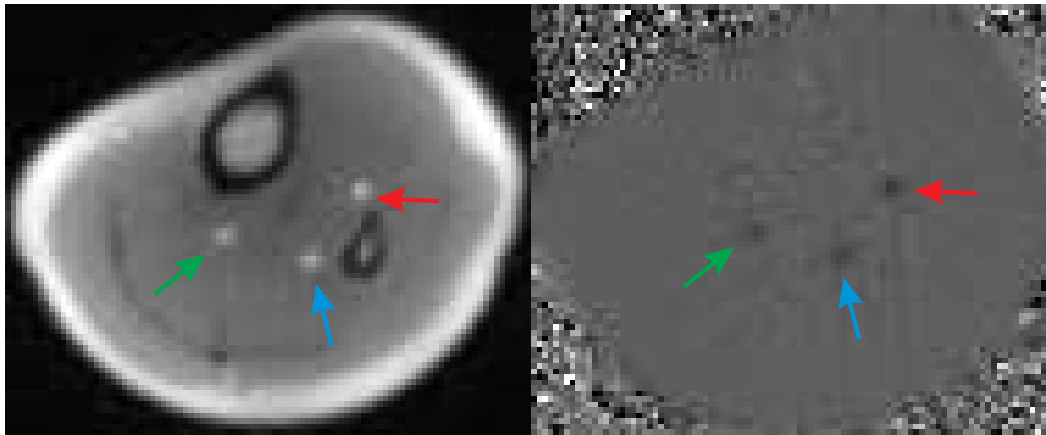the spatial averaged velocities shown in Figure 7.9.
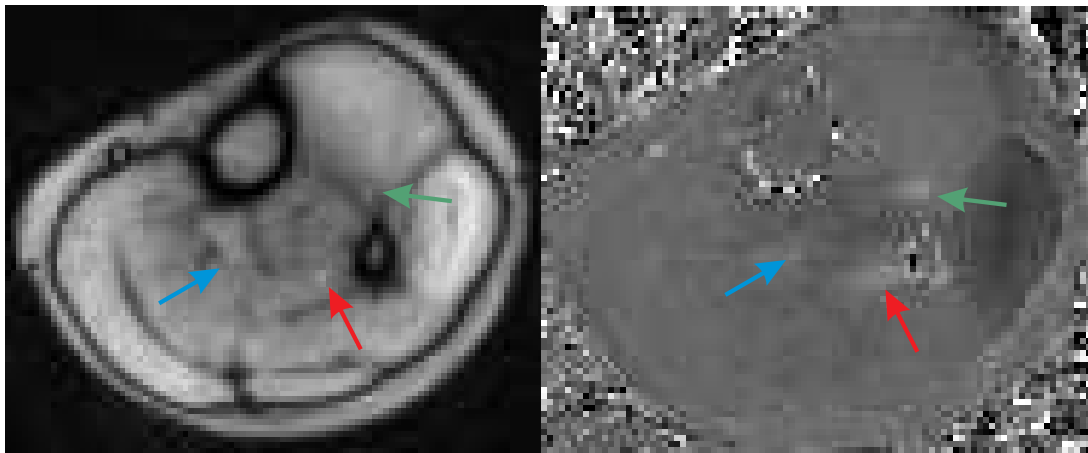
Figure 7.8: Magnitude image (left) and phase-contrast map (right) of peripheral venous flow
obtained from lower limbs at the region of the calf muscles using real-time PC MRI during
flexion and extension of the foot. Region of interests include anterior tibial vein (blue), fibular
vein (red) and posterior tibial vein (green).

In future, the real-time imaging of peripheral circulatory system should be supported with
multiple tasks to understand the physiology and hemodynamics of peripheral blood flow. The
specific knowledge of hemodynamics will surely aid in targeting early diagnosis of specific
diseases. For example, the formation of varicose veins is a topic of great interest about peripheral
circulatory system where blood is accumulated in the lower limbs due to the non-functioning
of valves which are present in the veins [160, 161]. Past studies using MRI concentrated on
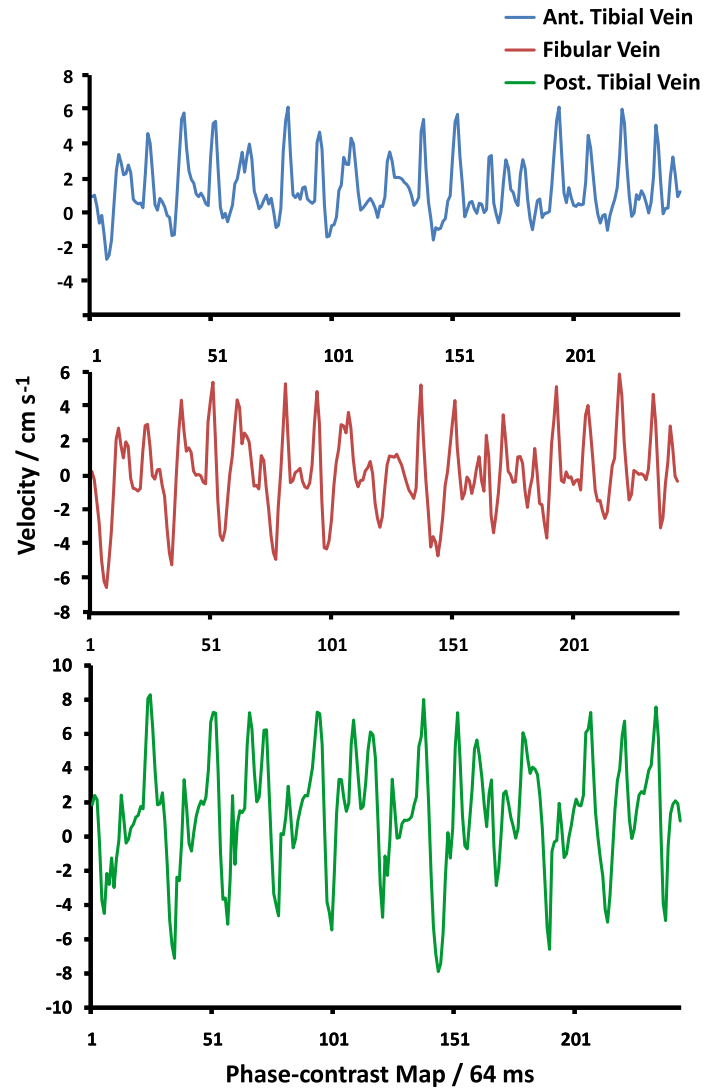
Figure 7.9: Flow parameters representing peripheral venous flow obtained from lower limbs at the region of the calf muscles using real-time PC MRI. Region of interests include anterior tibial vein (blue), fibular vein (red) and posterior tibial vein (green).

anatomical imaging of varicose veins from different regions of the body [162,163]. It is assumed that flow information using real-time PC MRI can be used as a tool for the early diagnosis of thrombosis in deep veins.

7.4   Skeletal Muscle Motion

Skeletal muscles are important part of the human body and complete the framework of the skeletal systems. The coordinated effort of different muscles at different regions leads to movement of the body. Studies on musculo-skeletal system and its modeling helps in understanding the bio-mechanics of the muscles [164–166] which can be applied in the fields of physiotherapy (preventive and post operative), sports medicine and training [167]. Pathological conditions can induce uncoordinated functioning of muscles such as cerebral palsy [168], muscle spasticity [169], static muscle contractures [170], limb abnormalities [171]. PC MRI can be used to understand and study the biomechanics of the muscles. Cine phase-contrast imaging was used for these studies [172–174]. Further studies on skeletal muscles and its applications using the PC MRI have been reported in the past years [164, 175–178]. The problem of using cine phase-contrast imaging for skeletal muscle velocity are as follows 1) the image quality decreases considerably when non-accurate and uncoordinated repetitions are performed 2) Prolonged scan time can create fatigue of the muscles involved in the tasks performed 3) patients suffering from musculo-skeletal diseases are uncomfortable to perform tasks for prolonged scan times. These drawbacks are circumvented by real-time imaging which provides access to quantitative information along with comfort to patients [179]. Experiments were performed to demonstrate the use of real-time PC MRI for the quantification of musculo-skeletal system. The through-plane motion of the lower limb was imaged with a region of interest around the calf muscles. The muscles imaged and quantified were gastrocnemius-medial, tibialis anterior and fibularis longus. The subject was asked to perform continuous flexion and extension of the foot during the measurement. Real-time PC MRI images were obtained with spatial resolution $1.3 \times 1.3 \times 6$ mm^3, TR/TE/α 4.58/3.69 ms/10°, VENC 25 cm s^{-1}, FOV 192 mm, 7 spokes, temporal resolution of 64 ms.

The maximum spatially averaged velocity was analyzed and plotted for different muscles as shown in Figure 7.11. It is observed that the three muscles gastronemeus-medial, fibularis longus and tibialis anterior act simultaneously. However, tibialis anterior acts opposite to gastrocnemius-medial and fibularis longus. These muscles act similarly and oppositely to maintain the balance of the lower limb. These results can also be observed from the phase-contrast maps displayed in Figure 7.10. Further, the mean and standard deviation of the peak velocity from gastrocnemius-medial, fibularis longus and tibialis anterior was 6.87±1.4 cm s^{-1}, 6.85±0.9 cm s^{-1}, and 7.31 ± 0.8 cm s^{-1}, respectively. From this study it has been demonstrated that
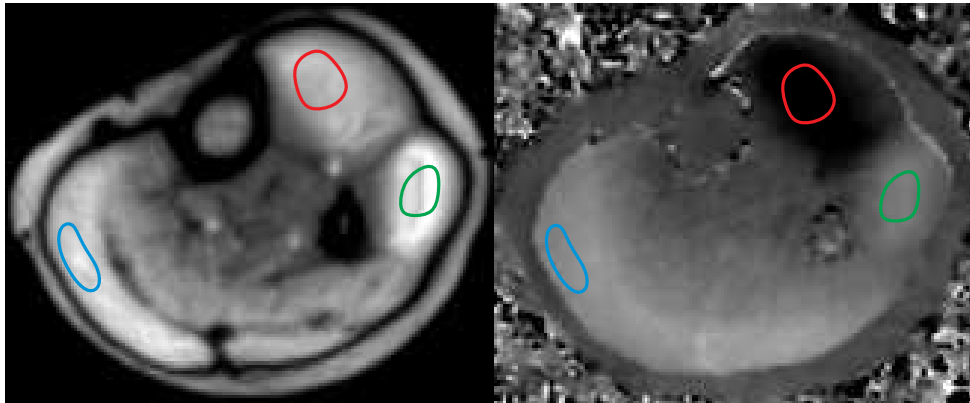
Figure 7.10: Magnitude image (left) and phase-contrast map (right) depicting the skeletal muscle motion using real-time PC MRI. Region of interests include gastroncnemius-medial (blue), tibialis anterior (red) and fibularis longus (green) of the lower limb.

Figure 7.11: The quantitative analysis of spatially averaged velocity of the skeletal muscles. Region of interests include gastrocnemius-medial (blue), tibialis anterior (red) and fibularis longus (green) of the lower limb.

biomechanics of skeletal muscles can be imaged and studied using real-time PC MRI. Similar studies in future can be used to study the functioning of other muscles of the body which aid in creating a complete individual specific musculo-skeletal model incorporating the muscle dynamics. Such model can also be used for pre-operative planning and designing of prosthesis. In addition, this study proves that real-time PC MRI can be used to study all kinds of motion involving moving spins.

7.5   Swallowing

Esophagus, commonly known as 'food pipe', is an anatomical structure which connects the mouth and stomach. It provides the passage for the food to reach the stomach. Esophagus is located in the thoracic cavity behind the heart, lungs along with ascending aorta and in-front of the vertebral column. The esophagus abnormalities in most patients are due to the gastromotor disorders [180] and gastroesophageal reflux disease (GERD) [181, 182]. The common methods to measure the esophageal disorders are pH-metry [183], manometry [181] and videofluoroscopy. While pH-metry and manometry are used for evaluation for greater extent by clinicians, they induce patient discomfort due to long measurement times and invasive procedure. Videofluoroscopy allows for the visualization and assessment of oral, pharyngeal and esophageal spaces simultaneously from the images, but is associated with the administration of doses of 0.76-1.3 mSv of ionizing radiation [184]. In the past, various MRI techniques were employed to measure the swallowing function and gastroesophageal junction [185–187]. Dynamic MRI studies have also been conducted to study esophagus function [188, 189] but with low temporal resolutions. Recently Zhang et al. [77] successfully employed undersampled radial FLASH and nonlinear inversion reconstruction with high spatial and temporal resolutions for the real-time study of swallowing function. Although these studies dealt with swallowing and esophagus function, phase-contrast MRI was never used for the quantitative assessment of the flow in esophagus. The purpose of this study was to demonstrate and discuss the preliminary results obtained from real-time PC MRI on flow through the esophagus.

The experiments were performed with real-time PC MRI at the region of the sphincter into the stomach. All measurements were performed with 10 ml bolus of pineapple juice as it provides natural T_1 contrast in MRI due to the presence of manganese. The real-time PC MRI was performed on 10 normal subjects with an in-plane resolution of 2 mm, slice thickness of 8 mm, VENC 60 cm s^{-1} providing temporal resolution of 50 ms. Figure 7.12 shows the magnitude and phase-contrast maps obtained from the flow inside esophagus at the region of sphincter muscle. As seen from the images the area of the flow is very small due to the narrow opening of the sphincter muscle to the stomach.
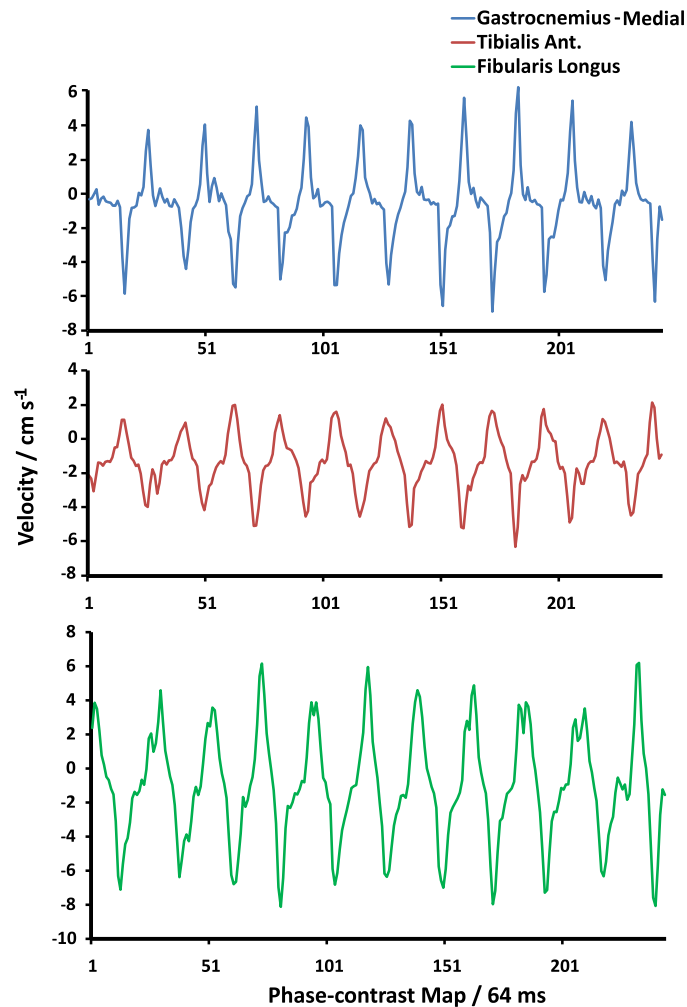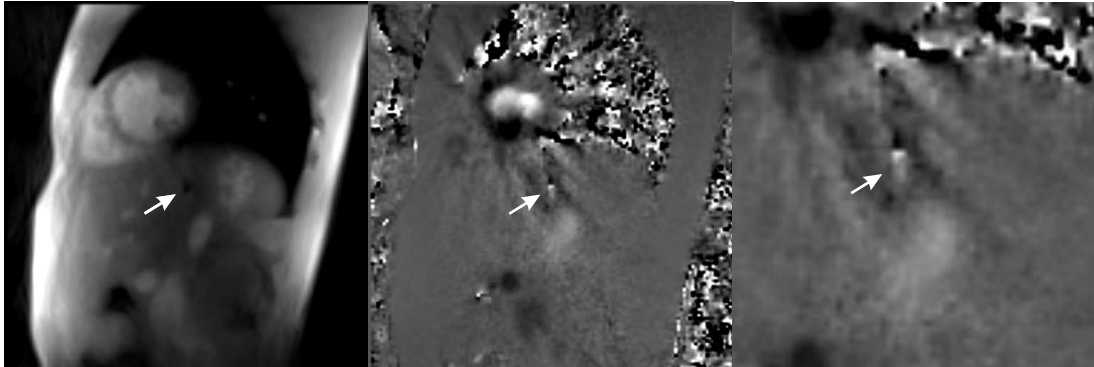
Figure 7.12: Magnitude image and phase-contrast maps depicting the real-time PC MRI of esophagus at the region of the sphincter. The arrow indicates the passage of bolus through the sphincter muscles in magnitude image and the velocity of bolus flow in phase-contrast map.

The quantitative analysis of the flow around the sphincter muscles using real-time PC MRI is represented in Figure 7.13. The peak velocity and the spatial average velocity obtained from flow at sphincter muscle was around 27 and 7 cm s^{-1}, respectively. It can be also inferred from the graph that the entire bolus is transferred from sphincter to the stomach in around 1.5 s. The maximum of the peak velocity represents the involuntary opening of sphincter muscles to the bolus. However, the number of instances of the opening of sphincter muscles for the passage of bolus can vary between subjects.

Figure 7.13: Quantitative analysis of flow parameters such as spatially averaged velocity and peak velocity at the region of sphincter. The peaks represent the opening of the sphincter muscles for bolus outflow.

The flow in the esophagus is mainly caused by the peristaltic movement of the inner muscles of the esophagus which is different from the pulsatile laminar flow pattern of ascending aorta. This can pose several challenges for quantitative analysis such as 1) small reg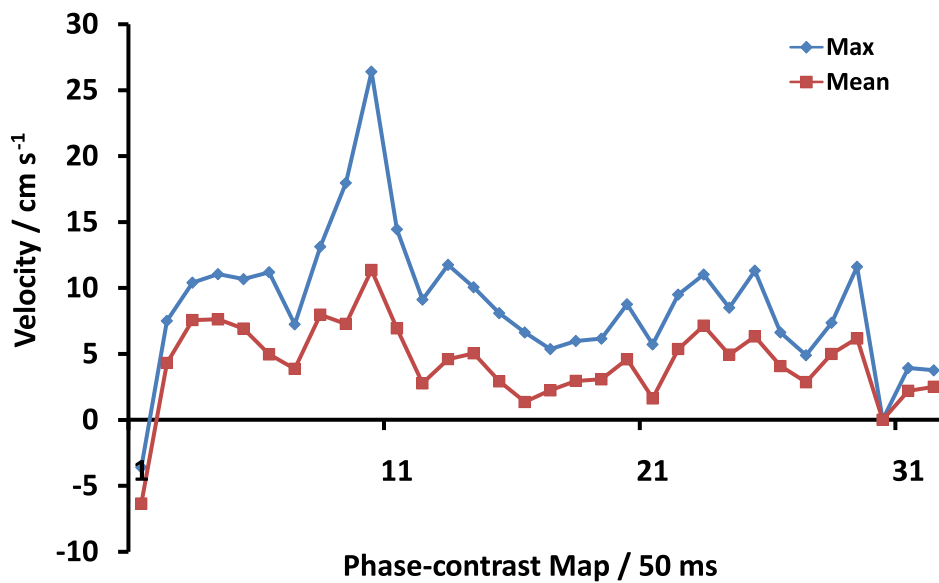ion of interest covering few pixels due to complex peristaltic flow 2) in some subjects some region of the lumen was filled with air which induces noise in phase-contrast maps 3) inter-subject variability over the process of flow in esophagus can be prominent in some instances. Nevertheless, this is the first demonstration on the application of real-time PC MRI in understanding the esophagus flow. In future, improvements can be made to the challenges encountered by real-time PC MRI for the analysis esophagus function.

7.6   Summary

Applications of real-time PC MRI, as demonstrated in this chapter, not only pertain to quantitative imaging of cardiovascular blood flow but also to other fields of research. The ability to capture actual physiological variations was effectively demonstrated from Valsalva maneuver where rapid changes in flow parameters and heart rate were observed. These results cannot be attained by cine PC MRI where images of synthetic cardiac cycle are obtained. Further, these results on Valsalva maneuver and mild aortic valve insufficiency also exhibit the potential of real-time PC MRI for imaging disease conditions such as arrhythmias where inconsistent heart rates are observed. This chapter also presented the first demonstration of the flow in esophagus through real-time PC MRI. Although the detection of esophagus flow faces several challenges, future improvements to the technique would aid in clinical acceptance. Real-time PC MRI could provide additional information regarding arterial and venous flow of the peripheral circulation system which may in future act as a diagnostic tool of diseases of deep veins such as thrombosis. Imaging and quantification of skeletal muscle motion was shown with real-time PC MRI which can potentially be used for musculo-skeletal modeling and understanding bio-mechanics. From the diverse applications presented in this chapter, it can be inferred that real-time PC MRI could be a great diagnostic tool to create a functional model of physiological processes associated with moving spins.

Chapter 8

Summary and Outlook

The development of a robust and quantitatively reliable real-time MRI technique for imaging of moving spins was the major goal of this thesis. For this purpose, phase-contrast flow MRI was the method of choice as it provides both qualitative and quantitative information. Real-time phase-contrast MRI as developed in this work offers valuable new insights into cardiovascular blood flow through access to individual cardiac cycles, monitoring of physiological variations of functional parameters from heartbeat to heartbeat, and insensitivity to the occurrence of irregular cardiac cycles - none of which can be achieved by standard Cine MRI techniques. Although previous attempts to real-time phase-contrast MRI have been reported [132,150,190–194], most implementations had to sacrifice on spatial resolution to achieve high temporal resolution. In this work, a temporal resolution of 40 ms was achieved while maintaining sufficiently high spatial resolution of $1.3 \times 1.3 \times 6$ mm^3.

The first part of this thesis compared different acquisition schemes such as Cartesian and radial sampling schemes. Radial schemes were found to be more robust to pronounced undersampling which is beneficial for real-time imaging. The oversampling of k-space center by radial encoding makes it moderately tolerant to motion. This aspect was advantageous for regions with involuntary motions such as the cardiovascular system, thorax and upper abdomen. In general, highly undersampled radial acquisitions were combined with a modified regularized NLINV reconstruction method. In anatomical real-time MRI the use of a temporal median filter along with interleaved radial acquisitions commonly reduces the amount of residual streaking artifacts from extreme undersampling. For real-time phase-contrast MRI, however, the application of this filter was restricted to magnitude images in order to preserve the temporal fidelity and true flow resolution of the individual phase-contrast maps. Streaking artifacts were observed in phase-contrast maps especially at cardiac phases of high flow velocity such as during early systole. They generally occur outside the vascular region and therefore do not corrupt quantitative evaluations.

With respect to flow encoding, two gradient modes with bipolar gradients were developed termed zero-max (i.e., with and without a flow gradient) and min-max (i.e. with two sign-opposed gradients). While phantom validations revealed no differences between both gradient modes, the zero-max version was used for in vivo real-time phase-contrast MRI studies as it provides shorter echo times. Flow compensation gradients were introduced in the slice direction to remove motion artifacts, but found not necessary in the two read directions. Short echo times were ensured by gradient overlap along all axes. Two variants, i.e. a sequential and interleaved mode for flow encoding, were developed for real-time phase-contrast MRI. In vivo studies of the ascending aorta showed slight differences in the mean velocity especially at late systolic phases of the cardiac cycle. The sequential variant was chosen as the preferred method because of its better temporal definition (20 ms) of the flow-encoded acquisition, and because it provided less corrupted ECG signals which are usually recorded as time stamps for more convenient parametric analyses.

Further extensions of the real-time phase-contrast MRI method concentrated on the use of two sequential gradient echoes for further speed. In comparison to previous dual-echo phase-contrast studies with Cartesian sampling, the radial sequence developed here was able to remove visible motion artifacts. However, the occurrence of differential phase offsets between the two echoes due to respiratory motion resulted in a drawback which makes the approach not viable for real-time applications. Nevertheless, dual-echo phase-contrast flow MRI may be recommended for scenarios without motion. Preliminary work on the encoding of multi-directional flow at high temporal resolution was also demonstrated. Current implementations offer 110 ms acquisition times per section, while ECG-gated Cine studies of 4D flow MRI usually last for up to 30 minutes.

Foreseeable technical advances are manifold and, for example, include new methods to remove residual streaking artifacts for high-velocity flow situations. A possible solution may stem from refined nonlinear inverse reconstructions that rely on an aggregated motion estimation [195]. A simple technique to enhance the temporal resolution by a factor of two would be to sequentially share the two images with different velocity encodings by a sliding-window reconstruction of phase-contrast maps [196]. An even better though computationally demanding development would be the combination of complementary sets of spokes from the two flow-encoded acquisitions in a direct model-based reconstruction of phase-contrast maps. And finally, the use of low VENC values for flow encoding, which is preferable for enhanced sensitivity, will become possible if robust phase unwrapping methods are available that exploit the pronounced temporal continuity of a real-time phase-contrast MRI acquisition.

In summary, this thesis presents the successful development of a real-time phase-contrast MRI method at high spatiotemporal resolution. It offers advantageous applications for quantitative studies of human blood flow and moving spins in general. Apart from providing a huge mine of new diagnostic information at improved patient comfort, this technique promises shorter examination times. Its translation into the clinical environment warrants further validation in extensive patient studies, but may be a diagnostically fruitful and economically viable enterprise. In conclusion, this thesis significantly contributed to the advancement of flow MRI.

Bibliography

[1] P.C. Lauterbur. Image formation by induced local interactions: examples employing nuclear magnetic resonance. *Nature*, 242:190–191, 1973.

[2] F. Bloch. Nuclear induction. *Phys. Rev.*, 70:460–474, 1946.

[3] E.M Purcell, H.C. Torrey, and R.V. Pound. Resonance absorption by nuclear magnetic moments in solid. *Phys. Rev.*, 69:37–38, 1946.

[4] Z.P. Liang and P.C. Lauterbur. *Principles of magnetic resoance imaging: a signal perspective*. IEEE press series in biomedical engineering. SPIE Optical Engineering Press, 2000.

[5] E.M. Haacke, R.W. Brown, M.R. Thompson, and R. Venkatesan. *Magnetic resonance imaging: physical principles and sequence design*. Wiley-Liss NewYork, 1999.

[6] E.L. Hahn. Spin echoes. *Phys. Rev.*, 80:580, 1950.

[7] D.B. Plewes and W. Kucharczyk. Physics of mri: a primer. *JMRI*, 35:1038–1054, 2012.

[8] G.H. Glover and J.M. Pauly. Projection reconstruction techniques for reduction of motion effects in MRI. *MRM*, 28:275–289, 1992.

[9] C.B. Ahn, J.H. Kim, and Z.H. Cho. High-speed spiral-scan echo planar NMR imaging. *IEEE Trans. Med. Imaging*, 5:2–7, 1986.

[10] D.C. Noll, J.D. Cohen, C.H. Meyer, and W. Schneider. Spiral k-space MR imaging of cortical activation. *JMRI*, 5:49–56, 1995.

[11] K.T. Block and J. Frahm. Spiral imaging: a critical appraisal. *JMRI*, 21:657–668, 2005.

[12] M. Katoh, E. Spuentrup, A. Buecker, W.J. Manning, R.W. Guenther, and R.M. Botnar. MR coronary vessel wall imaging: Comparison between radial and spiral k-space sampling. *JMRI*, 23:757–762, 2006.

[13] P. Mansfield. Multi-planar imaging formation using NMR spin-echoes. *Journal of Physics C: Solid State Physics*, 10:L55–L58, 1977.

[14] P. Mansfield and I Pykett. Biological and medical imaging by NMR. *JMR*, 29:355–373, 1978.

[15] R.R. Edelman, P. Wielopolski, and F. Schmitt. Echo-planar MR imaging. *Radiology*, 192:600–612, 1994.

[16] H. Zeng and R.T. Constable. Image distortion correction in EPI: comparison of field mapping with point spread function mapping. *MRM*, 48:137–146, 2002.

[17] M. Bernstein, K. King, and X. Zhou. *Handbook of MRI pulse sequences*. Academic Press, 2004.

[18] J.D. OSullivan. A fast sinc function gridding algorithm for Fourier inversion in computer tomography. *IEEE Trans. Med. Imaging*, 4:200–207, 1985.

[19] E.L. Hahn and D.E. Maxwell. Spin echo measurements of nuclear spin coupling in molecules. *Phys. Rev.*, 88:1070, 1952.

[20] A. Haase, J. Frahm, D. Matthaei, W. Hanicke, and K.D. Merboldt. FLASH imaging. rapid NMR imaging using low flip-angle pulses. *JMR*, 67:258–266, 1986.

[21] J. Frahm, A. Haase, and D. Matthaei. Rapid NMR imaging of dynamic processes using the FLASH technique. *MRM*, 3:321–327, 1986.

[22] G. Suryan. Nuclear resonance in flowing liquids. *Proc. Indian Acad. Sci. A*, 33:107–111, 1951.

[23] H.Y. Carr and E.M Purcell. Effects of diffusion on free precession in nuclear magnetic resonance. *Phys. Rev.*, 94:630, 1954.

[24] J.R. Singer. Blood flow rates by nuclear magnetic resonance measurements. *Science*, 130:1652–1653, 1959.

[25] J.R Singer. Flow rates using nuclear or electron paramagnetic resonance techniques with applications to biological and chemical processes. *J. Appl. Phys.*, 31:125–127, 1960.

[26] O.C. Morse and J.R Singer. Blood velocity measurements in intact subjects. *Science*, 170:440–441, 1970.

[27] T. Grover and J.R Singer. NMR spin-echo flow measurements. *J. Appl. Phys.*, 42:938, 1971.

[28] J.H. Battocletti, R.E Halbach, S.X Salles-Cunha, and A. Sances Jr. The NMR blood flow meter theory and history. *Med. Phys.*, 8:435–443, 1981.

[29] E.L. Hahn. Detection of sea-water motion by nuclear precession. *J. Geophys. Res.*, 65:776–777, 1960.

[30] E.O Stejskal and J.E Tanner. Spin diffusion measurements: spin echoes in the presence of a time-dependent field gradient. *J. Chem. Phys.*, 42:288, 1965.

[31] E.O. Stejskal. Use of spin-echoes in a pulsed magnetic-field gradient to study anisotropic restricted diffusion and flow. *J. Chem. Phys.*, 43:3597, 1965.

[32] P.R. Moran. A flow velocity zeugmatographic interlace for NMR imaging in humans. *MRI*, 1:197–203, 1982.

[33] D.J. Bryant, J.A Payne, D.A Firmin, and D.B Longmore. Measurement of flow with NMR imaging using a gradient pulse and phase difference technique. *J. Comput. Assist. Tomo.*, 8:588–593, 1984.

[34] L. Axel. Blood flow effects in magnetic resonance imaging. *AJR*, 143:1157–1166, 1984.

[35] P. van Dijk. Direct cardiac NMR imaging of heart wall and blood flow velocity. *J. Comput. Assist. Tomo.*, 8:429–436, 1984.

[36] D.N. Firmin, G.L Nayler, P.J Kilner, and D.B Longmore. The application of phase shifts in NMR for flow measurement. *MRM*, 14:230–241, 1990.

[37] T.M. Grist, C.A. Mistretta, C.M. Strother, and P.A. Turski. Time-resolved angiography: past, present, and future. *JMRI*, 36:1273–1286, 2012.

[38] A.J. Wheaton and M. Miyazaki. Non-contrast enhanced MR angiography: physical principles. *JMRI*, 36:286–304, 2012.

[39] D.L. Parker, C. Yuan, and D.D. Blatter. MR angiography by multiple thin slab 3D acquisition. *MRM*, 17:434–451, 1991.

[40] D. Atkinson, M. Brant-Zawadzki, G. Gillan, D. Purdy, and G. Laub. Improved MR angiography: magnetization transfer suppression with variable flip angle excitation and increased resolution. *Radiology*, 190:890–894, 1994.

[41] T. Kimura, M. Ikedo, and S. Takemoto. Hybrid of opposite-contrast MR angiography (HOP-MRA) combining time-of-flight and flow-sensitive black-blood contrasts. *MRM*, 62:450–458, 2009.

[42] R.R. Edelman, J.J. Sheehan, E. Dunkle, N. Schindler, J. Carr, and I. Koktzoglou. Quiescent-interval single-shot unenhanced magnetic resonance angiography of peripheral vascular disease: technical considerations and clinical feasibility. *MRM*, 63:951–958, 2010.

[43] E.J. Offerman, P.A. Hodnett, R.R. Edelman, and I. Koktzoglou. Nonenhanced methods for lower-extremity MRA: a phantom study examining the effects of stenosis and pathologic flow waveforms at 1.5T. *JMRI*, 33:401–408, 2011.

[44] M. Miyazaki and M. Akahane. Non-contrast enhanced MR angiography: Established techniques. *JMRI*, 36:286–304, 2012.

[45] P.R. Moran, D. Saloner, and B.M.W. Tsui. NMR velocity-selective excitation composites for flow and motion imaging and suppression of static tissue signal. *IEEE Trans. Med. Imaging*, 6:141–147, 1987.

[46] C.L. Dumoulin, S.P. Souza, M.F. Walker, and W. Wagle. Three-dimensional phase contrast angiography. *MRM*, 9:139–149, 1989.

[47] M. ODonnell. NMR blood flow imaging using multiecho, phase contrast sequences. *Med. Phys.*, 12:59–64, 1985.

[48] M.A. Bernstein, M. Grgic, T.J. Brosnan, and N.J. Pelc. Reconstructions of phase contrast, phase array multi-coil data. *MRM*, 32:330–334, 1994.

[49] J. Henning, M. Muri, P. Brunner, and H. Friedburg. Quantitative flow measurement with the fast fourier flow technique. *Radiology*, 166:237–240, 1988.

[50] J.L.A. Carvalho and K.S. Nayak. Rapid quantitation of cardiovascular flow using slice-selective Fourier velocity encoding with spiral readouts. *MRM*, 57:639–646, 2007.

[51] J.A. Steeden, A. Jones, B. Pandya, D. Atkinson, A.M. Taylor, and V. Muthurangu. High-resolution slice-selective Fourier velocity encoding in congenital heart disease using spiral SENSE with velocity unwrap. *MRM*, 67:1538–1546, 2012.

[52] R.E. Hendrick, J.B. Kneeland, and D.D. Stark. Maximizing signal-to-noise and contrast-to-noise ratios in FLASH imaging. *MRI*, 5:117–127, 1987.

[53] W.T. Dixon. Simple proton spectroscopic imaging. *Radiology*, 153:189, 1984.

[54] H.Y. Carr. Steady-state free precession in nuclear magnetic resonance. *Phys. Rev.*, 112:1693, 1958.

[55] A.P. Crawley, M.L. Wood, and R.M. Henkelm. Elimination of transverse coherences in FLASH MRI. *MRI*, 8:248–260, 1988.

[56] J. Frahm, W. Haenicke, and K.D Merboldt. Transverse coherence in rapid FLASH NMR imaging. *JMR*, 72:307–314, 1987.

[57] K.T. Block. *Advanced methods for radial data sampling in magnetic resonance imaging*. PhD thesis, Georg-August-University Goettingen, 2008.

[58] S. Zhang. *Real-time magnetic resoance imaging*. PhD thesis, Georg-August-University Goettingen, 2009.

[59] V. Rasche, R.W. De Boer, D. Holz, and R. Prokas. Continuous radial data acquisition for dynamic MRI. *MRM*, 34:754–761, 1995.

[60] M.L. Lauzon and B.K. Rutt. Effects of polar sampling in k-space. *MRM*, 36:940–949, 1996.

[61] T.P. Trouard, Y. Sabharwal, M.I. Altbach, and A.F Gmitro. Analysis and comparison of motion-correction techniques in diffusion-weighted imaging. *JMRI*, 6:925–935, 1996.

[62] J.J. Van Vaals, M.E. Brummer, W.T. Dixon, J.J. Tuithof, J. Engels, R.C. Nelson, B.M. Gerety, J.L. Chezmar, and J.A. den Boer. Keyhole method for accelerating imaging of contrast agent uptake. *JMRI*, 3:671–675, 1993.

[63] D.J. Atkinson and R.R. Edelman. Cineangiography of the heart in a single breath hold with a segmented turboflash sequence. *Radiology*, 178:357–360, 1991.

[64] R.J. Hernandez, A.M. Aisen, T.K.F. Foo, and R.H. Beekman. Thoracic cardiovascular anomalies in children-evaluation with a fast gradient-recalled-echo sequence with cardiac-triggered segmented acquisition. *Radiology*, 188:775–780, 1993.

[65] T.K.F. Foo, M.A. Bernstein, A.M. Aisen, R.J. Hernandez, B.D. Collick, and T. Bernstein. Improved ejection fraction and flow velocity estimates with use of view sharing and uniform repetition time and fast cardiac techniques. *Radiology*, 195:471–478, 1995.

[66] S. Zhang, K.T. Block, and J. Frahm. Magnetic resonance imaging in real time: advances using radial FLASH. *JMRI*, 31:101–109, 2009.

[67] P.B. Roemer, W.A. Edelstein, C.E. Hayes, S.P. Souza, and O.M. Mueller. The NMR phased-array. *MRM*, 16:192–225, 1990.

[68] K. Pruessmann, M. Weigner, M. Scheidegger, and P. Boesiger. SENSE: sensitivity encoding for fast MRI. *MRM*, 42:952–962, 1999.

[69] M. Uecker. *Nonlinear reconstruction methods for parallel magnetic resonance imaging*. PhD thesis, Georg-August-University Goettingen, 2009.

[70] D. Sodickson and W. Manning. Simultaneous acquisition of spatial harmonics (SMASH): fast imaging with radiofrequency coil arrays. *MRM*, 38:591–603, 1997.

[71] M.A. Griswold, P.M. Jakob, R.M. Heidemann, M. Nittka, V. Jellus, J. Wang, K. Berthold, and A. Hasse. Generalized auto-calibrating partially parallel acquisitions (GRAPPA). *MRM*, 47:1202–1210, 2002.

[72] R. Heidemann, M. Griswold, A. Haase, and P. Jakob. VD-auto-SMASH imaging. *MRM*, 45:1066–1074, 2001.

[73] P. Jakob, M. Grisowld, R. Edelman, and D. Sodickson. AUTOSMASH: a self-calibrating technique for SMASH imaging. *MAGMA*, 7:42–54, 1998.

[74] J. Tsao, P. Boesiger, and K.P. Pruessmann. k-t BLAST and k-t SENSE: dynamic MRI with high frame rate exploiting spatiotemporal correlations. *MRM*, 50:1031–1042, 2003.

[75] M. Lustig, M. Donoho, and J.M. Pauly. Sparse MRI: The application of compressed sensing for rapid MR imaging. *MRM*, 58:1182–1195, 2007.

[76] M. Uecker, S. Zhang, D. Voit, A. Karaus, K.D. Merboldt, and J. Frahm. Real-time MRI at a resolution of 20 ms. *NMR Biomed*, 23:986–994, 2010.

[77] S. Zhang, A. Olthoff, and J. Frahm. Real-time magnetic resonance imaging of normal swallowing. *JMRI*, 35:1372–1379, 2012.

[78] A. Niebergall, S. Zhang, E. Kunay, G. Keydana, M. Job, M. Uecker, and J. Frahm. Real-time MRI of speaking at a resolution of 33ms: undersampled radial FLASH with nonlinear inverse reconstruction. *MRM*, 69:477–485, 2013.

[79] M. Uecker, T. Hohage, K.T. Block, and J. Frahm. Image reconstruction by regularized nonlinear inversion- joint estimation of coil sensitivities and image content. *MRM*, 60:674–682, 2008.

[80] A.B. Bakushinsky and M.Yu Kokurin. *Iterative methods for approximate solution of inverse problems.* Springer: Dordrecht, 2004.

[81] M. Uecker, S. Zhang, and J. Frahm. Nonlinear inverse reconstruction for real-time MRI of the human heart using undersampled radial FLASH. *MRM*, 63:1456–1462, 2010.

[82] S. Zhang, M. Uecker, D. Voit, K.D. Merboldt, and J. Frahm. Real-time cardiac MRI at high temporal resolution: radial FLASH with nonlinear inverse reconstruction. *JCMR*, 12:39–45, 2010.

[83] M. Buehrer, K.P. Pruessmann, P. Boesinger, and S. Kozerke. Array compression for MRI with large coil arrays. *MRM*, 58:1131–1139, 2007.

[84] F. Huang, S. Vijayakumar, Y. Li, S. Hertel, and G.R. Duensing. A software channel compression technique for faster reconstruction with many channels. *MRI*, 26:133–141, 2008.

[85] T.S. Sorensen, D. Atkinson, T. Schaeffter, and M.S. Hansen. Real-time reconstruction of sensitivity encoded radial magnetic resonance imaging using a graphics processing unit. *IEEE Trans. Med. Imaging*, 28:1974–1985, 2009.

[86] M. Murphy, M. Alley, J. Demmel, K. Keutzer, S. Vasanawala, and M. Lustig. Fast l1-SPIRiT compressed sensing parallel imaging MRI: scalable parallel implementation and clinically feasible runtime. *IEEE Trans. Med. Imaging*, 31:1250–1262, 2012.

[87] G.T. Kowalik, J.A. Steeden, B. Pandya, D. Atkinson, A.M. Taylor, and V. Muthurangu. Real-time flow with fast GPU reconstruction for continuous assessment of caridac output. *JMRI*, 36:1477–1482, 2012.

[88] S. Schaetz and M. Uecker. A multi-GPU programming library for real-time applications. *Lecture Notes in Computer Science*, 7439:114–128, 2012.

[89] S.M. Wright and L.L. Wald. Theory and application of array coils in MR spectroscopy. *NMR Biomed*, 10:394–410, 1997.

[90] J.S. Hyde, A. Jesmanowicz, W. Froncisz, J.B. Kneeland, and T.M. Grist. Parallel image acquisition for noninteracting local coils. *JMR*, 70:512–517, 1987.

[91] D.O. Walsh, A.F. Gmitro, and M.W. Marcelin. Adaptive reconstruction of phased array MR imagery. *MRM*, 43:682–690, 2000.

[92] M. Bydder, D.J. Larkman, and J.V. Hajnal. Combination of signals from array coils using image-based estimation of coil sensitivity profiles. *MRM*, 47:539–548, 2002.

[93] G.J.M. Parker, G.J. Barker, and P.S. Tofts. Accurate multislice gradient echo T1 measurement in the presence of non-ideal RF pulse shape and RF field nonuniformity. *MRM*, 45:838–845, 2001.

[94] O. Dietrich, M.F. Reiser, and S.O. Schoenberg. Artifacts in 3T MRI: physical background and reduction strategies. *Eur. J. Radiol.*, 65:29–35, 2008.

[95] M.J. Middione and D.B. Ennis. Chemical shift-induced phase errors in phase-contrast MRI. *MRM*, 69:391–401, 2013.

[96] T.E. Conturo and G.D. Smith. Signal-to-noise in phase angle reconstruction: dynamic range extension using phase reference offsets. *MRM*, 15:420–437, 1990.

[97] M.A. Bernstein and Y. Ikezaki. Comparison of phase-difference and complex-difference processing in phase-contrast MR angiography. *JMRI*, 1:725–729, 1991.

[98] D.C. Ghiglia and M.D. Pitt. *Two-dimensional phase unwrapping: theory, algorthms and software.* John Wiley & Sons, Inc, 1998.

[99] F. Stahlberg, C. Thomsen, L. Soendergaard, and O. Henriksen. Pulse sequence design for MR velocity mapping of complex flow: notes on the necessity of low echo times. *MRI*, 12:1255–1262, 1994.

[100] L.R. Frank, A.P. Crawley, and R.B. Buxton. Elimination of oblique flow artifacts in magnetic resonance imaging. *MRM*, 25:299–307, 1992.

[101] C.A. Hamilton, P.R. Moran, P. Santago, and S.A. Rajala. Effects of intravoxel velocity distributions on the accuracy of the phase-mapping method in phase-contrast MR angiography. *JMRI*, 4:752–755, 1994.

[102] F. Stahlberg, L. Sondergaard, C. Thomsen, and O. Henriksen. Quantification of complex flow using MR phase imaging - a study of parameters influencing the phase/velocity relation. *JMRI*, 10:13–23, 1992.

[103] M.A. Bernstein, A. Shimakawa, and N.J. Pelc. Minimizing TE in moment-nulled or flow-encoded two and three-dimensional gradient-echo imaging. *JMRI*, 2:583–588, 1992.

[104] L. Axel and D. Morton. MR flow imaging by velocity-compensated/uncompensated difference images. *J. Comput. Assist. Tomo.*, 11:31–34, 1987.

[105] M. Rolf, M. Hofman, P. Gatehouse, K. Markenroth-Bloch, M. Heymans, T. Ebbers, M. Graves, J. Totman, B. Werner, A. van Rossum, P. Kilner, and R. Heethaar. Sequence optimization to reduce velocity offsets in cardiovascular magnetic resonance volume flow quantification - a multi-vendor study. *JCMR*, 13:18, 2011.

[106] C.B. Ahn and Z.H. Cho. Analysis of eddy currents in nuclear magnetic resonance imaging. *MRM*, 17:149–163, 1991.

[107] P. Jehenson, M. Westphal, and N. Schuff. Analytical method for the compensation of eddy-current effects induced by pulsed magetic-field gradients in NMR systems. *JMR*, 90:264–278, 1990.

[108] Y. Zhou, S.D. Wolff, T.M. Grist, and J.A. Polzin. Investigation of eddy current effect on phase contrast imaging. In *Proc. Intl. Soc. Mag. Reson. Med.*, page 552, 2004.

[109] J. Lotz, C. Meier, A. Leppert, and M. Galanski. Cardiovascular flow measurement with phase contrast MR imaging: basic facts and implementation. *Radiographics*, 22:651–671, 2002.

[110] E.K. Brodsky, A.A. Samsonov, and W.F. Block. Characterizing and correcting gradient errors in non-cartesian imaging: are gradient errors linear time-invariant (LTI). *MRM*, 62:1466–1476, 2009.

[111] J.W. Lankhaar, M.B.M. Hofman, J.T. Marcus, J.J.M Zwanenburg, T.J. Faes, and A. Vonk-Noordegraaf. Correction of phase offset errors in main pulmonary artery flow quantification. *JMRI*, 22:73–79, 2005.

[112] T.A. Miller, A.B. Landes, and A.M. Moran. Improved accuracy in flow mapping of congenital heart disease using stationary phantom technique. *JCMR*, 11:52, 2009.

[113] P.G. Walker, G.B. Cranney, M.B. Scheidegger, G. Waseleski, G.M. Pohost, and A.P. Yoganathan. Semiautomated method for noise-reduction and background phase error correction in MR phase velocity data. *JMRI*, 3:521–530, 1993.

[114] C. Barmet, N. De Zanche, and K.P. Pruessmann. Spatiotemporal magnetic field monitoriing for MR. *MRM*, 60:187–197, 2008.

[115] K. Edler and D. Hoult. Spherical harmonic inductive detection coils for dynamic pre-emphasis. *MRM*, 60:277–287, 2008.

[116] P.D. Gatehouse, M.P. Rolf, M.J. Graves, M.B.M. Hofman, J. Totman, B. Werner, R.A. Quest, Y. Liu, J. von Spiczak, M. Dieringer, D.N. Firmin, A. van Rossum, M. Lombardi, J. Schwitter, J. Schulz-Menger, and P.J. Kilner. Flow measurement by cardiovascular magnetic resonance: a multi-centre multi-vendor study of background phase offset errors that can compromise the accuracy of derived regurgitant or shunt flow measurements. *JCMR*, 12:5–8, 2010.

[117] A.A. Joseph, J Kowallick, K.D Merboldt, D. Voit, S. Schaetz, S. Zhang, J. Sohns, J. Lotz, and J. Frahm. Real-time flow MRI of the aorta at a resolution of 40 ms. *JMRI;*, doi:10.1002/jmri.24328, 2013.

[118] A.A. Joseph, K.D. Merboldt, D. Voit, S. Zhang, M. Uecker, J. Lotz, and J. Frahm. Real-time phase-contrast MRI of cardiovascular blood flow using undersampled radial fast low-angle shot and nonlinear inverse reconstruction. *NMR Biomed.*, 25:917–924, 2012.

[119] B.N. Tillmann. *Atlas der Anatomie des Menschen*. Number ISBN: 978-3-642-02679-9. Springer Berlin Heidelberg, 2005.

[120] A.M. Weissler, W.S. Harris, and C.D Schoenfeld. Systolic time intervals in heart failure in man. *Circulation*, 37:149–159, 1968.

[121] N.J. Pelc, R.J. Herfkens, A. Shimakawa, and D. Enzmann. Phase contrast cine magnetic resonance imaging. *MR Quart*, 7:229–254, 1991.

[122] R.L. Ehman and J.P. Felmlee. Adaptive technique for high-definition MR imaging of moving structures. *Radiology*, 173:255–263, 1989.

[123] H.W. Korin, F. Farzaneh, R.C. Wright, and S.J Riederer. Compensation for effects of linear motion in MR imaging. *MRM*, 12:99–113, 1989.

[124] M. Markl and J. Henning. Phase contrast MRI with improved temporal resolution by view sharing: k-space related velocity mapping properties. *MRM*, 19:669–676, 2001.

[125] T.S. Sachs, C.H. Meyer, B.S. Hu, J Kohli, D.G Nishimura, and A. Macovski. Real-time motion detection in spiral MRI using navigators. *MRM*, 32:639–645, 1994.

[126] M. Markl, A. Harloff, T.A. Bley, M. Zaitsev, B. Jung, E. Weigang, M. Langer, J. Hennig, and A. Frydrychowicz. Time-resolved 3D MR velocity mapping at 3T: Improved navigator-gated assessment of vascular anatomy and blood flow. *JMRI*, 25:824–831, 2007.

[127] H. Sakuma, N. Kawada, H. Kubo, Y. Nishide, K. Takano, N. Kato, and K. Takeda. Effect of breath holding on blood flow measurement using fast velocity encoded cine MRI. *MRM*, 45:346–348, 2001.

[128] G.L. Nayler, D.N. Firmin, and D.B. Longmore. Blood flow imaging by cine magnetic resonance. *J. Comput. Assist. Tomo.*, 10:751–722, 1986.

[129] M.J. Bland and D.G. Altman. Statistical methods for assessing agreement between two methods of clinical measurement. *Lancet*, 327:307–310, 1986.

[130] D.N. Firmin, R.H. Klipstein, G.L. Hounsfield, M.P. Paley, and D.B. Longmore. Echo-planar high-resolution flow velocity mapping. *MRM*, 12:316–327, 1989.

[131] J.F. Debatin, D.A. Leung, S. Wildermuth, R. Botnar, J. Felblinger, and G.C. McKinnon. Flow quantitation with echo-planar phase contrast mapping: in vitro and in vivo evaluation. *JMRI*, 5:656–662, 1995.

[132] A.C. Eichenberger, J. Schwitter, G.C. McKinnon, J.F. Debatim, and G.K. Von Schulthess. Phase-contrast echo-planar MR imaging: real-time quantification of flow and velocity patterns in the thoracic vessels by valsalva's maneuver. *JMRI*, 5:648–655, 1995.

[133] R.B. Thompson and E.R. McVeigh. High temporal resolution phase contrast MRI with multiecho acquisitions. *MRM*, 47:499–512, 2002.

[134] K.M. Johnson, D.P. Lum, P.A. Turski, W.F. Block, C.A. Mistretta, and O. Wieben. Improved 3D phase contrast MRI with off-resonance corrected dual echo VIPR. *MRM*, 60:1329–1336, 2008.

[135] V.M. Pai. Phase contrast using multiecho steady-state free precession. *MRM*, 58:419–424, 2007.

[136] M.P. Rolf, M.B.M. Hofman, J.P.A. Kuijer, V.M. Pai, A. Greiser, A.C. van Rossum, and R.M. Heethaar. Extrinsic multiecho phase-contrast SSFP: evaluation on cardiac output measurements. *MRI*, 27:385–392, 2009.

[137] M. Markl, P.C. Francis, M.T. Alley, K.L. Wedding, M.T. Draney, C.J. Elkins, D.W. Parker, R. Wicker, C.A. Taylor, R.J. Herfkens, and N.J. Pelc. Time-resolved three-dimensional phase-contrast MRI. *JMRI*, 17:499–506, 2003.

[138] L. Wigstroem, L. Sjoeqvist, and B. Wranne. Temporally resolved 3D phase-contrast imaging. *MRM*, 36:800–803, 1996.

[139] M. Markl, F. Wegent, T. Zech, S. Bauer, C. Strecker, M. Schumacher, C. Weiller, J. Hennig, and A. Harloff. In vivo wall shear stress distribution in the carotid artery: effect of bifurcation geometry, internal carotid artery stenosis and recanalization therapy. *Circ. Cardiovasc. Imag.*, 3:647–655, 2010.

[140] Z. Stankovic, A. Frydrychowicz, Z. Csatari, E. Panther, P. Deibert, W. Euringer, W. Kreisel, M. Russe, S. Bauer, M. Langer, and M. Markl. MR-based visulaization and quantification of three-dimensional flow characteristics in the portal venous system. *JMRI*, 32:466–475, 2010.

[141] J.P. Kvitting, T. Ebbers, J. Engvall, G.R. Sutherland, B. Wranne, and L. Wigstroem. Three-directional myocardial motion assessed using 3D phase contrast MRI. *JCMR*, 6:627–636, 2004.

[142] M.D. Hope, A.K. Meadows, T.A. Hope, K.G. Ordovas, D. Saloner, G.P. Reddy, M.T. Alley, and C.B. Higgins. Clinical evaluation of aortic coarctation with 4D flow MR imaging. *JMRI*, 31:711–718, 2010.

[143] S. Kozerke, J.M. Hasenkam, E.M. Pedersen, and P. Boesiger. Visualization of flow patterns distal to aortic valve prostheses in humans using a fast approach for cine 3D velocity mapping. *JMRI*, 13:690–698, 2001.

[144] M.H. Buonocore. Visualizing blood flow patterns using streamlines, arrows, and particle paths. *MRM*, 40:210–226, 1998.

[145] L. Wigstroem, T. Ebbers, A. Fyrenius, M. Karlsson, J. Engvall, B. Wranne, and A.F. Bolger. Particle trace visualization of intercardiac flow using time-resolved 3D phase contrast MRI. *MRM*, 41:793–799, 1999.

[146] D.C. Peters, F.R. Korosec, T.M. Grist, W.F Block, J.E. Holden, K.K. Vigen, and C.A. Mistretta. Undersampled projection reconstruction applied to MR angiography. *MRM*, 43:91–101, 2000.

[147] A. Shankaranarayanan, O.P. Simonetti, G. Laub, J.S Lewin, and J.L Duerk. Segmented k-space and real-time cardiac cine MR imaging with radial trajectories. *Radiology*, 221:827–836, 2001.

[148] A.F. Parisi, J.J. Harrington, J. Askenazi, R.C. Pratt, and K.M. Mclntyre. Echocardiographic evaluation of the valsalva maneuver in healthy subjects and patients with and without heart failure. *Circulation*, 54:921–927, 1976.

[149] J.C.Jr. Greenfield, R.L. Cox, R.R. Hernandez, C. Thomas, and F.W. Schoonmaker. Pressure-flow studies in man during the valsalva maneuver with observations on the mechanical properties of the ascending aorta. *Circulation*, 35:653–661, 1967.

[150] P.D. Gatehouse, D.N. Firmin, S. Collins, and D.B. Longmore. Real-time blood flow imaging by spiral scan phase velocity mapping. *MRM*, 31:504–512, 1994.

[151] J.L. Carvalho, H.S. Carvalho, and K.S. Nayak. Assessment of stroke volume variability using real-time spiral phase contrast. In *Proc. Intl. Soc. Mag. Reson. Med.*, volume 16, page 383, 2008.

[152] R. Willeput, C. Rondeux, and A.D. Troyer. Breathing effects venous return from legs in humans. *J. Appl. Physiol.*, 57:971–976, 1984.

[153] V.E Hjortdal, K. Emmertsen, and E. Stenbog. Effects of excercise and respiration on blood flow in total cavopulmonary connection: a real-time magnetic resonance flow study. *Circulation*, 108:1227–1231, 2003.

[154] J.D. Miller, D.F. Pegelow, A.J. Jacques, and J.A. Dempsey. Sketal muscle pump versus respiratory muscle pump: Modulation of venous return from the locomotor limb in humans. *J. Physiol.*, 563:925–943, 2005.

[155] J.P. Carpenter, G.A. Holland, R.A. Baum, J.T. Carpenter, and C. Cope. Magnetic resonance venography for the detection of deep venous thrombosis: Comparison with contrast venography and duplex doppler ultrasonography. *J. Vasc. Surg.*, 18:734–741, 1993.

[156] D.G.W. Fraser, A.R. Moody, I.R. Davidson, A.L. Martel, and P.S. Morgan. Deep venous thrombosis: diagnosis by using venous enhanced subtracted peak arterial MR venography versus conventional venography. *Radiology*, 226:812–820, 2003.

[157] C.P. Cantwell, A. Cradock, J. Bruzzi, P. Fitzpatrick, S. Eustace, and J.G. Murray. MR venography with true fast imaging with steady-state precession for suspected lower-limb deep vein thrombosis. *J. Vasc. Interv. Radiol.*, 17:1763–1769, 2006.

[158] M.S. Wang, D.R. Haynor, G.J. Wilson, and J.H. Maki. Intravascular hematocrit layering in equilibrium phase contrast-enhanced MR angiography of peripheral vasculature. *JMRI*, 24:1393–1400, 2006.

[159] I.T. Pierce, P.D. Gatehouse, X. Yun Xu, and D. Firmin. MR phase-contrast velocity mapping methods for measuring venous blood velocity in the deep veins of the calf. *JMRI*, 34:634–644, 2011.

[160] M.J. Callam. Epidemiology of varicose veins. *Br. J. Surg.*, 81:167–173, 1994.

[161] D.P. Burkitt. Varicose veins, deep vein thrombosis, and haemorrhoids: epidemiology and suggested aetiology. *Br. Med. J.*, 2:556–561, 1972.

[162] F.V. Coakley, S.L. Varghese, and H. Hricak. CT and MRI of pelvic varices in women. *J. Comput. Assist. Tomo.*, 23:429–434, 1999.

[163] D.D. Stark, P.F. Hahn, C. Trey, M.E Clouse, and J.T Ferrucci Jr. MRI of the budd-chiari syndrome. *AJR*, 146:1141–1148, 1986.

[164] S.S. Blemker, D.S. Asakawa, G.E. Gold, and S.L. Delp. Image-based musculoskeletal modeling: Applications, advances, and future opportunities. *JMRI*, 25:441–451, 2007.

[165] F.C. Anderson and M.G. Pandy. Individual muscle contributions to support normal walking. *Gait Posture*, 17:159–169, 2003.

[166] S.J. Piazza and S.L. Delp. The influence of muscles on knee flexion during the swing phase of gait. *J. Biomech.*, 29:723–733, 1996.

[167] S.G. McLean, A. Su, and A.J. van den Bogert. Development and validation of a 3D model to predict knee joint loading during dynamic movement. *J. Biomech. Eng.*, 125:864–874, 2003.

[168] P.D. Neilson, N.J. ODwyer, and J. Nash. Control of isometric muscle activity in cerebral palsy. *Developmental Medicine and Child Neurology*, 32:778–788, 1990.

[169] J.R. Gage. *Gait analysis in cerebral palsy.* Mac Keith Press, London, 1991.

[170] G. Tardieu and C. Tardieu. Cerebral palsy. mechanical evaluation and conservative correction of limb joint contractures. *Clinical Orthopaedics and Related Research*, 219:63–69, 1987.

[171] M.S. Cornell. The hip in cerebral palsy. *Developmental Medicine and Child Neurology*, 37:3–18, 1995.

[172] J.E. Drace and N.J. Pelc. Measurement of skeletal muscle motion in vivo with phase-cotnrast MR imaging. *JMRI*, 4:157–163, 1994.

[173] F.T. Sheehan, F.E. Zajac, and J.E. Drace. Using cine phase contrast magnetic resonance imaging to non-invasively study in vivo knee dynamics. *J. Biomech.*, 31:21–26, 1998.

[174] G.P. Pappas, D.S. Asakawa, S.L. Delp, F.E. Zajac, and J.E. Drace. Nonuniform shortening in the biceps brachii during elbow flexion. *J. Appl. Physiol.*, 92:2381–2389, 2002.

[175] C.E. Draper, T.F. Beiser, J.M. Santos, F. Jennings, M. Fredericson, G.E. Gold, G.S. Beaupre, and S.L. Delp. Using real-time MRI to quantify altered joint kinematics in subjects with patellofemoral pain and to evaluate the effects of a patelllar brace or sleeve on join motion. *J. Orthopaed. Res.*, 27:571–577, 2009.

[176] G.E. Gold, G.P. Pappas, S.S. Blemker, S.T. Whalen, G. Campbell, T.A. McAdams, and C.F. Beaulieu. Abduction and external rotation in shoulder impingement: an open MR study on healthy volunteers- initial experience. *Radiology*, 244:815–822, 2007.

[177] H.D. Lee, T. Finni, J.A. Hodgson, A.M. Lai, V.R. Edgerton, and S. Sinha. Soleus aponeurosis strain distribution following chronic unloading in humans: an in vivo MR phase-contrast study. *J. Appl. Physiol.*, 100:2004–2011, 2006.

[178] D. Shin, T. Finni, S. Ahn, J.A. Hodgson, H.D. Lee, V.R. Edgerton, and S. Sinha. In vivo estimation and repeatability of force-length relationship and stiffness of the human achilles tendon using phase contrast MRI. *JMRI*, 28:1039–1045, 2008.

[179] D.S. Asakawa, K.S. Nayak, S.S. Blemker, S.L Delp, J.M Pauly, D.G. Nishimura, and G.E Gold. Real-time imaging of skeletal muscle velocity. *JMRI*, 18:734–739, 2003.

[180] J. Tack. Gastro motor disorders. *Best Pract. Res. Clin. Gastroenterol.*, 21:633–644, 2007.

[181] G. Stacher. Oesophageal motility, oesophageal transit, and gastro-oesophageal reflux-a methodological overview. *Hepatogastroenterology*, 32:299–304, 1985.

[182] M.D. Gelfand and V.A. Botoman. Esophageal motility disorders: a clinical overview. *Am. J. Gastroenterol.*, 82:181–187, 1987.

[183] M.Y. Chen, D.J. Ott, J.W. Sinclair, W.C. Wu, and D.W. Gelfand. Gastroesophageal reflux disease: correlation of esophageal pH testing and radiographic findings. *Radiology*, 185:483–486, 1992.

[184] M.T. Crawley, P. Savage, and F. Oakley. Patient and operator dose during fluroscopic examination of swallow mechanism. *Br. J. Radiol*, 77:654–656, 2004.

[185] V. Panebianco, E. Tomei, M. Anzidei, F.I. Habib, C. Catalano, D. Lisi, A. Laghi, and R. Passariello. Functional MRI in the evaluation of oesophageal motility: feasibility, MRI patterns of normality and prelimary experience in subjects with motility disorders. *Radiol. Med.*, 111:881–889, 2006.

[186] T. Manabe, H. Kawamitsu, T. Higashino, Shirasaka D, Aoyama N, and Sugimura K. Observation of gasrto-esophageal reflux by MRI: a feasibility study. *Abdom. Imaging*, 34:419–423, 2009.

[187] J. Curcic, M. Fox, E. Kaufman, Z. Forras-Kaufman, G.S. Hebbard, S. Roy, A. Pal, W. Schwizer, M. Fried, R. Treier, and P. Boesiger. Gastroesophageal junction: structure and function as assessed by using MR imaging. *Radiology*, 257:115–124, 2010.

[188] C. Kulinna-Cosentini, M.D. Schima, and E.P. Cosentini. Dynamic MR imaging of the gastroesophageal junction in healthy volunteers during bolus passage. *JMRI*, 25:749–754, 2007.

[189] C. Kulinna-Cosentini, M.D. Schima, J. Lenglinger, M. Riegler, C. Koelblinger, A. Ba-Ssalamah, G. Bischof, M. Weber, P. Kleinhansl, and E.P. Cosentini. Is there a role for dynamic swallowing MRI in the assessment of gastroesophageal reflux disease and oesophageal motility disorders? *Eur. Radiol.*, 22:364–370, 2012.

[190] K.S. Nayak, J.M. Pauly, A.B. Kerr, B.S. Hu, and D.G. Nishimura. Real-time color flow MRI. *MRM*, 43:251–258, 2000.

[191] C. Klein, S. Schalla, B. Schnackenburg, A. Bornstedt, E. Fleck, and E. Nagel. Magnetic resonance flow measurements in real time: comparison with a standard gradient-echo technique. *JMRI*, 14:306–310, 2001.

[192] H. Koerperich, J. Gieseke, P Barth, R. Hoogeveen, H. Esdorn, A. Peterschroeder, H. Meyer, and P. Beerbaum. Flow volume and shunt quantification in pediatric congenital heart disease by real-time magnetic resonance velocity mapping: A validation study. *Circulation*, 107:1987–1993, 2004.

[193] R. Nezafat, P. Kellman, J.A. Derbyshire, and E. Mcveigh. Real-time blood flow imaging using autocalibrated spiral sensitivity encoding. *MRM*, 54:1557–1561, 2005.

[194] J.A. Steeden, D. Atkinson, A.M. Taylor, and V. Muthurangu. Assessing vascular response to exercise using a combination of real-time spiral phase contrast MR and noninvasive blood pressure measurements. *JMRI*, 31:997–1003, 2010.

[195] H. Li, M. Haltmeier, S. Zhang, J. Frahm, and A. Munk. Aggregated motion estimation for image reconstruction in real-time MRI. *arXiv preprint, arXiv:1304.5054*, 2013.

[196] H.Y. Lin, J.A. Bender, Y. Ding, Y.C. Chung, A.M. Hinton, M.L. Pennel, K.K. Whitehead, S.V. Raman, and O.P. Simonetti. Shared velocity encoding: a method to improve the temporal resolution of phase-contrast velocity measurements. *MRM*, 68:703–710, 2012.

List of Publications

Journal Publications

- Arun A. Joseph, Klaus-Dietmar Merboldt, Dirk Voit, Shuo Zhang, Martin Uecker, Joachim Lotz and Jens Frahm, Real-time phase-contrast MRI of cardiovascular blood flow using undersampled radial fast low-angle shot and nonlinear inverse reconstruction. *NMR in Biomedicine*, 25:917-924 (2012).

- Arun A. Joseph, Johannes T. Kowallick, Klaus-Dietmar Merboldt, Dirk Voit, Sebastian Schaetz, Shuo Zhang, Jan Sohns, Joachim Lotz and Jens Frahm, Real-time flow MRI of the aorta at a resolution of 40 ms. *Journal of Magnetic Resonance Imaging*, 2013; doi:10.1002/jmri.24328.

Conference Contributions

- Arun A. Joseph, Dirk Voit, Klaus-Dietmar Merboldt, Martin Uecker, Shuo Zhang and Jens Frahm. Real-time cardiovascular PC imaging using undersampled radial FLASH and nonlinear inverse reconstruction. Annual Meeting ISMRM, Melbourne 2012, In *Proc. Intl. Soc. Mag. Reson. Med.* 20:673 (2012).

- Jan M. Sohns, Arun A. Joseph, Klaus-Dietmar Merboldt, Dirk Voit, Shuo Zhang, Martin Uecker, Joachim Lotz, and Jens Frahm. Quantitative Phasenkontrast-MRT der Aorta in Echtzeit - radiales FLASH mit Unterabtastung und nichtlinearer inverser Rekonstruktion, 4. Deutsche Kardiodiagnostik-Tage, Leipzig 2012, *Fortschr. Röntgenstr.* 184 - TNE14 (2012).

- Dirk Voit, Klaus-Dietmar Merboldt, Martin Uecker, Arun A. Joseph, Joachim Lotz, and Jens Frahm. Real-time MRI of Cardiac Function and Flow at a Resolution of 35 ms, 9th IMRI, Boston 2012, In *Proc. 9th Intvnl. MRI Symp.*, Oral V8, p. 27 (2012).

- Arun A. Joseph, Jan M. Sohns, Johannes T. Kowallick, Klaus-Dietmar Merboldt, Joachim Lotz and Jens Frahm. Real-time cardiovascular phase-contrast flow MRI during Valsalva maneuver. Annual Meeting ISMRM, Salt Lake City 2013, In *Proc. Intl. Soc. Mag. Reson. Med.* 21:4441 (2013).

- Arun A. Joseph, Dirk Voit, Sebastian Schätz, Klaus-Dietmar Merboldt and Jens Frahm. Towards real-time 3D phase-contrast flow MRI. Annual Meeting ISMRM, Salt Lake City 2013, In *Proc. Intl. Soc. Mag. Reson. Med.* 21:4567 (2013).

- Shuo Zhang, Alexander Beham, Arun A. Joseph, Henrik Forster, Aaron Niebergall, Martin Uecker and Jens Frahm. Real-time MRI of Esophageal Function at a Resolution of 50 ms: Initial Results in Healthy Subjects. Annual Meeting ISMRM, Salt Lake City 2013, In *Proc. Intl. Soc. Mag. Reson. Med.* 21:0676 (2013).

- Jan M. Sohns, Christina Unterberg-Buchwald, Johannes T. Kowallick, Michael Steinmetz, Christina Schulte, Wieland Staab, Arun A. Joseph, Klaus-Dietmar Merboldt, Dirk Voit, Shuo Zhang, Martin Uecker, Jens Frahm, and Joachim Lotz. Real-time cardiac phase contrast MRI blood flow including Valsalva and Mueller maneuver. Initial experiences. In 16th Annual SCMR Scientific Sessions, *Journal of Cardiovascular Magnetic Resonance*; 15(Suppl 1):E17 (2013).

- Joachim Lotz, Jan M. Sohns, Michael Steinmetz, Johannes T. Kowallick, Christina Schulte, Wieland Staab, Arun A. Joseph, Klaus-Dietmar Merboldt, Dirk Voit, Shuo Zhang, Martin Uecker, Christina Unterberg-Buchwald, Gerd Hasenfus, and Jens Frahm. High resolution real-time CMR of function and flow: initial clinical results. *Journal of Cardiovascular Magnetic Resonance*; 15(Suppl 1): E99 (2013).

- Jan M. Sohns, Johannes T. Kowallick, Christina Unterberg-Buchwald, Wieland Staab, Arun A. Joseph, Klaus-Dietmar Merboldt, Martin Uecker, Dirk Voit, Shuo Zhang, Jens Frahm, and Joachim Lotz. Echtzeit-Cardio-MRT-Phasenkontrast-Flussmessungen mit dem Valsalva- und Müllermaneuver als Stresstest. 94. Deutscher Röntgenkongress Fronleichnam 2013, *Fortschr. Röntgenstr.*: 185 - VO105_I_5 (2013).

- Johannes T. Kowallick, Jan M. Sohns, Christina Unterberg-Buchwald, Christina Schulte, Wieland Staab, Klaus-Dietmar Merboldt, Dirk Voit, Shuo Zhang, Arun A. Joseph, Jens Frahm, Joachim Lotz. Hochauflösende Echtzeit-Cardio-MRT Flussmessung im Vergleich zur Cine Phasenkontrast-Flussmessung. 94. Deutscher Röntgenkongress Fronleichnam 2013, *Fortschr. Röntgenstr.*: 185 - VO105_ I_ 4 (2013).

- Johannes T. Kowallick, Jan M. Sohns, Christina Unterberg-Buchwald, Arun A. Joseph, Klaus-Dietmar Merboldt, Shuo Zhang, Dirk Voit, Christina Schulte, Wieland Staab, Jens Frahm, Joachim Lotz. Echtzeit-Cardio-MRT-Phasenkontrast-Flussmessung mit dem Valsalva-Manöver als Stresstest. Initiale klinische Ergebnisse. 79. Jahrestagung der Deutsche Gesellschaft für Kardiologie- Herz- und Kreislaufforschung, Mannheim 2013, *Clin. Res. Cardiol.* 102 (Suppl 1): P758 (2013).

- Markus Huellebrand, Anja Hennemuth, Lennart Tautz, Arun A. Joseph, Jens Frahm, Stephan Krass. Quantitative Analysis of Bloodflow Variation based on Realtime PC MRI. Accepted for Quantitative Imaging Reading Room, RSNA annual meeting 2013, Chicago.

Acknowledgments

I am very grateful to Prof. Dr. Peter Jakob from the Department of Experimental Physics 5 at the Julius-Maximilians-Universität Würzburg for being the examiner of my thesis and the kind support provided during the work of this thesis.

I would like to thank Prof. Dr. Jens Frahm, head of the Biomedizinische NMR Forschungs GmbH am Max-Planck-Institut für biophysikalische Chemie, for being my advisor and guide during the course of this thesis. It has been a great honor and pleasure to be his student. His vision, zeal, enthusiasm and unending quest for knowledge has been highly inspirational and stimulating to pursue research as a PhD student. In many instances, his simple approach and clarity of thoughts had provided the necessary determination to focus on the challenges put forth by the research. In addition to the scientific skills, I have also learnt leadership and management skills from him.

I am also thankful to Dr. Klaus-Dietmar Merboldt and Dr. Dirk Voit for being my supervisors during the work of thesis. They were always helpful and approachable for critical thinking, innumerable discussions and exploring new ideas. These discussions have helped me to acquire greater knowledge in MRI and flow imaging. I will cherish their constant guidance, encouragement and friendship provided to me.

I am grateful to all my colleagues of Biomedizinische NMR Forschungs GmbH for all the good time and friendship provided to me. The pleasant and excellent working atmosphere created by them was really helpful to enjoy research and work as a team. I would like to express my gratitude to Ms.Sylke Wallbrecht and Dr.Meike Schweisfurth for providing me the necessary assistance in VISA process and other administrative procedures during my initial days in Göttingen. Further I would like to thank Dr.Shuo Zhang for the friendship and enjoyable philosophical discussions during my PhD.

I express my sincere gratitude to my parents, my brother and family for the love, care and support through the journey of this thesis. Throughout my life they have motivated and encouraged me to courageously push the limits and define new paths. This thesis is dedicated to them as an appreciation for their unblemished love and trust in me. Last but not the least, I thank God for this exciting and memorable phase of my life.

Erklärung

Göttingen, den 20. 03. 2014

(Arun Antony Joseph)